Assessment of optical systems by means of point-spread functions

Joseph J.M. Braat, Sven van Haver

Optics Research Group, Technical University Delft, Lorentzweg 1, 2628 CJ Delft, The Netherlands

Augustus J.E.M. Janssen, Peter Dirksen

Philips Research Europe, HTC 36 / 4, 5600 JA Eindhoven, The Netherlands

To be published in:
Progress in Optics, Vol. **51**, Ed. E. Wolf, Elsevier, Amsterdam / The Netherlands, 2008
See also http://www.nijboerzernike.nl

Contents

1 Introduction

The subject of this chapter is the computation of the point-spread function of optical imaging systems and the characterization of these systems by means of the measured three-dimensional structure of the point-spread function. The point-spread function, accessible in the optical domain only in terms of the energy density or the energy flow, is a nonlinear function of the basic electromagnetic field components in the focal region. That is why the reconstruction of the amplitude and phase of the optical far-field distribution that produced a particular intensity point-spread function is a nonlinear procedure that does not necessarily have a unique solution.

For a long time, a detailed measurement of the point-spread function was not possible because of the lack of adequate intensity recording media. The eye of a human subject, although close to perfection over the typical diameter of its iris, is not capable of appreciating the small imperfections that may be present in high-quality instruments for optical observation. In the seventeenth and eighteenth century, telescopes and microscopes were still manufactured in a craftmanship way, without the feedback from reliable and objective optical measurement. Generally speaking, one could say that he modern epoch of high-quality instrument making has started with the pioneering work by Joseph von Fraunhofer who combined his gifts in optical design with a professional approach to optical measurement technology and manufacturing. In a few decades, as of 1850, the trial-and-error methods from the past were ruled out and scientific instrument making was gradually introduced. Nowadays, the perfection of optical instruments has reached a level that was thought to be impossible in the still recent past, see the statement in [Conrady (1929)]: "it is no use to acquire a microscope objective with a numerical aperture beyond 0.80 because a still larger cone of light will only contribute to light gathering and not to improved imaging". Especially since the 1970's, the quality of optical imaging systems (telescopes, microscope objectives, high-quality projection lenses for optical lithography, space observation cameras) has been pushed to the extreme limits. At this level of perfection, a detailed analysis of the optical point-spread function is necessary to understand the image formation by these instruments, especially when they operate at high numerical aperture. In terms of the imaging defects, we are allowed to suppose that the wavefront aberration of such instruments is not substantially larger than the wavelength λ of the light. In most cases, the aberration even has to be reduced to a minute fraction of the wavelength of the light to satisfy the extreme specifications of

these imaging systems. In the following paragraphs we briefly present the past work on point-spread function analysis and its application to the assessment of imaging systems. We conclude this introduction with a brief outline of the further contents of the chapter.

1.1 The optical point-spread function

A very comprehensive overview of the early history of point-spread function analysis can be found in a review paper by [Wolf (1951)]; in this subsection we mention the most important steps in the remote past that have led to our present knowledge and then sketch in some more detail the recent developments since the 1950's.

The early point-spread function analysis was based on ray optics and it focused on the influence of spherical aberration (see early work by Christiaan Huygens, reported in [Korteweg, Huygens complete works (1941)]). Because of the increasing quality of optical components at the beginning of the 19^{th} century and the refinement of, for instance, astronomical observations, a more sophisticated analysis of the optical point-spread function in focus was required. This led to the expression given in [Airy (1835)] that is based on the wave theory of light and takes into account the diffraction of light on its passage through an aperture with limited extent. Point-spread function interaction when imaging incoherent sources was studied by Rayleigh, see [Rayleigh (1879)], leading to his still frequently used criterion for minimum star separation in astronomy. An important step forward in the analysis of the point-spread function can be found in [Lommel (1885)] who derived analytic expressions for the out-of-focus region, thus for the first time systematically adding the axial dimension in the analysis of diffraction images. An interesting criterion in quality assessment of optical systems was introduced by Strehl, see his publication [Strehl (1896)]. He defined the ratio of the maximum on-axis intensity of the point-spread function of an actual imaging system and its theoretical value in the absence of aberrations, given by Airy's expression. This quantity was given the name 'Definitionshelligkeit', later called Strehl definition or Strehl ratio in the English literature. Since then, various authors have focused on numerical evaluations ([Conrady (1919)]) and analytic expressions for the diffraction image or its Strehl ratio in the presence of certain typical aberrations like spherical aberration ([Steward (1925)]) and coma or astigmatism, see [Picht (1925)]. During this period, a continuous subject of research was the optimum distribution or 'balancing' of aberrations of various orders and types to optimize

the quality of the point-spread function, see [Richter (1925)] for a discussion of this topic. This subject was and still is of great practical importance for the optical system designers who need useful rules-of-thumb in their laborious optimization activity.

A break-through in point-spread function analysis and the study of aberrations was brought about by the introduction of the circle polynomials in optical diffraction problems, see [Zernike (1934)]). They were applied to the study of weakly or moderately aberrated point-spread functions in references [Nijboer (1942)] and [Zernike, Nijboer (1949)]). The orthogonality of the Zernike circle polynomials provided the optical system design community with a general solution to the 'balancing' problem of residual aberrations in well-corrected imaging systems. The circle polynomials also proved their usefulness when studying the allowable amount of aberration of an optical system to attain a certain minimum on-axis intensity (Strehl intensity). According to a result derived in [Maréchal (1947)], the deviation from unit Strehl ratio for small aberrations is given by $\mathrm{Var}(\Phi)$, the variance of the phase departure Φ of the focusing wave over the exit pupil of the optical system. Applying the circle polynomials to expand the phase function Φ leads to an expression for $\mathrm{Var}(\Phi)$ that is a simple weighted sum of squares of the Zernike expansion coefficients, see [Born, Wolf (2002)]).

An important new development in the study of the point-spread function of an imaging system is related to the extension of the light propagation from the common scalar to the more intricate vector model. The complete set of electric and magnetic field vectors has to be calculated in the focal region of the optical system and, from these, the relevant electromagnetic quantities like energy density and the flow components related to energy, impulse and angular momentum can be obtained. A first series of publications by [Ignatowsky (1919)] on the vector field in focus passed relatively unnoticed by the community. Some qualitative considerations on the vector aspects of the field in focus were put forward by Hopkins [Hopkins (1943)]. It finally was a set of two papers, [Wolf (1959)] and [Richards, Wolf (1959)], that triggered the interest for the rigorous study of high-quality imaging systems with a numerical aperture higher than, say, 0.60. Nowadays, the vector diffraction theory proposed in these papers is widely used, together with alternative representations that will be equally discussed in this chapter. Fields of application are high-resolution three-dimensional microscopy, high-density optical data storage and high-resolution optical lithography.

It was mentioned above that the assessment of the quality of a highly specified optical system has to be done in the wavefront domain down to a fraction of the wavelength of the light. Interferometric methods are mostly used for this purpose. Although the achievable precision is very high, these methods need refined and delicate optical set-ups and, in practice, special laser sources to achieve sufficient signal-to-noise ratio. When a measurement at a specific wavelength is needed for which an adequate source is not available, interpolation from measurements at other wavelengths would be required and the measurement accuracy can become a problem. For that reason, a direct measurement of the point-spread function (or intensity impulse response) can be of great practical interest if it is possible to derive from such an intensity distribution the relevant quality data of the optical system, in particular the wavefront aberration. The strongly nonlinear relationship between the phase departure in the exit pupil of the optical system and the detected intensity in the focal plane leads to an ill-posed inversion problem. The first publications on this type of inversion problems go back to [Gerchberg, Saxton (1971)], [Gerchberg, Saxton (1972)]and [Frieden (1972)]. To improve the stability of the inversion process, extra information from e.g. the pupil intensity distribution (optical far field intensity) or from several image planes in the focal region is incorporated like the 'phase diversity' method proposed by [Gonsalves (1982)], or the multiple images phase retrieval method in electron microscopy by [VanDijck, Coene (1987)]). An early 'phase retrieval' methods is found in [Fienup (1982)]; later developments can be found in [Barakat, Sandler (1992)], [Frieden, Oh (1992)], [Fienup, Marron, Schultz, Seldin (1993)], [Iglesias (1998)] and [Fienup (1999)]. The focus in this chapter will be on the assessment of optical systems using the optical point-spread function, especially in the case of systems with very high values of the numerical aperture in image space. The reconstruction of complete objects, a much broader subject, is outside the scope of this chapter. We will pay special attention to methods for representing the pupil function of the optical system and the analytic or numerical steps that are needed to obtain the point-spread function in the focal region. The stability of the various pupil function representations in the inversion process is studied and the range of wavefront aberration that can be retrieved is tested.

The organization of the chapter is as follows. We first present in Section 2 the calculation method in the forward direction to arrive from the complex amplitude in the exit pupil of an optical system to the amplitude in the focal

region in image space. Various levels of approximation in solving the pertinent diffraction integral are addressed, leading to the Rayleigh and Debye integral expressions and the so-called paraxial approximation; both the scalar and the vector diffraction formalism are discussed. One of the important subjects in this section is the efficient and stable representation of the exit pupil distribution or far field by means of Zernike polynomials. Section 3 uses the results from the previous section to develop analytic expressions for the energy density and the Poynting vector components in the focal region, this in the presence of a general exit pupil function characterized by its complex Zernike expansion coefficients. In Section 4 we address the general inverse problem in optical imaging and the various methods that have been devised so far for solving this problem. In Section 5, the emphasis is on the application of the extended Nijboer-Zernike diffraction theory to the optical inverse problem. By using the information from through-focus point-source images we describe a method to assess the quality of the optical system regarding its optical aberrations, transmission defects and birefringence. In this section, both the scalar and vector diffraction theory will be applied to the solution of the optical inverse problem. The final short section presents the conclusions and an outlook to further research in this field. Several appendices give detailed derivations of results that were needed in the main body of the text.

2 Theory of point-spread function formation

In this section we describe the optical model that is used for calculating the point-spread function of optical systems that suffer from relatively small wavefront aberrations. Analytic or semi-analytic expressions for both the in-focus and the out-of-focus point-spread function are given, based on the work by [Lommel (1885)] and [Nijboer (1942)]. Recent extensions apply to the description of through-focus point-spread functions in the presence of aberrations while these are crucial when solving the inverse problem. As the basis for our point-spread function calculation we will use the Debye diffraction integral. Its derivation from more general diffraction integrals and its limits of applicability are discussed in some detail. The optical model is first based on the common scalar approximation and is then extended to include vector diffraction effects.

2.1 Field representations and the diffraction integral

In representing a field distribution on a surface and its propagated and/or diffracted version elsewhere, it is possible to use either the basic principle of Huygens' spherical wavelets or the more recently developed plane wave expansion and the concept of Fourier transformation associated with it. In the latter case, the field distribution is described in terms of the complex spectrum of spatial frequencies, each spatial frequency set k_x, k_y, k_z corresponding to a plane wave with wave vector $\mathbf{k} = (k_x, k_y, k_z)$. The time dependence of the monochromatic field components is given by $\exp\{-i\omega t\}$ and will be generally omitted when using the complex representation of time-harmonic fields. The result of the dispersion relation at frequency ω yields the relationship $k_x^2 + k_y^2 + k_z^2 = n^2 k_0^2 = k^2$ with n the (complex) refractive index of the medium. We now define the two-dimensional forward and inverse Fourier transforms of the complex field $\mathbf{E}(\mathbf{r})$ according to (see Fig. 2.1 for the geometry of the problem)

$$\tilde{\mathbf{E}}(z^{'}; k_x, k_y) = \iint_{-\infty}^{+\infty} \mathbf{E}(x', y', z') \exp\{-i[k_x x' + k_y y']\} dx' dy', \tag{2.1}$$

$$\mathbf{E}(x', y', z') = \frac{1}{(2\pi)^2} \iint_{-\infty}^{+\infty} \tilde{\mathbf{E}}(z^{'}; k_x, k_y) \exp\{i[k_x x' + k_y y']\} dk_x dk_y \ . \tag{2.2}$$

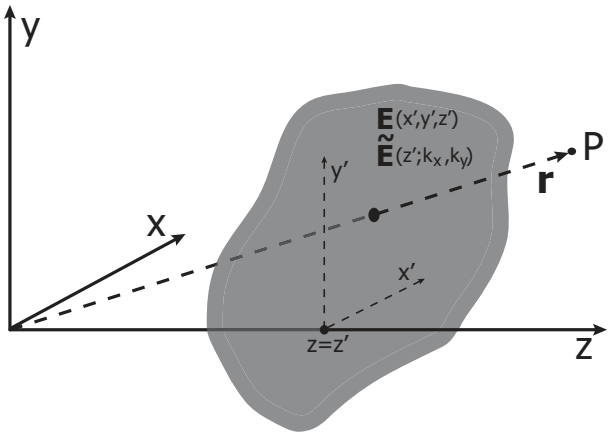

Fig. 2.1. The field distribution $\mathbf{E}(\mathbf{r}^{'})$ and its two-dimensional spatial Fourier transform $\tilde{\mathbf{E}}(z';k_x,k_y)$ are given in the plane $z=z^{'}$. The field has to be calculated in an arbitrary point P, given by the general position vector $\mathbf{r}$.

Using the Fourier transform $\tilde{\mathbf{E}}(z^{'};k_x,k_y)$ in the plane $z=z'$, the field in a general point P with position vector $\mathbf{r}$ is given by

$$\mathbf{E}(x,y,z;z') = \frac{1}{(2\pi)^2}\iint_{-\infty}^{+\infty}\tilde{\mathbf{E}}(z^{'};k_x,k_y)\times \exp\{i[k_x x+k_y y+k_z(z-z^{'})]\}dk_x dk_y\ , \quad (2.3)$$

where the value of k_z equals $\sqrt{k^2-k_x^2-k_y^2}$ for $k_x^2+k_y^2\leq k^2$ and $+i\sqrt{k_x^2+k_y^2-k^2}$ for $k_x^2+k_y^2>k^2$.
The relationship between the propagation method using a Fourier-based plane wave expansion and the physically more intuitive Huygens' spherical wavelet model can be established by using Weyl's result [Weyl (1919)] for the plane wave expansion of a spherical wave,

$$\frac{\exp(ikr)}{r} = \frac{i}{2\pi}\iint_{-\infty}^{+\infty}\frac{\exp\{i[k_x x+k_y y+k_z z]\}}{k_z}dk_x dk_y\ , \quad (2.4)$$

where $r=(x^2+y^2+z^2)^{1/2}$. A proof of Weyl's result is given in Appendix A. The dual approach to wave propagation has been more systematically described in well-known textbooks like [Born, Wolf (2002)] and [Stamnes (1986)], especially in the context of focused fields. To illustrate the connection between both approaches we follow the arguments in [Stamnes (1986)] and study the propagated field in the case that not the field itself is given in the plane $z=z'$ but its derivative with respect to z, $\partial\mathbf{E}(x,y,z;z')/\partial z$. Using Eq.(2.3), taking

the z-derivative and then putting $z = z'$, we find

$$\frac{\partial \mathbf{E}(x, y, z'; z')}{\partial z} = \frac{1}{(2\pi)^2} \iint_{-\infty}^{+\infty} ik_z \tilde{\mathbf{E}}(z^{'}; k_x, k_y) \exp\{i[k_x x + k_y y]\} dk_x dk_y \ . \quad (2.5)$$

Taking the Fourier transform of this quantity we find after some manipulation the following relationship

$$FT\left[\frac{\partial \mathbf{E}(x, y, z'; z')}{\partial z}\right] = \tilde{\mathbf{E}}_d(z'; k_x, k_y) = ik_z \tilde{\mathbf{E}}(z^{'}; k_x, k_y) \ , \quad (2.6)$$

where the subscript d indicates that we have taken the Fourier transform of the z-derivative of the field. The propagated field according to Eq.(2.3) is now alternatively written as

$$\mathbf{E}(x, y, z; z') = \frac{1}{(2\pi)^2} \iint_{-\infty}^{+\infty} \tilde{\mathbf{E}}_d(z^{'}; k_x, k_y) \times \frac{\exp\{i[k_x x + k_y y + k_z(z - z^{'})]\}}{ik_z} dk_x dk_y \ . \quad (2.7)$$

Following [Sherman (1967)], the above expression is interpreted as a the Fourier transform of the product of two functions that can be put equal to the convolution of their transforms

$$\begin{aligned} f(x, y) &= \frac{1}{(2\pi)^2} \iint_{-\infty}^{+\infty} F_1(k_x, k_y) F_2(k_x, k_y) \exp\{i[k_x x + k_y y]\} dk_x dk_y \\ &= \iint_{-\infty}^{+\infty} f_1(x', y') f_2(x - x', y - y') dx' dy' \ , \end{aligned} \quad (2.8)$$

where the lower case functions are the inverse Fourier transforms of the corresponding capital functions.

By putting $F_1 = \tilde{\mathbf{E}}_{\mathbf{d}}(z^{'}; k_x, k_y)$ and $F_2 = \exp\{ik_z(z - z')\}/(ik_z)$ and using the result of Eq.(2.4) we find after some arrangement the expression

$$\mathbf{E}_d(x, y, z; z') = \frac{-1}{2\pi} \iint_{-\infty}^{+\infty} \frac{\partial \mathbf{E}(x, y, z'; z')}{\partial z} \times \frac{\exp\{ik[(x - x')^2 + (y - y')^2 + (z - z')^2]^{1/2}\}}{[(x - x')^2 + (y - y')^2 + (z - z')^2]^{1/2}} dx' dy' \ . \quad (2.9)$$

Like before, the subscript d indicates that the field has been obtained using the z-derivative values in the plane $z = z'$ as single-sided boundary conditions which means that we neglect any counter-propagating wave components.

It can be shown similarly that a comparable expression can be obtained when using the field values in the plane $z = z'$ as starting condition and this leads to the expression

$$\mathbf{E}_f(x,y,z;z') = \frac{-1}{2\pi} \iint_{-\infty}^{+\infty} \mathbf{E}(x',y',z';z') \times \frac{\partial}{\partial z}\left(\frac{\exp\{ik[(x-x')^2+(y-y')^2+(z-z')^2]^{1/2}\}}{[(x-x')^2+(y-y')^2+(z-z')^2]^{1/2}}\right) dx'dy' \ . \quad (2.10)$$

$\mathbf{E}_f(x,y,z;z')$ and $\mathbf{E}_d(x,y,z;z')$ are generally referred to as, respectively, the Rayleigh-I and Rayleigh-II diffraction integrals, based on the propagation of spherical waves or their z-derivatives. An equally weighted sum of both solutions leads to a third integral expression, the well-known Kirchhoff diffraction formula [Stamnes (1986)]. This relationship between the Rayleigh and Kirchhoff integrals is only valid if the assumption holds that there are no counter-propagating wave components.

These three equivalent representations of the propagated field remain directly applicable when the effective source area is limited by an aperture $\mathcal{A}$, see Fig. 2.2. The effect of this aperture is either included in the integration

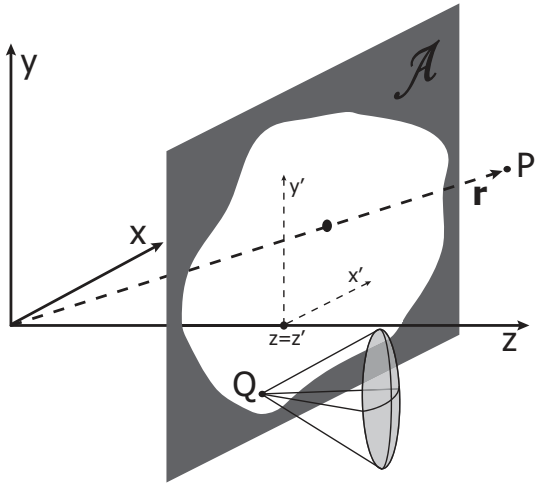

Fig. 2.2. The field propagated to a general point P in the presence of an obstructing aperture $\mathcal{A}$ in the plane $z = z'$ where the incident field is given. A portion of a secondary spherical wave, emanating from a general point Q in the aperture, has been schematically indicated.

range or it is accounted for by adding a multiplying 'aperture' function in the integrand of the diffraction integrals. If necessary, this aperture function is complex to account for possible phase changes introduced on the passage of

the radiation through the aperture.

2.2 The Debye integral for focused fields

When calculating a point-spread function, the field in the aperture is basically a spherical wave converging to the focal point F. Especially for high-numerical-aperture focused beams, it is customary to use the plane wave expansion based integral of Eq.(2.3) to calculate the focal field distribution. The focusing incident wave passes through the diaphragm $\mathcal{A}$ and produces a diffraction image in the focal region near F, see Fig. 2.3. We now temporarily restrict

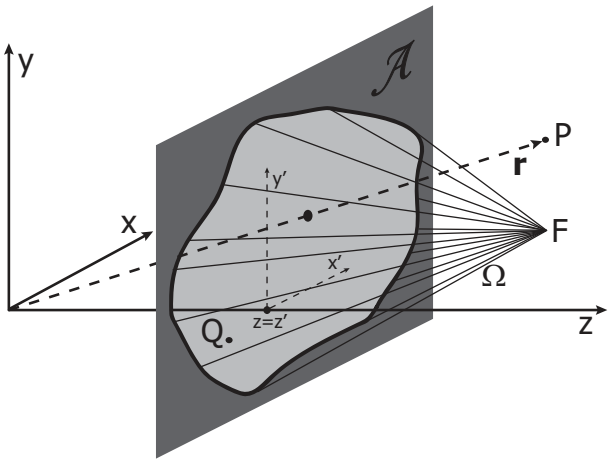

Fig. 2.3. The incident field is a spherical wave focused at the point $F(x_f, y_f, z_f)$ with the incident field in a general point Q given by Eq.(2.11). The diffracted field in a point P is calculated by means of an integration over the solid angle Ω that is determined by the lines joining the rim of the aperture A and the focal point F.

ourselves to a scalar wave phenomenon, characterized by a single quantity E to describe the field. We suppose that the field in the aperture is given by

$$E_{\mathcal{A}}(x', y', z') = E_0(x', y') \frac{\exp\{-ikR_{QF}\}}{R_{QF}} \,, \tag{2.11}$$

with R_{QF} given by the distance from a general point Q in the aperture with coordinates (x', y', z') to the focal point $F(x_f, y_f, z_f)$. The function $E_0(x', y')$ (dimension is field strength times meter) accounts for any perturbations of the incident spherical wave in amplitude or phase; for a perfectly spherical wave we have $E_0(x', y') \equiv 1$. The minus sign in the exponential for a converging wave stems from the choice of the phase reference point that is commonly the focal point F.

The angular spectrum of the field in the aperture is given by

$$\tilde{E}(z';k_x,k_y)=\iint\limits_{\mathcal{A}} E_0(x',y')\frac{\exp\{-ikR_{QF}\}}{R_{QF}}\exp\{-i[k_xx'+k_yy']\}dx'dy', \tag{2.12}$$

where possible aberrations or aperture transmission variations can be incorporated in the function $E_0(x',y')$. The field limitation by the aperture boundary is geometrically 'sharp', not taking into account possibly more smooth electromagnetic boundary conditions. This so-called 'hard' Kirchhoff boundary condition is adequate when the typical dimension of the aperture is many wavelengths large, a condition satisfied in most practical optical imaging systems.

The angular spectrum of the function $\tilde{E}(z';k_x,k_y)$ basically extends to infinity, among others because of the hard Kirchhoff boundary condition. This is a serious complication when carrying out the integration of Eq.(2.3). A frequently used approximation for $\tilde{E}(z';k_x,k_y)$, originally proposed by [Debye (1909)], is

$$\tilde{E}(z';k_x,k_y)=\begin{cases}\left(\frac{2\pi}{ik_z}\right)E_0\{x_f-\frac{k_x}{k_z}(z_f-z'),y_f-\frac{k_y}{k_z}(z_f-z')\}\times \\ \qquad\qquad \exp\{-i[k_xx_f+k_yy_f+k_z(z_f-z')]\}, & \text{inside } \Omega \\ 0, & \text{outside } \Omega\end{cases} \tag{2.13}$$

where $\mathbf{r}_f=(x_f,y_f,z_f)$ is the position vector of the focal point F and Ω denotes the solid angle that the aperture subtends at F. The solid angle Ω equals the solid angle of the cone of light created by the incident spherical wave after truncation by the aperture following the laws of geometrical optics.

The expression of Eq.(2.13) can be obtained by an asymptotic expansion of Eq.(2.12) for the aberration-free case by finding the stationary points of the phase function [Stamnes (1986)]. In Appendix B we give the expression for $\tilde{E}(z';k_x,k_y)$ in the presence of an aberrated incident wave. The diffraction integral of Eq.(2.3) now becomes

$$E(x,y,z;z')=\frac{-i}{2\pi}\iint\limits_{\Omega}\frac{E_0\{(x_f-\frac{k_x}{k_z}(z_f-z'),y_f-\frac{k_y}{k_z}(z_f-z')\}}{k_z}\times \\ \exp\{i[k_x(x-x_f)+k_y(y-y_f)+k_z(z-z_f]\}dk_xdk_y. \tag{2.14}$$

In most cases, the coordinate z' will be that of the center of the aperture plane and then equals zero.

The Debye approximation thus is equivalent to the introduction of a sharp boundary in the plane wave spectrum following from geometrical optics arguments. It has been shown by [Stamnes (1986)] that the Debye approximation is equivalent to an asymptotic value of the integral of Eq.(2.3) where only the interior stationary point has been kept. The conditions of applicability of the Debye approximation have been examined in [Wolf, Li (1981)]. The result of their analysis is that the Debye integral is a sufficient approximation to the field values in the focal region if the condition $z_f - z' \gg \pi/\{k \sin^2(\alpha_m/2)\}$ is fulfilled with $\sin \alpha_m = s_0$ equal to the numerical aperture of the focusing wave divided by the refractive index of the medium (see also fig. 2.4 for the definition of numerical aperture and s_0).

2.3 The Rayleigh-I integral for focused fields

In this Subsection, we will focus on the first version of the Rayleigh diffraction integrals, the so-called Rayleigh-I intgeral. For an incident focused field, this intgeral is obtained by the substitution of Eq.(2.11) in Eq.(2.10) and, including the aberration phase $\Phi(x', y')$ introduced in Appendix B, we get

$$E_f(x, y, z; z') = \frac{-i}{\lambda} \iint_{\mathcal{A}} \frac{z - z'}{R_{QP}^2 R_{QF}} E_0(x', y') \exp\{i\Phi(x', y')\} \times \exp\{ik(R_{QP} - R_{QF})\} dx' dy', \tag{2.15}$$

where $Q(x', y', z')$ again is the general point in the diffracting aperture $\mathcal{A}$ and $(z - z')/R_{QF}$ can be recognized as an obliquity factor for the strength of the emitted secondary waves. The integral expression above neglects the diffracted near-field contribution, but for $kR_{QP} >> 1$, it is sufficiently accurate if the Kirchhoff boundary conditions apply.

A direct comparison of the Rayleigh and Debye integral expressions can be carried out by transforming the Debye integral of Eq.(2.14) from an integration over the (k_x, k_y)-domain back to the (x', y')-domain in the planar diffracting aperture $\mathcal{A}$. With the focal point F located on the z-axis, the relation between the coordinates (x', y') and the wave vector components (k_x, k_y) is given by, see Fig. 2.4,

$$k_x = \frac{k_z}{z_f - z'} x' = -\frac{k}{R_{QF}} x', \qquad k_y = \frac{k_z}{z_f - z'} y' = -\frac{k}{R_{QF}} y', \tag{2.16}$$

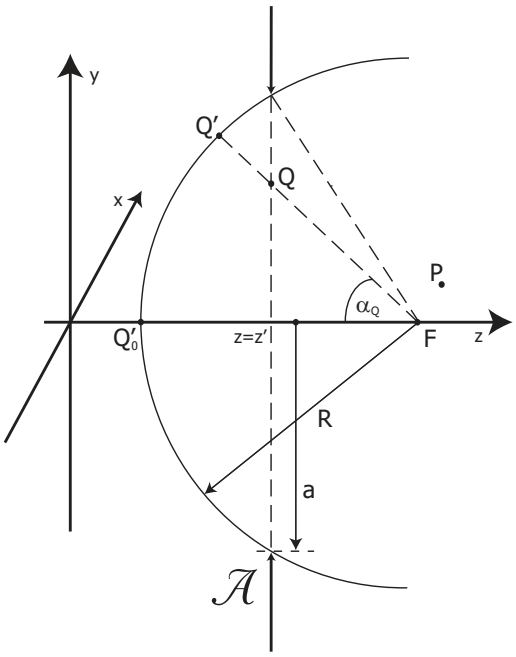

Fig. 2.4. Schematic drawing of the aperture $\mathcal{A}$ limiting the incident wave with its focus in the axial point F. The possible amplitude and phase variation over the beam cross-section in $\mathcal{A}$ are preferably measured or calculated on the exit pupil sphere with radius R, centered in F and intersecting the z-axis in the point $Q_0^{'}$. In the figure, the aperture cross-section is chosen to be circular but a more general shape can also be accommodated.

with $R_{QF}^2{=}x^{'2} + y^{'2} + (z_f - z^{'})^2$. The Jacobian of the transformation yields $dk_x dk_y{=}dx^{'}dy^{'}\ k^2(z_f - z^{'})^2/R_{QF}^4$ and, with $k_z = k\cos\alpha_Q = k(z_f - z^{'})/R_{QF}$ and after some rearrangement, we find the transformed Debye integral according to

$$E(x,y,z;z') = \frac{-i}{\lambda}\iint\limits_{\mathcal{A}} \frac{z_f - z^{'}}{R_{QF}^3} E_0(x^{'},y^{'})\exp\{i\Phi(x^{'},y^{'})\}\times \exp\{i\mathbf{k}\cdot(\mathbf{r}_{QP}-\mathbf{r}_{QF})\}dx^{'}dy^{'}, \tag{2.17}$$

with the aberration function Φ of the incident wave explicitly included in the integral and the components of the vector $\mathbf{k}$ defined by Eq.(2.16).

Discrepancies between the Rayleigh-I and the Debye integral are found in the amplitude or obliquity factor where the difference between R_{QP} and R_{QF} and the difference between z and z_f is neglected in the Debye expression. Another important difference is found in the pathlength exponential. The pathlength difference $R_{QP} - R_{QF}$ of the Rayleigh-I integral is approximated by the scalar product $\mathbf{s}\cdot(\mathbf{r}_{QP} - \mathbf{r}_{QF})$ with $\mathbf{s}$ the unit vector in the propagation direction. Like for the obliquity factor above, the expressions are sufficiently accurate when P and F are close and R is very large with respect to λ. The pathlength expression in the Debye integral is exact if $R \to \infty$ and it then corresponds

to the pathlength definition along a geometrical ray given by Hamilton in the framework of his eikonal functions [Born, Wolf (2002)]. The evaluation of the function $E_0(x^{'}, y^{'})\ \exp\{i\Phi(x^{'}, y^{'})\}$ can be carried out in the plane of the aperture $\mathcal{A}$ by measuring in $\mathcal{A}$ the amplitude and phase differences between the actual wave and the ideal spherical wave. The function $E_0 \exp(i\Phi)$ carries the information about the amplitude and phase of the bundles of rays that have been traced through the optical system. These quantities are preferably defined on the exit pupil sphere of the optical system, the sphere with radius R, centered on F in Fig. 2.4 and truncated by the physical aperture $\mathcal{A}$.

2.4 Comparison of the various diffraction integrals

A comparison of the various diffraction integrals for focused fields leads to the following order in terms of accuracy and degree of approximation

- *Rayleigh-I integral*
  The Rayleigh-I integral according to Eq.(2.15) is the most accurate one, within the framework of scalar diffraction theory. The integral is related to the amplitude distribution in a plane. A comparable accurate integral can be obtained from Eq.(2.9), the so-called Rayleigh-II integral.
- *Debye integral*
  The Debye integral, Eq.(2.14), yields accurate results once the distance from pupil to focal point is large ($Q_0^{'}F = R \to \infty$) and the aperture of the cone of plane waves is sufficiently large. The angular spectrum is truncated according to the geometrical optics approximation, but this truncation has less and less influence when R increases (see [Wolf, Li (1981)] for the residual error of this integral). The functions E_0, see Eq.(2.14), accounts for a non-uniform (complex) amplitude of the incident spherical wave.

A numerical comparison of the axial intensity in the focal region according to the Rayleigh-I and the Debye integral is given in Fig. 2.5. The graphs in the upper, middle and lower row apply to increasing aperture diameters of 10λ, 100λ and $10^5\lambda$, respectively. In the left column of the graphs, the numerical aperture $s_0 = \sin\alpha_m$ of the focused beam in free space is 0.25, in the right column 0.50. The plotted intensity patterns, in arbitrary units, have been normalized with respect to the most accurate result following from the Rayleigh-I integral (solid lines). The curve following from the Debye approximation of the diffraction integral is the dotted one. The variable plotted along the horizontal axis is the defocusing $(z - z_f)$ in units of λ. The two upper graphs show that

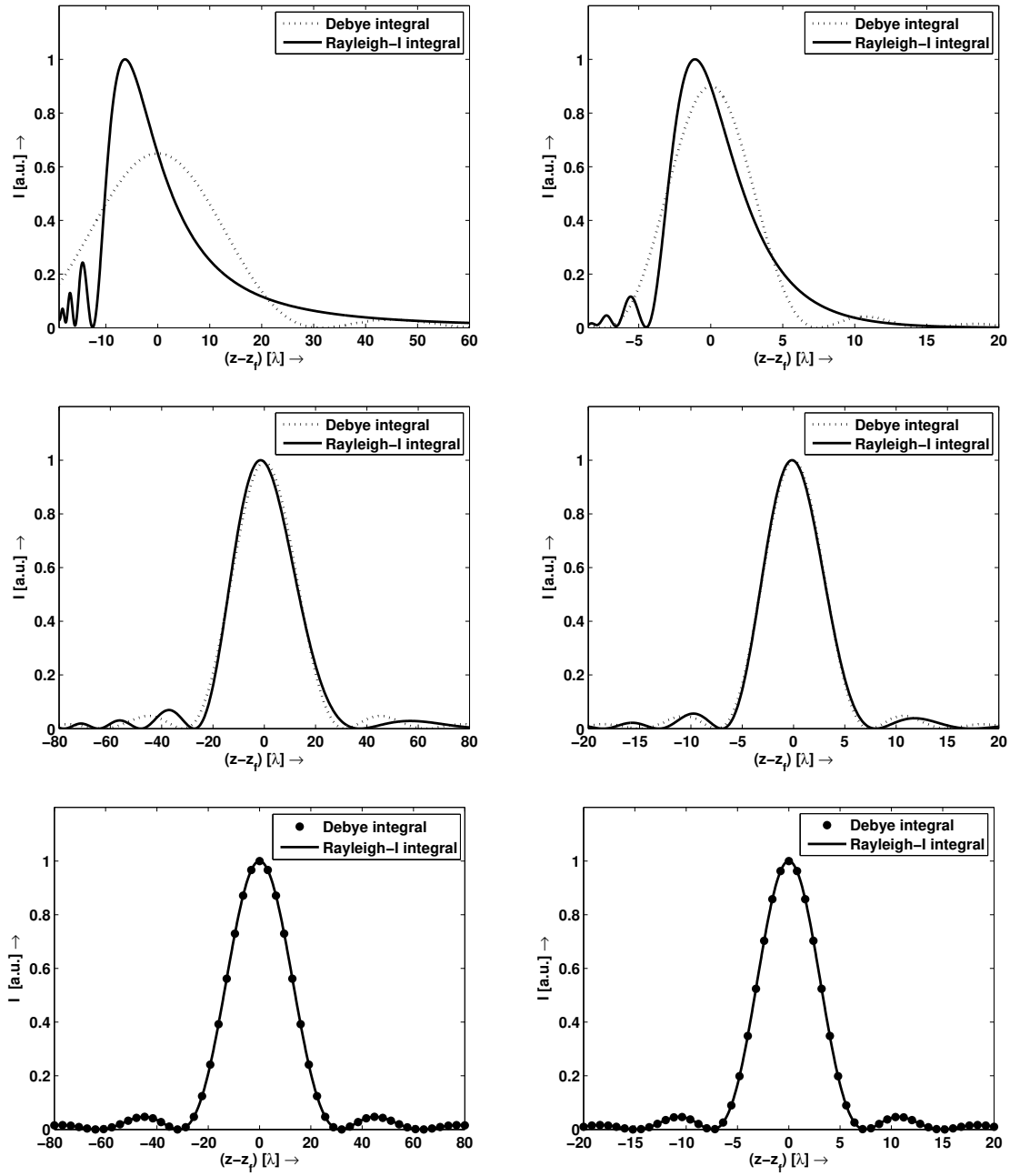

Fig. 2.5. The axial intensity in the focal region calculated according to the Rayleigh-I (solid lines) and the Debye integral expression (dotted lines). Upper row: aperture diameter $2a$ is 10 λ. In the middle row, the aperture diameter has been increased to 100 λ, in the lower row we have taken $2a = 10^5\lambda$. In the graphs on the left, the numerical aperture s_0 of the focusing beam in free space is 0.25, in the graphs on the right the value is 0.50. The intensity in arbitrary units has been normalized to the result of the Rayleigh-I integral. The defocusing $z - z_f$ has been plotted along the horizontal axis in units of the wavelength λ of the light.

for a very small aperture diameter the difference between the Rayleigh-I and Debye integral is large. The Rayleigh-I integral result leads to a strong asymmetry with respect to the nominal focus position and the highest intensity is at an axial position closer to the aperture than the nominal focal point F. These effects are relaxed by an increase of the numerical aperture as shown by

the upper right graph. The strong intensity oscillations at the negative defocus values $-20 \leq z - z_f \leq -10$ in the upper left graph correspond to axial points that are very close to the diffracting aperture itself. They can be explained by the interference effect between the wave diffracted from the circular rim of the aperture and the undiffracted focused wave, both having comparable amplitudes close to the aperture. The axial range beyond the intensity maximum and the focal point F does not show these deep oscillations because in this region the direct undiffracted spherical wave has, by far, the largest amplitude on axis. The effect of a higher numerical aperture is a less pronounced focus off-set of the Rayleigh-I integral; one also observes an increased fidelity of the Debye integral result regarding maximum intensity. An increase of the aperture diameter to 100λ makes the focus offset almost disappear, especially in the graph on the right with $s_0 = 0.50$. The asymmetry around focus in the position of the relative maxima is still visible, but the Debye approximation has strongly improved with respect to the upper row of graphs, also regarding its prediction of maximum intensity. The correspondence between both representations is increasingly better and beyond the value $2a = 500\lambda$ hardly any difference is noticeable. This is illustrated in the lower row of graphs that applies to the very large apertures encountered in practical optical systems, for instance $2a = 5$ mm with $\lambda = 0.5\ \mu m$. Here, we have plotted the Debye approximation results as dots and these coincide extremely well with the Rayleigh-I integral results in the range of numerical apertures that are of interest for high-resolution applications. It is for imaging systems in this domain that the quality assessment using point-spread functions will be carried out. The lower graphs show that in this case it is fully justified to resort to the analytically more accessible Debye integral.

- *Paraxial approximation of the Debye integral*
  The paraxial approximation to the Debye integral is allowed if the aperture shape is such that $k_z^2 \gg (k_x^2 + k_y^2)$ within the cone of integration Ω, see Eq.(2.14). The k_z-factor in the nominator of the integrand is put equal to k. The variables (k_x, k_y) are transformed according to $k_x = -k(x_s^{'}/R)$ and $k_y = -k(y_s^{'}/R)$ with $(x_s^{'}, y_s^{'})$ cartesian coordinates on the exit pupil sphere through $Q_0^{'}$ with radius R that has its midpoint in the focal point F, located on the z-axis, see Fig. 2.4. After some manipulation and expanding the square root for k_z in the pathlength exponential up to the first power we obtain

$$E_f(x, y, z; z') \approx \frac{-i}{\lambda R^2} \exp\{ik(z - z_f)\} \exp\left\{ik\frac{(x^2 + y^2)}{2R}\right\} \times$$

$$\iint_{\mathcal{A}} \exp\left\{-ik(z-z_f)\frac{(x_s^{'2}+y_s^{'2})}{2R^2}\right\} E_s(x_s^{'},y_s^{'}) \times$$
$$\exp\{i\Phi_s(x_s^{'},y_s^{'})\} \exp\left\{-ik\frac{xx_s^{'}+yy_s^{'}}{R}\right\} dx_s^{'}dy_s^{'}. \tag{2.18}$$

The amplitude function $E_s(x_s^{'},y_s^{'})$ and phase function $\exp\{i\Phi_s(x_s^{'},y_s^{'})\}$, describing the departure of the complex amplitude of the focusing wave from that of a uniform spherical wave, are now defined on the exit pupil sphere where they can easily be calculated or measured.

The paraxial approximation of Eq.(2.18) is often modified to allow the use of dimensionless coordinates. The aperture coordinates are normalized with respect to the lateral dimension a of the aperture. The lateral field coordinates of the image point P are normalized with respect to the quantity $\lambda R/a$ or λ/s_0, the diffraction unit in the focal region ($s_0 = \sin\alpha_{max} = a/R$ is the numerical aperture of the focusing beam). The axial coordinate z is normalized with respect to the axial diffraction unit, $\lambda/(\pi s_0^2)$. With these transformations we find

$$E_f(x_n,y_n,z_n) \approx \frac{-is_0^2}{\lambda} \exp\left\{\frac{i2(z_n-z_{n,f})}{s_0^2}\right\} \exp\left\{i\frac{\pi\lambda}{Rs_0^2}(x_n^2+y_n^2)\right\} \times$$
$$\iint_{\mathcal{A}_n} \exp\left\{-i(z_n-z_{n,f})(x_n^{'2}+y_n^{'2})\right\} E(x_n^{'},y_n^{'}) \times$$
$$\exp\{i\Phi(x_n^{'},y_n^{'})\} \exp\left\{-i2\pi(x_nx_n^{'}+y_ny_n^{'})\right\} dx_n^{'}dy_n^{'}. \tag{2.19}$$

Using normalized polar coordinates (ρ,θ) in the aperture and cylindrical coordinates (r,ϕ,f) in the focal region (origin of the normalized axial coordinate f is in F) yields the expression

$$E_f(r,\phi,f) \approx \frac{-is_0^2}{\lambda} \exp\left\{\frac{i2f}{s_0^2}\right\} \exp\left\{i\frac{\pi\lambda r^2}{Rs_0^2}\right\} \times$$
$$\iint_{\mathcal{A}_n} \exp\left\{-if\rho^2\right\} E(\rho,\theta) \exp\{i\Phi(\rho,\theta)\} \times$$
$$\exp\left\{-i2\pi r\rho\cos(\theta-\phi)\right\} \rho d\rho d\theta, \tag{2.20}$$

where the amplitude and aberration functions in cartesian coordinates now have been replaced by their analoga in polar coordinates.

The intensity distribution in the point-spread function strongly depends on the departure of the incident focusing wave from its reference shape, that of a spherical wave with a uniform amplitude. In this subsection we discuss, especially for the high-numerical-aperture case, the various factors that influence the complex amplitude distribution of the focusing wave, measured in the exit pupil of the imaging system. We also discuss the various methods for representing the wavefront aberration on the exit pupil sphere.

2.5.1 Amplitude distribution in the exit pupil

For the calculation of the amplitude in the focal region of an optical imaging system we need the complex amplitude distribution on the exit pupil sphere of the system. In most practical case, we are able to specify the complex amplitude distribution on the entrance pupil sphere or on the entrance pupil plane in the frequently occurring case that the object conjugate of the system is at infinity. The transfer of complex amplitude from entrance to exit pupil depends on numerous factors like diaphragm shape, reflection losses at the intermediate optical surfaces, light absorption in the lens materials, etc. These effects, particular for each optical system, can be accounted for in the complex transmission function $E(\rho, \theta)\, \exp\{i\Phi(\rho, \theta)\}$. A more general aspect is the pupil imaging telling us how the complex amplitude distribution in object space is mapped to the exit pupil sphere in image space. In Fig. 2.6 we show the geometry that is relevant for this mapping process from object to image space. Several options may occur in practical systems. To study these options, we consider the intensities in an annular region of the entrance pupil and the corresponding annulus on the exit pupil sphere. The more general situation with a finite object distance and a spherical entrance pupil surface does not basically change the result. Supposing loss-free light propagation, the relation between the power flow through the annular regions of entrance pupil and exit pupil is given by

$$2\pi I_0\, r_0 dr_0 = 2\pi p(\alpha) I_1 R^2 \sin\alpha d\alpha, \tag{2.21}$$

where $r_0 = \sqrt{x_0^2 + y_0^2}$ is a function of α that determines the mapping effect and the ratio $I_1/I_0 = (f_L/R)^2$ follows from the paraxial magnification between the exit pupil and entrance pupil (f_L is the focal distance of the imaging system).

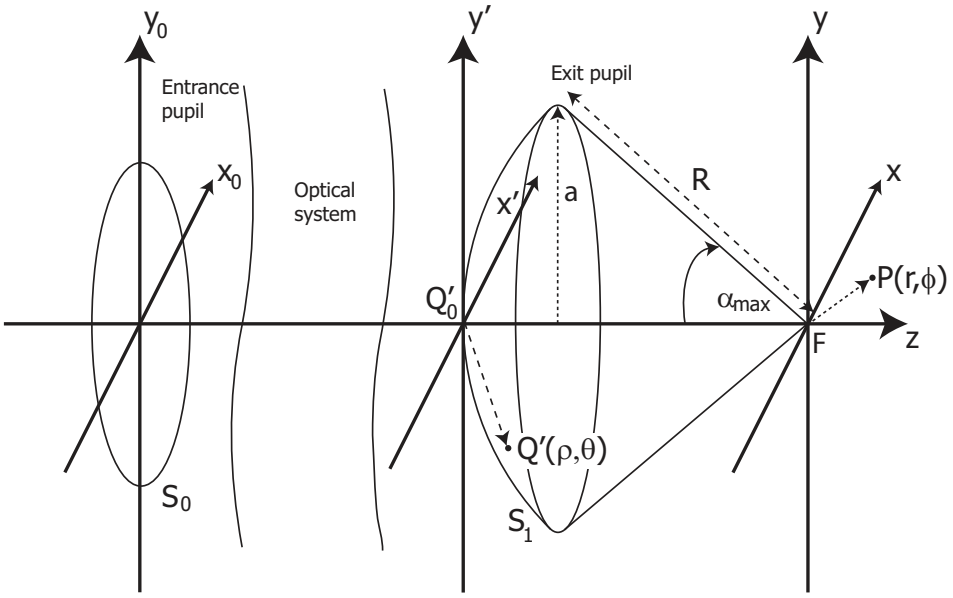

Fig. 2.6. An incident wave is described by its complex amplitude on the entrance pupil sphere S_0 (flat in this picture with the object point at infinity) and propagates from the entrance pupil through the optical system towards the exit pupil sphere S_1 and to the focal region with its center in F. The co-ordinates in object and image space are referred to by (x_0, y_0, z_0) and (x, y, z), respectively, with respect to the origins in object and image space. The general point Q' on the exit pupil sphere is defined by means of its polar coordinates (ρ, θ) with respect to the z-axis. The aperture of the imaging pencil (diameter $2a$) is given by $s_0 = \sin\alpha_{max}$. The distance from $Q_0^{'}$ to F is denoted by R with the origin for the z'-coordinate on the exit pupil sphere chosen in $Q_0^{'}$.

The function $p(\alpha)$ is unity on axis but can deviate from this value for $\alpha \neq 0$ to account for non-paraxial behaviour of finite rays in the imaging system. The integration of Eq.(2.21) from 0 to a general aperture value given by $\sin\alpha$ yields

$$r_0^2 = f_L^2 \int_0^{\alpha} p(\alpha) \sin\alpha d\alpha. \tag{2.22}$$

We consider two options

- $p(\alpha) = 1$, yielding

$$r_0 = 2 f_L \sin(\alpha/2) \qquad \text{Herschel's condition} \tag{2.23}$$

- $p(\alpha) = \cos\alpha$, yielding

$$r_0 = f_L \sin\alpha \qquad \text{Abbe's sine-condition} \tag{2.24}$$

The two pupil imaging conditions applying to non-paraxial rays have already been proposed in the nineteenth century. They emerge as special cases in the framework of general isoplanatic imaging conditions, see [Welford (1986)]. Outside the paraxial imaging regime, the Herschel condition favors the imaging of

axial points in front and beyond F; the Abbe sine-condition has been designed to guarantee good imaging for image points in the focal image plane through F. The vast majority of optical systems obeys the Abbe sine condition and for this reason, in the following, we will adhere to the condition $p(\alpha) = \cos(\alpha)$. The function $p(\alpha)$ pertains to the ratio of intensities. In the case of a uniform amplitude distribution in the entrance pupil, we will thus apply the rule, with $\cos^2\alpha = (1 - s_0^2\rho^2)$, that the amplitude function on the exit pupils sphere, $E(\rho, \theta)$, contains a factor $(1 - s_0^2\rho^2)^{1/4}$. This amplitude factor is often referred to as the radiometric effect. As defined before, ρ is the normalized radial coordinate on the exit pupil sphere.

2.5.2 Phase distribution in the exit pupil

The aberration function $\Phi(\rho, \theta)$ originates from the possible aberration that is already present in the incident beam and from the aberration imparted to the beam on its traversal of the optical system. It is common practice to effectively project back the effect on the aberration of all optical surfaces and media in the system onto the exit pupil sphere, yielding the global aberration function $\Phi(\rho, \theta)$ of the system. For sufficiently small aberrations, typically $\Phi \leq 2\pi$, this method is allowed.

The representation of the aberration function has its particular history. From the start of modern aberration theory by Seidel, see [Welford (1986)], based on a power series expansion of optical pathlength differences in an optical system, it was common practice to represent Φ as

$$\Phi(\rho, \theta) = \sum a_{kl}\rho^k \cos^l(\theta). \tag{2.25}$$

Certain combinations of k and l yield a characteristic aberration. This is more or less true for the lowest order aberration types that occur in an optical system with rotational symmetry when $k + l = 4$. But for higher order aberration terms, the expression of Eq.(2.25) becomes rather confusing because of the non-orthogonality of the expansion in both ρ and θ. A breakthrough in aberration theory is due to advent of the Zernike circle polynomials, see references [Zernike (1934)]-[Nijboer (1942)], and the expansion for Φ now reads

$$\Phi(\rho, \theta) = \sum_{nm} R_n^m(\rho) \left\{ \alpha_{n,c}^m \cos m\theta + \alpha_{n,s}^m \sin m\theta \right\}, \tag{2.26}$$

where $R_n^m(\rho)$ is the radial Zernike polynomial of radial order n and azimuthal order m with $n, m \geq 0$ and $n - m$ even. An alternative representation is

$$\Phi(\rho, \theta) = \sum_{nm} \alpha_n^m \; R_n^{|m|}(\rho) \; \exp\{im\theta\}, \tag{2.27}$$

where $n \geq 0$, $(n - |m|)$ even, and m now also assumes negative values. This latter expansion will be used and, more generally, we will also allow complex coefficients α_n^m so that a complex function $\Phi(\rho, \theta)$ can be expanded. The relationship between the now equally complex coefficients $\alpha_{n,c/s}^m$ and the α_n^m is then given by

$$\begin{aligned}
\Re(\alpha_{n,c}^m) &= \Re(\alpha_n^m + \alpha_n^{-m}) \\
\Im(\alpha_{n,c}^m) &= \Im(\alpha_n^m + \alpha_n^{-m}) \\
\Re(\alpha_{n,s}^m) &= -\Im(\alpha_n^m - \alpha_n^{-m}) \\
\Im(\alpha_{n,s}^m) &= \Re(\alpha_n^m - \alpha_n^{-m}).
\end{aligned} \tag{2.28}$$

Other representations of the complex amplitude on the exit pupil sphere have been proposed. We mention the expansion of the far-field using 'multipole waves', see [Sheppard, Török (1997)]. As a function of the azimuthal and elevation angles on the exit pupil sphere, the far-field is described with the aid of spherical harmonics. The coefficients that yield the optimum far-field match are then used to propagate the multipole waves towards and beyond the focal point. The propagation as a function of the distance r is described in terms of well-behaving spherical Bessel functions of various orders. So far, the analysis has been restricted to circularly symmetric geometries with amplitude (transmission) variation on the exit pupil and to an infinitely distant exit pupil. But the method can be extended to more general geometries and to aberrated waves. The method is applicable not only to scalar diffraction problems but equally well to high numerical aperture systems requiring a vector diffraction treatment and can be extended to birefringent media, see [Stallinga (2004-1)].

Another representation uses the so-called Gauss-Laguerre polynomials that are orthogonal on the interval $[-\infty < r < +\infty]$ and emerge as eigenfunctions of the solution of the paraxial wave equation according to [Siegman (1986)]. They have been further studied in [Barnett, Allen (1994)] to make them suitable for the non-paraxial case . We will not further consider this type of amplitude and aberration representation because its Gaussian shape is not well suited for the hard-limited aperture functions that are mostly encountered in optical imaging systems. But the Gauss-Laguerre elementary solutions with

azimuthal order number $m \neq 0$ are well suited to represent a phase departure of the pupil function that shows a so-called helical phase profile with a phase jump of $2m\pi$. This is interesting when discussing optical beams with orbital angular momentum, see for instance [Beijersbergen, Coerwinkel, Kristensen, Woerdman (1994)]. However, using the Zernike polynomial representation of Eq.(2.27) with the exponential azimuthal dependence, it is equally well possible to represent helical phase profiles by selecting a single nonzero α_n^m-coefficient instead of an automatic combination of α_n^m and α_n^{-m}.

Using the appropriate expressions for the amplitude and aberration function on the exit pupil sphere we are now able to evaluate Eq.(2.20) and to obtain the amplitude of the scalar point-spread function in the paraxial approximation. It is possible to extend the scalar integral of Eq.(2.20) beyond the paraxial domain by incorporating the defocus exponential of Eq.(2.14) according to

$$\exp\{ik_z(z-z_f)\} = \exp\{ik\sqrt{1-\frac{k_x^2+k_y^2}{k^2}}(z-z_f)\}. \tag{2.29}$$

With the same coordinate transformation as used in deriving Eq.(2.18) and switching to the normalized polar coordinates (ρ, θ) on the exit pupil sphere, we obtain

$$\exp\{ik_z(z-z_f)\} = \exp\{ik\sqrt{1-s_0^2\rho^2}\ (z-z_f)\}. \tag{2.30}$$

The axial coordinate $z - z_f$ is normalized in the high numerical aperture case according to

$$z - z_f = -\frac{f}{ku_0}, \tag{2.31}$$

with $u_0 = 1 - \sqrt{1-s_0^2}$ and one then finds the final expression for the high-numerical-aperture defocus exponential, viz.

$$\exp\{ik_z(z-z_f)\} = \exp\left[-i\frac{f}{u_0}\right]\ \exp\left\{i\frac{f}{u_0}\left[1-\sqrt{1-s_0^2\rho^2}\right]\right\}. \tag{2.32}$$

The scalar integral for high-numerical-aperture then reads

$$E_f(r,\phi,f) \approx \frac{-is_0^2}{\lambda}\exp\left\{\frac{-if}{u_0}\right\}\exp\left\{i\frac{\pi\lambda r^2}{Rs_0^2}\right\} \times$$

$$\iint_{\mathcal{A}_n} \exp\left\{if\left(\frac{1-\sqrt{1-s_0^2\rho^2}}{u_0}\right)\right\} E(\rho,\theta)\exp\{i\Phi(\rho,\theta)\}\times \exp\left\{-i2\pi r\rho\cos(\theta-\phi)\right\}\rho d\rho d\theta, \tag{2.33}$$

where the complex amplitude angular spectrum function $E(\rho,\theta)\exp\{i\Phi(\rho,\theta)\}$ is again evaluated on the exit pupil sphere using the data from ray tracing or other propagation methods of the wave through the optical system. In several instances in the literature, the minus sign in the exponential with the factor $\cos(\theta-\phi)$ in Eq.(2.33) has also been suppressed. This means that the results apply to an azimuth shift of π for the axis $\phi = 0$ in image space. In Section 3 and further of this chapter, we will adhere to this latter sign convention. The integral above is an improvement with respect to the paraxial approximation, beyond an aperture of 0.60, at the condition that polarization effects are not dominating. In practice, this might be the case when the optical system is illuminated with effectively unpolarized or 'natural' light.

2.5.3 The high-numerical-aperture vector point-spread function

The extension of the point-spread function analysis to the vector components of the electrical and magnetic fields was first carried out in [Ignatowsky (1919)]. In a series of three papers he analyzed the electromagnetic field in the focus of a parabolic mirror and in the focus of a general imaging system. He also analyzed the amplitude conversion from entrance to exit pupil following from the various pupil imaging conditions, see Eqs.(2.23)-(2.24). The subject was reformulated and cast in the form of a generalized Debye integral by [Wolf (1959)] and [Richards, Wolf (1959)], applied to an optical system that is illuminated by a parallel beam from infinity with the optimum focus of the point-spread function in the geometrical focal point F. The Debye integral is used to solve the diffraction problem for each cartesian vector component of the fields. The vector components of the fields on the exit pupil sphere are obtained using the condition of Abbe for the mapping of the field components from the entrance pupil to the exit pupil (aplanatic imaging). From the geometry of the problem, see Fig. 2.7, one easily derives the required unit vectors in image space that are associated with the s- and p-polarization components

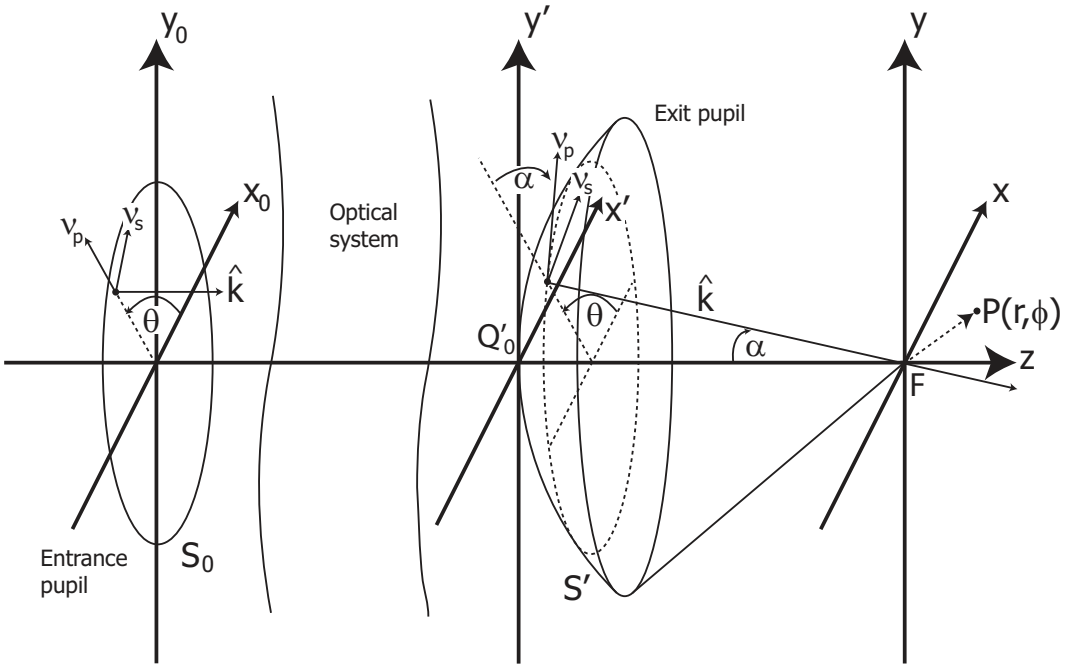

Fig. 2.7. Definiton of the orthogonal unit vector sets $(\nu_s, \nu_p, \hat{k})$ in entrance and exit pupil that are used to describe the components of the electromagnetic field vectors in the image space. The azimuthal plane defined by the angle θ is the plane of incidence. The origin for the exit pupil coordinates is chosen in $Q_0^{'}$ with Q a general point on the exit pupil sphere.

and the unit propagation vector

$$\nu_p = \begin{pmatrix} \cos\theta\cos\alpha \\ \sin\theta\cos\alpha \\ \sin\alpha \end{pmatrix} \quad \nu_s = \begin{pmatrix} \sin\theta \\ -\cos\theta \\ 0 \end{pmatrix} \quad \hat{\mathbf{k}} = \begin{pmatrix} -\cos\theta\sin\alpha \\ -\sin\theta\sin\alpha \\ \cos\alpha \end{pmatrix}. \tag{2.34}$$

The incident field is specified in terms of the linearly polarized electric components along the x_0- and y_0-axis in the entrance pupil according to $\mathbf{E} = a_0\hat{\mathbf{x}} + b_0\hat{\mathbf{y}}$, with a_0 and b_0 complex numbers to allow for an arbitrary state of polarization of the incident beam. The p- and s-polarization components of the field on the exit pupil sphere are now given by

$$\mathbf{E}_p \propto \{a_0\cos\theta + b_0\sin\theta\} \begin{pmatrix} \cos\theta\cos\alpha \\ \sin\theta\cos\alpha \\ \sin\alpha \end{pmatrix},$$

$$\mathbf{E}_s \propto \{a_0 \sin\theta - b_0 \cos\theta\} \begin{pmatrix} \sin\theta \\ -\cos\theta \\ 0 \end{pmatrix} \quad . \tag{2.35}$$

The x-, y- and z-components of the field on the exit pupil sphere is obtained by evaluating the scalar products with the cartesian unit vectors and this yields

$$\begin{aligned}
E_{s,x} &= \frac{f_L k_z^{1/2}}{2Rk^{1/2}} \left[a_0 \left\{ 1 + \frac{k_z}{k} - \cos 2\theta \left(1 - \frac{k_z}{k} \right) \right\} - b_0 \sin 2\theta \left(1 - \frac{k_z}{k} \right) \right] \\
E_{s,y} &= \frac{f_L k_z^{1/2}}{2Rk^{1/2}} \left[-a_0 \sin 2\theta \left(1 - \frac{k_z}{k} \right) + b_0 \left\{ 1 + \frac{k_z}{k} + \cos 2\theta \left(1 - \frac{k_z}{k} \right) \right\} \right] \\
E_{s,z} &= \frac{f_L k_r k_z^{1/2}}{Rk^{3/2}} \left(a_0 \cos\theta + b_0 \sin\theta \right) \ ,
\end{aligned} \tag{2.36}$$

with $k_r = k\sqrt{1 - k_z^2/k^2}$ and where we have included the amplitude mapping factor from the entrance to the exit pupil (see Subsection 2.5.1). The unit vector that points in the direction of the magnetic field is given by $\hat{\mathbf{h}}=\hat{\mathbf{k}} \times \hat{\mathbf{e}}$, yielding $\hat{h}_p = (\cos\alpha\cos\theta, \cos\alpha\sin\theta, \sin\alpha)$ and $\hat{h}_s = (-\sin\theta, \cos\theta, 0)$. The cartesian components of the magnetic induction are then given by

$$\begin{aligned}
B_{s,x} &= \frac{n_r f_L k_z^{1/2}}{2cRk^{1/2}} \left[-a_0 \sin 2\theta \left(1 - \frac{k_z}{k} \right) - b_0 \left\{ 1 + \frac{k_z}{k} - \cos 2\theta \left(1 - \frac{k_z}{k} \right) \right\} \right] \\
B_{s,y} &= \frac{n_r f_L k_z^{1/2}}{2cRk^{1/2}} \left[a_0 \left\{ 1 + \frac{k_z}{k} + \cos 2\theta \left(1 - \frac{k_z}{k} \right) \right\} + b_0 \sin 2\theta \left(1 - \frac{k_z}{k} \right) \right] \\
B_{s,z} &= \frac{n_r f_L k_r k_z^{1/2}}{cRk^{3/2}} \left(a_0 \sin\theta - b_0 \cos\theta \right) \ ,
\end{aligned} \tag{2.37}$$

with n_r the refractive index of the image space.

With the expressions for the electric and magnetic field components in terms of the wave vector components k_x and k_y, the Debye integral of Eq.(2.14), with $x_f = y_f = 0$, yields for the field components in the focal region near F

$$\begin{aligned}
\mathbf{E}(x,y,z) &= \frac{-i}{2\pi} \iint\limits_{\Omega} \frac{\mathbf{E_s}(-k_x,-k_y)}{k_z} \exp\{i[k_x x + k_y y + k_z(z - z_f)]\} dk_x dk_y \\
\mathbf{B}(x,y,z) &= \frac{-i}{2\pi} \iint\limits_{\Omega} \frac{\mathbf{B_s}(-k_x,-k_y)}{k_z} \exp\{i[k_x x + k_y y + k_z(z - z_f)]\} dk_x dk_y,
\end{aligned} \tag{2.38}$$

with $P(x, y, z)$ the coordinates of the considered point in the focal region. Using the more appropriate normalized cylindrical coordinates (ρ, θ) on the exit pupil sphere and (r, ϕ) in the focal region, we obtain

$$\mathbf{E}(r,\phi,f) = \frac{-is_0^2}{\lambda} \exp\left(\frac{-if}{u_0}\right) \iint\limits_C \frac{\mathbf{E_s}(\rho,\theta+\pi)}{(1-s_0^2\rho^2)^{1/2}} \times \exp\left\{\frac{if}{u_0}\left[1-(1-s_0^2\rho^2)^{1/2}\right]\right\} \exp\{i2\pi r\rho\cos(\theta-\phi)\}\rho d\rho d\theta, \tag{2.39}$$

with C the scaled integration area on the exit pupil sphere (in a standard situation equal to the unit circle); a comparable expression holds for the **B**-field components. In arriving at Eq.(2.39), we used Eq.(2.31) and the following coordinate transformations and normalizations,

$$\begin{aligned} k_x &= k_r\cos\theta = \rho k_{r,max}\cos\theta, & k_{r,max} &= ks_0, \\ k_y &= \rho k_{r,max}\sin\theta, \\ k_z &= (k^2-k_x^2-k_y^2)^{1/2} = k(1-s_0^2\rho^2)^{1/2}, \\ r &= \frac{ks_0}{2\pi}(x^2+y^2)^{1/2}, \end{aligned} \tag{2.40}$$

with the field strength function $\mathbf{E_s}$, originally defined as a function of the wave vector components (k_x, k_y), now to be measured as a function of the normalized radial aperture coordinate ρ on the exit pupil sphere and the azimuthal coordinate $\theta + \pi$. The position on the exit pupil sphere is obtained from Eq.(2.13) using $x = x_f - (k_x/k)R,\ y = y_f - (k_y/k)R$, leading to real space coordinates of $(x = -\rho a\cos\theta,\quad y = -\rho a\sin\theta)$, in normalized polar coordinates $(\rho, \theta + \pi)$; note that this latter phase off-set of π is missing in [Wolf (1959)].

2.6 Analytic expressions for the point-spread function in the focal region (scalar case)

The first analytic solution of the aberration-free point-spread function integral of Eq.(2.20) goes back to [Lommel (1885)] and is treated in detail in [Born, Wolf (2002)]. The solution for the aberrated case has been studied by various authors, see [Conrady (1919)], [Steward (1925)], [Picht (1925)], [Richter (1925)]. A more systematic analysis of the influence of aberrations on the point-spread function became possible after the introduction of the Zernike polynomials to describe the wavefront aberration, see [Zernike (1934)], [Ni-

jboer (1942)], [Zernike, Nijboer (1949)]. Considering the integral of Eq.(2.20) for a circular aperture (unit circle), we first substitute the Zernike expansion for the aberration function and use the approximation $\exp(i\Phi) \approx 1 + i\Phi$ for small values of Φ, typically $\Phi \leq 1$. We thus obtain

$$E_f(r,\phi,f) \approx \int_0^{2\pi}\int_0^1 \exp\left\{if\rho^2\right\} E(\rho,\theta)\{1 + i\sum_{nm}\alpha_n^m R_n^{|m|}(\rho)\exp(im\theta)\} \times \exp\left\{i2\pi r\rho\cos(\theta-\phi)\right\} \rho d\rho d\theta. \quad (2.41)$$

Carrying out the integration over θ and using the property

$$\int_0^{2\pi} \exp(im\theta)\exp\left\{i2\pi r\rho\cos(\theta-\phi)\right\} d\theta = 2\pi i^m J_m(2\pi r\rho)\exp(im\phi), \quad (2.42)$$

we get the expression originally derived by Nijboer in his thesis [Nijboer (1942)],

$$E_f(r,\phi,f) \approx 2\pi i \int_0^1 \exp\left\{if\rho^2\right\} E(\rho,\theta) \times \left\{[(1+\alpha_0^0)J_0(2\pi r\rho)] + \sum_{nm} i^{m+1}\alpha_n^m R_n^{|m|}(\rho)J_m(2\pi r\rho)\exp(im\phi)\right\}\rho d\rho, \quad (2.43)$$

where the summation now has to be carried out over all possible (n,m)-values with the exception of $m = n = 0$. As usual, the function $J_m(x)$ denotes the Bessel function of the first kind of order m. We remark here that, instead of expanding the function Φ itself using the α-coefficients, it is also possible to expand the complete pupil function $E(\rho,\theta)\exp\{i\Phi(\rho,\theta)\}$ in terms of Zernike polynomials, as it was first proposed in [Kintner, Sillitto (1976)].

A basic result from aberration theory, initially derived by Nijboer, is the following

$$\int_0^1 R_n^{|m|}(\rho)J_m(2\pi r\rho)\rho d\rho = (-1)^{\frac{n-|m|}{2}}\frac{J_{n+1}(2\pi r)}{2\pi r}. \quad (2.44)$$

In the perfectly focused case and for $E(\rho,\theta) \equiv 1$, the integral above is sufficient to analytically calculate the amplitude E_f with $z_n = 0$ in Eq.(2.43). However, in the defocused case, the analysis becomes more complicated and Bauer's formula has been used by Nijboer to obtain a workable expression [Nijboer

(1942)],

$$\exp(if\rho^2) = \exp(if/2) \sum_{n=0}^{\infty} (2n+1) i^n \; j_n\left(\frac{f}{2}\right) R_{2n}^0(\rho). \tag{2.45}$$

The spherical Bessel function $j_k(x)$ of the first kind is defined by

$$j_k(x) = \sqrt{\frac{\pi}{2x}}\, J_{k+\frac{1}{2}}(x) \;, \qquad k = 0, 1, \ldots \;, \tag{2.46}$$

see [Born, Wolf (2002)], Ch. 9, and [Abramowitz (1970)], Ch. 10. The extra radial Zernike polynomials that result from the expansion of the quadratic defocus exponential can be treated by formulae that express the product of two Zernike polynomials into a series of Zernike polynomials with differing upper or lower indices. This approach has been discussed by Nijboer. In practice, his solution allows to solve the problem of the defocused aberrated point-spread function for modest defocus values, for instance $|f| < \pi/2$. When trying to reconstruct aberrations from defocused intensity distributions, numerically reliable expressions for the intensity of the out-of-focus point-spread function are required over a larger range of f-values. The work described in Nijboer's thesis does not yet provide such results. It should be added that, even if these results would have been available, the lack of advanced computational means would have prohibited any further activity in this direction at that time.

2.6.1 Analytic solution for the general defocused case

A semi-analytic solution of the aberrated diffraction integral in the defocused case was presented in [Janssen (2002)] and its application and convergence domain was studied in [Braat, Dirksen, Janssen (2002)]. The basic integral occurring in, for instance, Eq.(2.43) reads

$$V_n^m(r, f) = \int_0^1 \exp\left\{if\rho^2\right\} R_n^{|m|}(\rho) J_m(2\pi r\rho) \rho d\rho \;, \tag{2.47}$$

and its solution is found to be an infinite Bessel function series according to

$$V_n^m(r, f) = \epsilon_m \exp\left[if\right] \sum_{l=1}^{\infty} (-2if)^{l-1} \sum_{j=0}^{p} v_{lj} \frac{J_{|m|+l+2j}(2\pi r)}{l(2\pi r)^l} \;. \tag{2.48}$$

In Eq.(2.48) we have to choose $\epsilon_m = -1$ for odd $m < 0$ and $\epsilon_m = 1$ otherwise. The function $V_n^m(r, f)$ provides us with the analytic solution of the integrals that occur in the general expression of E_f in Eq.(2.43) and they are associated with a typical Zernike aberration of radial order n and azimuthal order m. To obtain the total expression for E_f, it is just required to insert the appropriate azimuthal dependence. Denoting

$$p = \frac{n - |m|}{2}\,, \qquad\qquad q = \frac{n + |m|}{2}, \tag{2.49}$$

the coefficients v_{lj} in Eq.(2.48) are given as

$$v_{lj} = (-1)^p(|m| + l + 2j) \times \binom{|m| + j + l - 1}{l - 1}\binom{j + l - 1}{l - 1}\binom{l - 1}{p - j}\Big/\binom{q + l + j}{l}, \tag{2.50}$$

for $l = 1, 2, \ldots,\ \ j = 0, 1, \ldots, p$. The binomial coefficients are defined by

$$\binom{n}{m} = \frac{n(n-1)\cdots(n-m+1)}{m!} \tag{2.51}$$

with the remark that any binomial with $n < m$ is put equal to zero. To illustrate the accuracy of the series expansion, it can be shown that an absolute accuracy of 10^{-6} requires a number l_{max} of terms in the summation that is given by $l_{max} = |3f| + 5$. With this number of terms and a range $|f| \leq 2\pi$, the amplitude in the focal region of interest of well-corrected optical imaging systems can be calculated with ample precision.

Some special cases for the scalar amplitude E_f of Eq.(2.43) can be directly derived using the results of Eqs.(2.48)-(2.51).

- Nijboer's in-focus result of Eq.(2.44) is obtained for the special case of Eq.(2.48) with f=0, where the summation over l is now restricted to the term with $l = 1$ and the coefficient v_{1j} is identical $(-1)^{(n-|m|)/2}$, regardless the value of j.
- The special case with $m = n = 0$ corresponds to the aberration-free situation that should yield the result originally obtained by Lommel. Referring to Eq.(2.47), Lommel's solution reads, see [Born, Wolf (2002)],

$$V_0^0(r, f) = \int_0^1 \exp\left\{if\rho^2\right\} J_0(2\pi r\rho)\rho d\rho = \frac{C(r, 2f) + iS(r, 2f)}{2}\,, \tag{2.52}$$

with the functions C and S given by

$$C(r,f) = \frac{\cos(f/2)}{f/2}\, U_1(r,f) + \frac{\sin(f/2)}{f/2}\, U_2(r,f)\ ,$$
$$S(r,f) = \frac{\sin(f/2)}{f/2}\, U_1(r,f) - \frac{\cos(f/2)}{f/2}\, U_2(r,f), \tag{2.53}$$

with the general Lommel-function $U_n(r,f)$ defined by

$$U_n(r,f) = \sum_{s=0}^{\infty} (-i)^{2s} \left(\frac{f}{2\pi r}\right)^{2s+n} J_{2s+n}(2\pi r)\ . \tag{2.54}$$

The substitution of Lommel's results in Eq.(2.52) leads, after some rearrangement, to the expression

$$V_0^0(r,f) = \exp(if) \sum_{l=1}^{\infty} (-2if)^{l-1} \frac{J_l(2\pi r)}{(2\pi r)^l}. \tag{2.55}$$

It is seen that this compact expression of Lommel's result is equivalent to the special case with $n = m = 0$ of Eq.(2.48) once we have substituted the value $v_{l0} = l$.

- The on-axis amplitude distribution is obtained from Eq.(2.43) with $r = 0$. If we limit ourselves to circularly symmetric aberrations with $m = 0$ and use Bauer's formula of Eq.(2.45) for the defocus exponential, the integral over ρ is easily evaluated with the aid of the properties of the inner products of the radial Zernike polynomials and we find

$$E_f(0,0,f) \approx i\pi\ \exp(if/2) \left\{ j_0(f/2) + \sum_{n=0}^{\infty} i^n \alpha_{2n}^0 j_n(f/2) \right\}. \tag{2.56}$$

In the aberration-free case, the axial dependence is given by the spherical Bessel function of zero order. With the identity $j_0(x) = \sin(x)/x$, we find the Lommel result above.

Another analytic result from [Janssen (2002)] is related to diffraction integrals of the type

$$T_n^m(r,f) = \int_0^1 \exp\left\{if\rho^2\right\} \rho^n J_m(2\pi r\rho)\rho d\rho\ . \tag{2.57}$$

These integrals with a ρ-monomial in the integrand can be considered to be the building blocks for more general integrals containing a polynomial like a Zernike polynomial. Of course, they are also useful in the context of the

aberration representation according to Seidel. The Bessel series solution of this type of integral is given by

$$T_n^m(r,f) = \epsilon_m \exp[if] \sum_{l=1}^{\infty} (-2if)^{l-1} \sum_{j=0}^{p} s_{lj} \frac{J_{|m|+l+2j}(2\pi r)}{(2\pi r)^l} \; . \tag{2.58}$$

In Eq.(2.58) we again choose $\epsilon_m = -1$ for odd $m < 0$ and $\epsilon_m = 1$ otherwise. The coefficients s_{lj} are given by

$$s_{lj} = (-1)^j \, \frac{|m| + l + 2j}{q+1} \binom{p}{j} \binom{|m| + j + l - 1}{l-1} \Big/ \binom{q+l+j}{q+1}, \tag{2.59}$$

for the same ranges as in the case of v_{lj}: $l = 1, 2, \ldots,$ $j = 0, 1, \ldots, p$.

In the case of circularly symmetric aberrations a different expansion of the diffraction integral has been proposed in [Cao (2003)] and it produces analytic expressions for the functions $T_{2p}^0(r,f)$ defined above. The exponential factor $\exp(if\rho^2)$ is written as a Taylor series in f and this gives rise to the appearance of the so-called $Jinc$-functions with index n according to

$$Jinc_n(r) = \frac{1}{(2\pi r)^{2n+2}} \int_0^{2\pi r} x^{2n+1} \, J_0(x) \, dx, \tag{2.60}$$

for which Bessel series expansions are given. A convergence problem is present with respect to the power series expansion in f and the condition $|f| \leq 15$ should be respected to obtain an accuracy of 10^{-3} in amplitude, 10^{-6} in intensity.

The analytic expressions for the general functions $V_n^m(r,f)$ and $T_n^m(r,f)$ are composed of a Bessel function expansion with the argument $2\pi r$ and a power series expansion with respect to f. The latter series expansion, especially for the V-functions, gives rise to numerical convergence problems once the value of $|f|$ is larger than, say, 5π and an accuracy of 10^{-8} in amplitude can not be achieved for larger f-values. A drastic improvement in accuracy is obtained once the power series expansion in f can somehow be replaced by a more stable expression. To this goal, we use Bauer's expansion and write the exponential $\exp(if\rho^2)$ according to Eq.(2.45). Using this in the expression for $V_n^m(r,f)$, we find

$$V_n^m(r,f) = \exp(\frac{1}{2}if) \sum_{k=0}^{\infty} (2k+1) \, i^k \, j_k(f/2) \; \times$$

$$\int_0^1 R_{2k}^0(\rho)\, R_n^{|m|}(\rho)\, J_m(2\pi r\rho)\, \rho\, d\rho\ . \tag{2.61}$$

To proceed further, a general expression is needed that writes the product of a radially symmetric Zernike polynomial $R_{2k}^0(\rho)$ and a general polynomial $R_n^m(\rho)$ as a series of Zernike polynomials according to

$$R_{2k}^0\, R_{|m|+2p}^{|m|} = \sum_l w_{kl}\, R_{|m|+2l}^{|m|}\ . \tag{2.62}$$

In [Janssen, Braat, Dirksen (2004)], explicit expressions have been given for the coefficients w_{kl} and the range of the summation index l (see also Appendix C). A numerical implementation of these results has shown that $|f|$-values as large as 1000 can be dealt with. To illustrate the kind of intensity distributions that can be numerically handled by the analysis according to Eqs.(2.61)-(2.62), we show in Fig. 2.8 cross-sections of strongly defocused intensity distributions. In the left figure, a contour map is shown of an axial cross-section of a focal

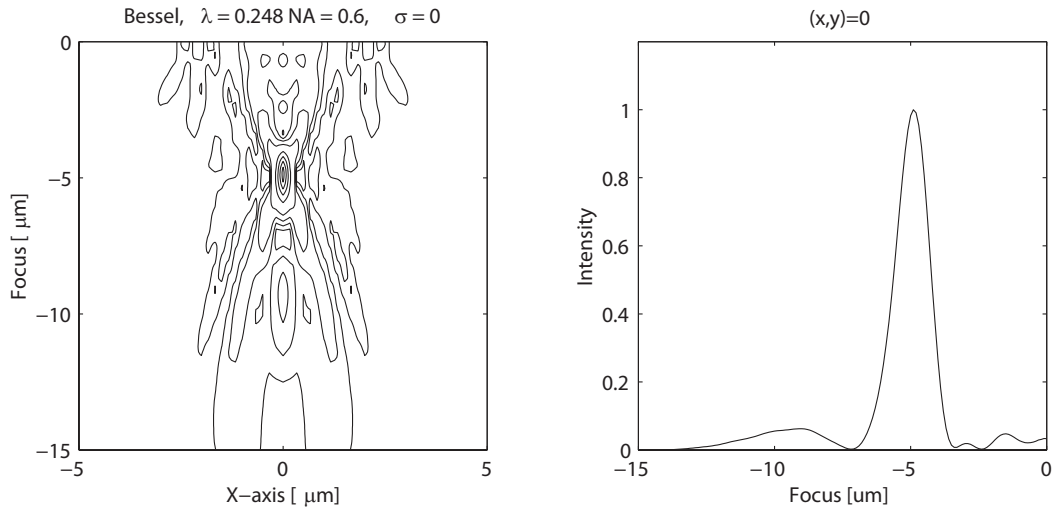

Fig. 2.8. Axial cross-section of a defocused intensity distribution (f=23) caused by the presence of a Fresnel zone plate in the plane z=0. The beam shows some circularly symmetric aberration that becomes visible in the figure on the right in which the axial intensity has been plotted. The numerical aperture is 0.60, the wavelength amounts to λ=248 nm.

intensity distribution that is off-set by approximately 15 focal depths from its nominal focal setting. The intensity distribution has been produced by means of a Fresnel zone lens and is affected by spherical aberration. In the right figure, we show the axial intensity distribution that shows an asymmetry around focus due to this residual aberration of the focusing beam. Figure 2.9 produces a picture of the measured intensity distribution in a strongly defocused image plane ($f \approx 75$). A typical Fresnel diffraction pattern is observed. Some spurious structure is visible due to light scattering at imperfections on the optical

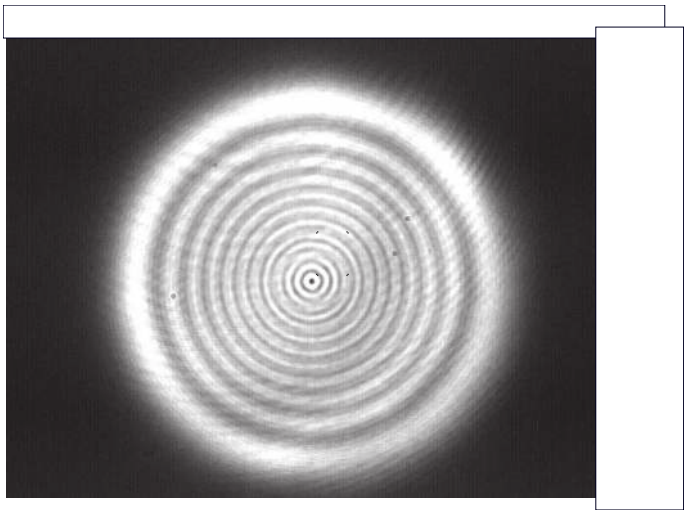

Fig. 2.9. Measured intensity distribution in a strongly defocused image plane. The value of f is approximately 75. Note that the axial intensity corresponds to a minimum due to the presence of an even number of Fresnel zones in the aperture as seen from the defocused position.

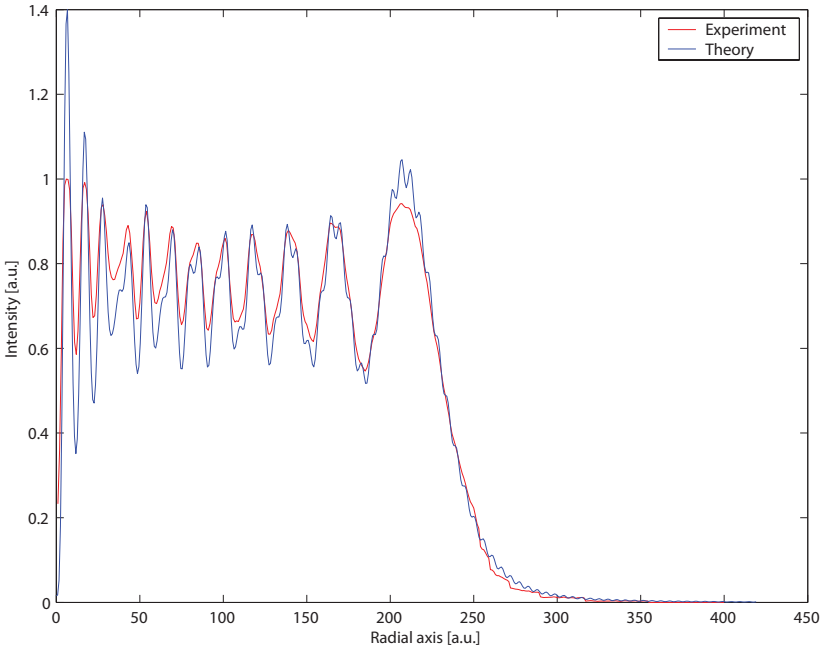

Fig. 2.10. Comparison of a measured intensity distribution and the best-fit calculated intensity distribution. In this case the value of f is 75 radians. The measured intensity shows a less pronounced modulation than the calculated distribution which may be attributed to some scattered background light and to a diaphragm rim that is not perfectly spherical.

surfaces in the experimental set-up. The number of luminous rings N_F in the Fresnel diffraction pattern is approximately given by $N_F = (f - \pi)/2\pi$.

In Fig. 2.10 we show a radial cross-section of such a defocused intensity distribution, from the central position on axis up to the geometrical shadow region. It is interesting to note that part of the fine structure in the fringes, predicted by the calculations, is also visible in the measured distribution, despite the high sensitivity of the measured intensity to spurious coherent light

scattered in the set-up. The calculated distribution was fit to the measured one by varying the f-parameter; the optimum value for these measured data was f=75.

When comparing the semi-analytic methods based on the out-of-focus extension of the Nijboer-Zernike diffraction theory and the numerical methods of the Fast Fourier Transform (FFT) type for solving the various diffraction integrals, we conclude the following. The analytic method has a clear advantage regarding the accuracy and monitored convergence of the solutions. In practice, the numerical effort is a linear function of the defocus parameter and machine-precision is the limiting factor when ultimate accuracy is sought for. Typical aliasing problems like in an FFT-calculation are of no concern. The aberration value can basically be increased to large values with respect to the wavelength of the light, although the number of Zernike aberration terms might become unwieldy. The calculation of the Zernike coefficients of the aberrated wavefront is a numerical investment that has to be carried out beforehand. Once the coefficients have been obtained, the actual calculation of the scalar amplitude or the field components in the focal region is extremely fast. The analytic decomposition in (r, f)- and ϕ-dependent functions produces an important economic advantage regarding computation time. At this moment we can state that the numerical effort to produce the amplitude in a single image plane using the analytic approach is comparable to the Fast Fourier Transform case. However, the equal numerical effort situation for both methods is limited to relatively coarse calculations. As soon as an accuracy better than, say, 10^{-4} is required, the FFT calculation time has to be strongly increased. The main reason for this is the intrinsic discontinuous nature of the pupil function which asks for high sample rates. For the calculation of the amplitude distribution in a large number of defocused planes, the semi-analytic method offers a very distinct advantage because the incremental numerical effort is small when going from one defocused plane to another, the only difference being the calculation of the $V(r, f)$-functions at another f-setting.

2.7 Analytic expressions for the point-spread function in the vector diffraction case

In the case of a non-uniform and aberrated amplitude distribution at the exit of the optical system, we have to further specify the expressions for the field components in Eqs.(2.36)-(2.37) by inserting a complex amplitude transmission function. Because of the vector nature of the diffraction problem, the transmission function possibly depends on the state of polarization. A general

field distribution that can be encountered in the entrance or exit pupil of an optical system is described in [Stallinga (2001)]. The general coherent field is written as the superposition of two orthogonal polarization states. We take the linear polarization states along, respectively, the x- and y-axis as basic orthogonal states. A general elliptical state of polarization is obtained via a linear superposition of the two basic linear states with relative amplitude weights and a certain phase difference, according to the complex numbers a_0 and b_0 defined in Subsection 2.5.3. The complex transmission functions for the two orthogonal linear polarizations in the entrance pupil are written

$$\begin{aligned} t_x(\rho,\theta) &= A_x(\rho,\theta)\exp\left[i\Phi_x(\rho,\theta)\right] , \\ t_y(\rho,\theta) &= A_y(\rho,\theta)\exp\left[i\Phi_y(\rho,\theta)\right] . \end{aligned} \tag{2.63}$$

Where A_x and A_y are real-valued functions and describe the transmission factors in the x- and y-direction, $\Phi_x(\rho,\theta)$ and $\Phi_y(\rho,\theta)$ are also real-valued and describe the phase distortion on the exit pupil sphere due to the wavefront aberration $W(\rho,\theta) = \Phi(\rho,\theta)/k$ introduced by the optical system. The phase difference $\epsilon(\rho,\theta) = \Phi_y(\rho,\theta) - \Phi_x(\rho,\theta)$ is the result, after traversal of the optical system, of a spatially varying birefringence due to medium transitions, optical coatings, internal material stresses etc. In well-corrected optical systems, the maximum value of the birefringence function $\epsilon(\rho,\theta)$ should be small and certainly restricted to the range $[-\pi,+\pi]$. Other orthogonal polarization states, for instance radial and azimuthal polarization distributions, see [Quabis, Dorn, Eberler, Glöckl, Leuchs (2000)], can also be accounted for by appropriately chosen functions $t_x(\rho,\theta)$ and $t_y(\rho,\theta)$.

The x- and y-dependent transmission functions of the optical system, given the incident linear state of polarization, are expanded with the aid of Zernike polynomials. We choose to apply a general expansion with complex Zernike coefficients β_x and β_y so that a complex transmission function can be represented, see [Kintner, Sillitto (1976)]. From now on, we will use the letter β for such an expansion to distinguish from an expansion of the phase aberration function Φ only with coefficients α according to Eq.(2.27). We thus have

$$\begin{aligned} t_x(\rho,\theta) &= \sum_{nm} \beta_{n,x}^m \; R_n^{|m|}(\rho) \; \exp\{im\theta\} , \\ t_y(\rho,\theta) &= \sum_{nm} \beta_{n,y}^m \; R_n^{|m|}(\rho) \; \exp\{im\theta\} . \end{aligned} \tag{2.64}$$

In the forward direction, the expansion is unique. In the reverse direction, obtaining the functions A and Φ from the β-coefficients, the uniqueness of such an

expansion can be questioned because of the contribution to both the real and imaginary part by the exponential factor in Eq.(2.63). But phase unwrapping techniques can be used, like in optical interferometry [Ettl, Creath (1996)], to recover the functions A and Φ independently if they show a smooth behaviour.

The transmission functions $t_{x,y}$ are now inserted in Eq.(2.39) and the following expressions are obtained for both the electric and magnetic field components in the focal region

$$\mathbf{E}(r,\phi,f) = \frac{-i\pi f_L s_0^2}{\lambda}\exp\left(\frac{if}{u_0}\right)\sum_{n,m} i^m \exp[im\phi]\times$$
$$\left[a_x\beta_{n,x}^m\begin{pmatrix} V_{n,0}^m + \frac{s_0^2}{2}\left(V_{n,2}^m\exp[2i\phi] + V_{n,-2}^m\exp[-2i\phi]\right) \\ -i\frac{s_0^2}{2}\left(V_{n,2}^m\exp[2i\phi] - V_{n,-2}^m\exp[-2i\phi]\right) \\ -is_0\left(V_{n,1}^m\exp[i\phi] - V_{n,-1}^m\exp[-i\phi]\right)\end{pmatrix} + \right.$$
$$\left. a_y\beta_{n,y}^m\begin{pmatrix} -i\frac{s_0^2}{2}\left(V_{n,2}^m\exp[2i\phi] - V_{n,-2}^m\exp[-2i\phi]\right) \\ V_{n,0}^m - \frac{s_0^2}{2}\left(V_{n,2}^m\exp[2i\phi] + V_{n,-2}^m\exp[-2i\phi]\right) \\ -s_0\left(V_{n,1}^m\exp[i\phi] + V_{n,-1}^m\exp[-i\phi]\right)\end{pmatrix}\right], \tag{2.65}$$

and,

$$\mathbf{B}(r,\phi,f) = \frac{-i\pi n_r f_L s_0^2}{c\lambda}\exp\left(\frac{if}{u_0}\right)\sum_{n,m} i^m \exp[im\phi]\times$$
$$\left[a_x\beta_{n,x}^m\begin{pmatrix} -i\frac{s_0^2}{2}\left(V_{n,2}^m\exp[2i\phi] - V_{n,-2}^m\exp[-2i\phi]\right) \\ V_{n,0}^m - \frac{s_0^2}{2}\left(V_{n,2}^m\exp[2i\phi] + V_{n,-2}^m\exp[-2i\phi]\right) \\ -s_0\left(V_{n,1}^m\exp[i\phi] + V_{n,-1}^m\exp[-i\phi]\right)\end{pmatrix} + \right.$$
$$\left. a_y\beta_{n,y}^m\begin{pmatrix} -V_{n,0}^m - \frac{s_0^2}{2}\left(V_{n,2}^m\exp[2i\phi] + V_{n,-2}^m\exp[-2i\phi]\right) \\ +i\frac{s_0^2}{2}\left(V_{n,2}^m\exp[2i\phi] - V_{n,-2}^m\exp[-2i\phi]\right) \\ is_0\left(V_{n,1}^m\exp[i\phi] - V_{n,-1}^m\exp[-i\phi]\right)\end{pmatrix}\right], \tag{2.66}$$

with f_L the image side focal distance and a_x and a_y the complex amplitude factors that determine the total power in the incident beam and allow to specify the state of global polarization of the light incident on the entrance pupil. The quantity n_r is the refractive index of the image space medium. The

newly defined functions $V_{n,j}^m$ that depend on the normalized radial coordinate r and the defocus parameter f are given by ($j = -2, -1, 0, 1, 2$)

$$V_{n,j}^m(r,f) = \int_0^1 \rho^{|j|} \frac{\left(1+\sqrt{1-s_0^2\rho^2}\right)^{-|j|+1}}{(1-s_0^2\rho^2)^{1/4}} \exp\left[\frac{if}{u_0}\left(1-\sqrt{1-s_0^2\rho^2}\right)\right] \times R_n^{|m|}(\rho) J_{m+j}(2\pi r\rho)\rho d\rho \quad . \tag{2.67}$$

In the expression for $V_{n,j}^m(r,f)$ we have incorporated the so-called radiometric effect in imaging the entrance pupil distribution onto the exit pupil sphere which leads to the factor $(1-s_0^2\rho^2)^{-1/4}$ in the integrand; it was discussed in Subsection 2.5.1 and follows from Abbe's sine condition for the imaging of the pupils, see Eq.(2.24). A series expansion can be devised to quickly obtain accurate values of the integral above. The functions that can be used in the expansions and the values of the corresponding expansion coefficients are given in Appendix D.

To illustrate the results above, we produce in Figs. 2.11-2.13 some grey-

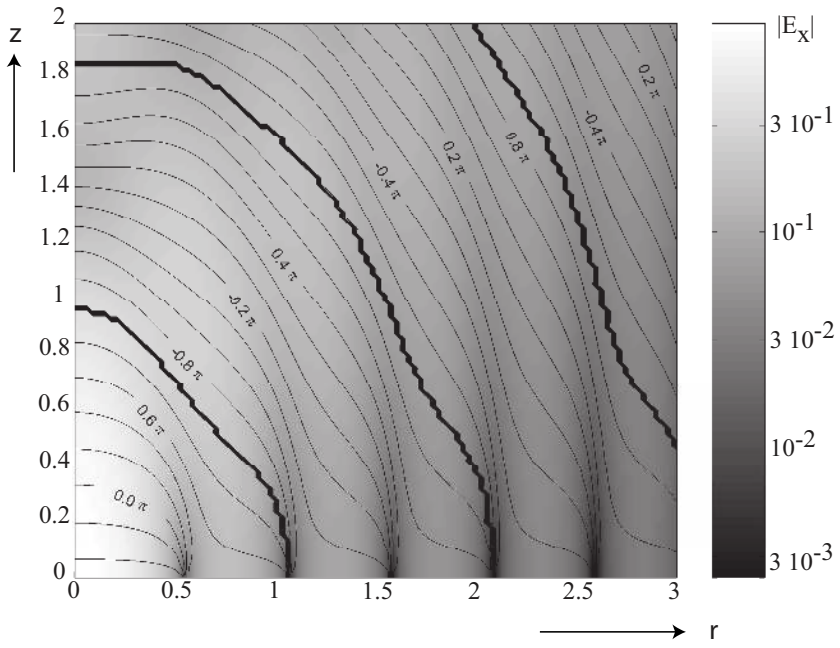

Fig. 2.11. Graph of the absolute values of the E_x-field component, and its phase in the focal volume for a high-numerical-aperture focused beam (s_0=0.95, linearly polarized incident light along the x-axis). Both the radial coordinate r and the axial coordinate z have been expressed in units of λ/s_0. Phase singularities are observed at the locations of zero amplitude.

scale graphs obtained with our high accuracy analytic formulae and that were published in [Braat, Dirksen, Janssen, van de Nes (2003)]. The series expansions for the vector components of the electric field have been truncated such that the inaccuracy in the field components is below an absolute value of 10^{-6},

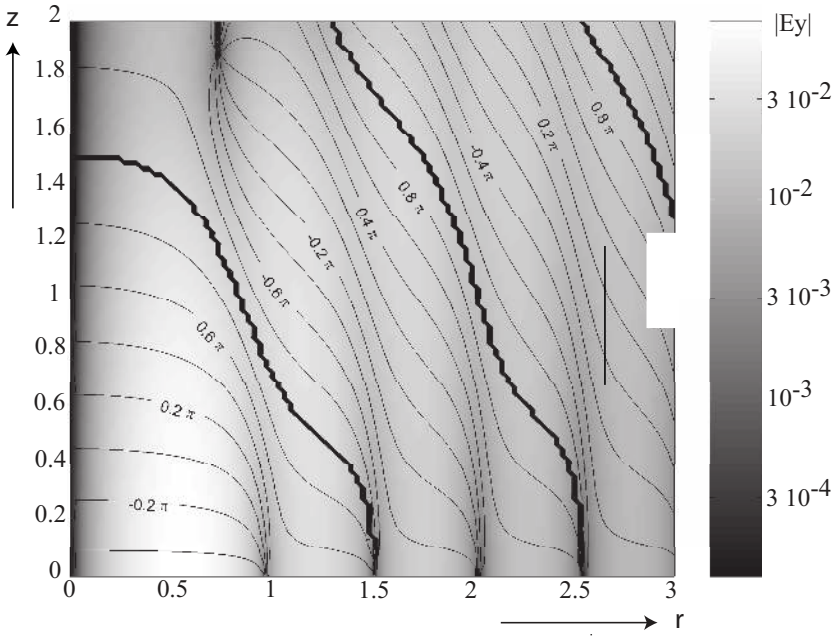

Fig. 2.12. Same legend as Fig. 2.11, now for the y-component of the electric field.

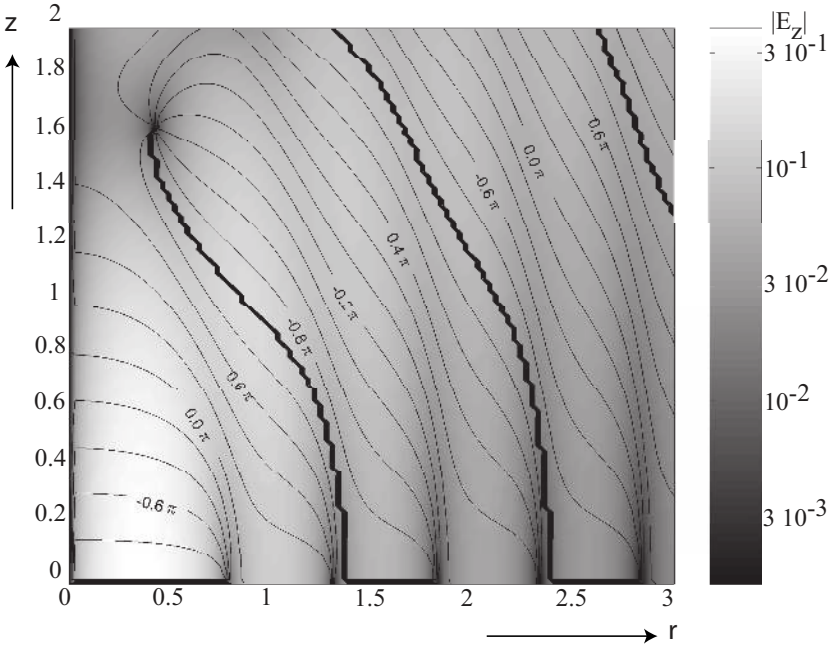

Fig. 2.13. Same legend as Fig. 2.11, now for the z-component of the electric field.

the corresponding inaccuracy in intensity below 10^{-12}. Finally, in Fig. 2.14 we have produced cross-sections of the energy density in the optimum focal plane ($z = f = 0$). The 'Airy disc' approximation (fully drawn curve) at high-NA has been obtained from the analytical expression $4J^2(2\pi r)/(2\pi r)^2$; its theoretical minima have been plotted explicitly. The dashed and dotted curves have been sampled using our semi-analytic series expansions for the field components in the focal plane. Due to this discrete sampling, the zero values that are theoretically possible in the cross-section perpendicular to the incident polarization

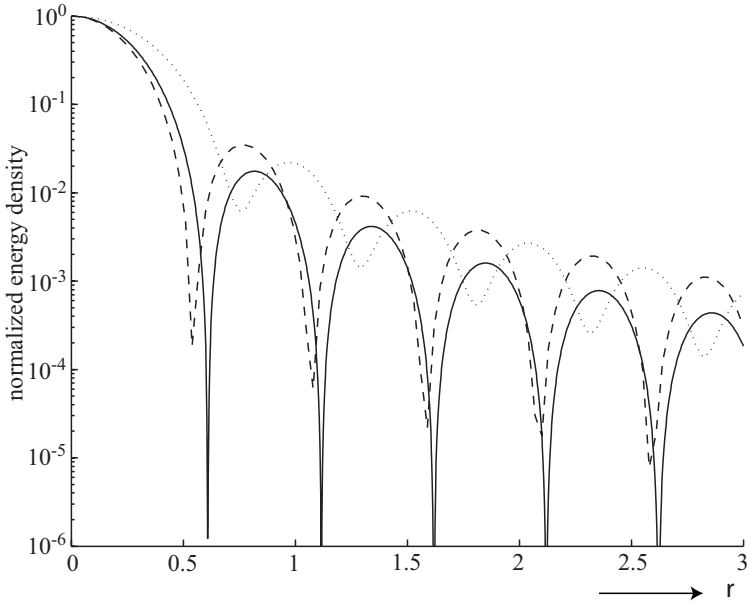

Fig. 2.14. Cross-sections of the normalized energy density ($\propto |\mathbf{E}|^2$) in the optimum focal plane of a high-numerical-aperture focused beam (s_0=0.95, linearly polarized incident light) as a function of the radial normalized coordinate r in units of λ/s_0. Drawn line: hypothetic Airy disc profile, extrapolated to this high-NA value from the low-aperture scalar model. Dashed line: cross-section of the normalized energy density, in a plane perpendicular to the incident linear polarization (y-cross-section). Dotted line: idem, now in the plane of the incident linear polarization parallel to the x-axis.

have not been exactly represented (dashed curve). Figure 2.14 clearly shows that in the cross-section parallel to the incident polarization no explicit zeros are observed. The different full widths at half maximum (FWHM) in the two main cross-sections, already demonstrated in [Richards, Wolf (1959)], are also clearly observed. The narrower FWHM for the cross-section perpendicular to the plane of polarization of the incident light can be explained by the relative amplitude enhancement as a function of the normalized exit pupil coordinate ρ at the pupil rim. This phenomenon is proper to an optical system satisfying Abbe's sine condition. Its behavior resembles that of a system with an annular aperture yielding a smaller value of the FWHM of the intensity profile and showing increased side lobe intensity.

2.8 The point-spread function in a stratified medium

So far, we have supposed that the image space was homogeneous. In practice, when using point-spread functions for the assessment of the quality of an optical system, the detection of the free-space focused beam is carried out in a relatively thin detection medium, for instance photo-resist on a Si-substrate or a photosensitive thin slice of doped crystalline silicon. The final transition

to the detecting medium, within the focal volume, induces angle-dependent amplitude and phase changes that produce a difference between the free-space intensity distribution and the effectively detected distribution in the medium. The effect of a single transition has been studied by [Ling, Lee (1984)] in the framework of focused microwaves and by [Török, Varga, Laczik, Booker (1995)] for optical microscopy when a mismatched aberrating cover glass is used. A general analysis of high-numerical-aperture imaging is described in [Mansuripur (1986)]-[Mansuripur (1989)]. The basic mathematical tool in the analysis of these references is Fourier transformation, to propagate through free space, but equally well through optical components of various nature (gratings, birefringent plates, thin-film stacks), both for point-source imaging and for the imaging of extended objects. Through its very general nature and flexibility, this approach is less convenient for numerical treatment of a specific problem like the formation of a point-spread function, issued from a single tiny source point.

The specific problem of detecting a point-spread function in a thin recording layer at very high numerical aperture is discussed in [Flagello, Milster (1992)], [Flagello, Milster, Rosenbluth (1996)]. The analysis applies the matrix technique devised for reflection and transmission of light through thin films, see [Macleod (1989)]. The plane wave components in the Debye integral expressions that are incident at a certain angle on the detection layer are given by the typical complex Fresnel coefficients belonging to the multiple reflection and transmission phenomena in the thin film stack at that specific angle. A modified version of the approach by Flagello et al. can be found in [van de Nes, Billy, Pereira, Braat (2004)]. Here, the analysis has been simplified by using polar coordinates throughout, thus exploiting the special behavior of the electric field components in the plane of incidence and perpendicular to it, the *p*- and *s*-components, respectively. For point-spread functions in a narrow field close to the optical axis, this approach is permitted; it is not applicable when skew beams and strongly off-axis point-spread functions have to be studied. The superposition of the forward and backward propagating plane waves in the layered medium with their angle-dependent amplitude and phase can be taken into account in modified Zernike expansions of the pupil function. One modified expansion applies to the forward propagating waves, the other to the backward propagating waves, creating a second 'virtual' exit pupil function. With these modified pupil functions, two point-spread functions pertaining to the two propagation directions can be calculated in the corresponding layer of the stratified medium. The coherent superposition of the field components of the two point-spread functions allows the calculation of the local electric

energy density that shows the typical standing wave phenomena in such a thin-film stack. The first noticeable effect of the penetration of the focused beam in the recording layer is a circularly symmetric phase defect to be classified as spherical aberration, see [Visser, Wiersma (1991)]. At high numerical aperture, amplitude and phase deviations without circular symmetry become visible in the case of, for instance, linearly polarized light in the entrance pupil. Projected back to the exit pupil of the imaging system, this is equivalent to the introduction of apparent astigmatism in the focusing beam. The further treatment of point-spread function formation in layered media is outside the scope of this chapter.

3 Energy density and power flow in the focal region

In the preceding section we have derived expressions for the complex disturbance (scalar approximation) or the complex field vectors (high-numerical-aperture vector case) in the focal region. These basic quantities are needed for evaluating the optically measurable quantities like energy density, intensity, linear impulse and angular momentum that are built up in and transported through the focal region. Although these quantities, time-averaged at optical frequencies, can be obtained in each point from the electromagnetic field vectors only, we will carry out, in this subsection, a detailed analysis of the typical distributions in energy density and intensity that are associated with particular aberrations. We need these expressions when we address the main subject of this chapter, the assessment of optical systems using the point-spread function intensity in the focal region. As the starting point, we will use the expressions for the field vectors that were derived in Eqs.(2.65)-(2.66). Not only wavefront aberration is incorporated in the model but also a non-uniform amplitude distribution on the exit pupil sphere, as this is, in any case, to be expected for high-numerical-aperture imaging. In this section we will express the quadratic quantities in the focal region (energy density, Poynting vector components) in terms of the basic diffraction integral $V_{n,j}^m(r, f)$. Regarding the energy density, we will restrict ourselves to the electric energy density because this is the quantity that is relevant for detectors or recording media at optical frequencies. The energy flow, described by e.g. the cartesian or cylindrical components of the Poynting vector, will be discussed relatively briefly. The direction and magnitude of the vector yield the flow of the total electromagnetic energy, including the magnetic part. The divergence of the Poynting vector yields the energy outflow per unit volume. If the power loss in the detection medium is due to its finite conductance only, the loss can be attributed to ohmic dissipation and is proportional to the electric energy density in the medium. In this case, the electric energy density can directly be used; the Poynting vector data can serve as a check on the calculations based on the electric energy density. Finally, the electric energy density distribution in the focal region according to the scalar approximation will come out as the low-aperture limit of the result for an arbitrary opening angle of the focused beam.

The time averaged value of the electric field energy density $\langle w_e \rangle$ is given by

$$\langle w_e \rangle = \frac{\epsilon_0}{2} n_r^2 |\mathbf{E}|^2 \ , \tag{3.1}$$

with the relative dielectric constant given by $\epsilon = n_r^2$. The electric field components in the presence of aberrations in a high-numerical-aperture system, as given by Eq.(2.65), are needed to compute the scalar product $\mathbf{E}^* \cdot \mathbf{E}$. The direct evaluation of $\langle w_e \rangle$ leads to a quadruple sum over the indices n, m, $n^{'}$ and $m^{'}$ that appear in the products of the electric field components. In our approach to quality assessment of optical systems, we focus on the typical azimuthal dependencies that appear in the through-focus intensity distribution in the presence of aberrations. For that reason, a more systematic approach is required in the evaluation of the energy density expression. We combine terms with equal azimuthal dependence $\exp(im\phi)$ and these collected terms will play an important role in the quality assessment problem that we address in the second part of this chapter.

A general term in the expression of Eq.(3.1) is written

$$\begin{aligned} G_{kl}(\beta_1, \beta_2) = & \sum_{n,m} i^m \exp\left[im\phi\right] \ \beta_{n,1}^m V_{n,k}^m(r,f) \exp\left[ik\phi\right] \times \\ & \sum_{n',m'} i^{-m'} \exp\left[-im'\phi\right] \beta_{n',2}^{m'*} V_{n',l}^{m'*}(r,f) \exp\left[-il\phi\right] \\ = & \sum_{n,m,n',m'} \exp\left[i(m-m')\pi/2\right] \ \exp\left[i(m-m'+k-l)\phi\right] \times \\ & \beta_{n,1}^m \beta_{n',2}^{m'*} V_{n,k}^m(r,f) V_{n',l}^{m'*}(r,f) \ , \end{aligned} \tag{3.2}$$

where the function G_{kl} has the sets of Zernike coefficients $\beta_{n,1}^m$ and $\beta_{n,2}^m$ as variables, in shorthand notation written as β_1 and β_2 in the argument of G_{kl}). The indices $\{kl\}$ stem from the various combinations of $V_{n,j}^m \exp[i(j\phi)]$-functions that occur in the summation. The azimuthal dependence of the energy density terms is made explicit by writing the general quadruple series $\sum_{n,m,n',m'} a_{n,m,n',m'}$ according to a diagonal summation scheme as

$$\sum_{m,m',n,n'} a_{m,m';n,n'} = \sum_n \Big\{ \sum_m a_{m,m;n,n} +$$

$$\left. + \sum_{\mu=1}^{\mu_{max}} \sum_{m} \left(a_{m,m+\mu;n,n} + a_{m+\mu,m;n,n} \right) \right\}$$
$$+ \sum_{\nu=1}^{\nu_{max}} \left\{ \sum_{n} \sum_{m} \left(a_{m,m;n,n+\nu} + a_{m,m;n+\nu,n} \right) \right.$$
$$+ \sum_{\mu=1}^{\mu_{max}} \sum_{n} \sum_{m} \Big[a_{m,m+\mu;n,n+\nu} + a_{m+\mu,m;n,n+\nu}$$
$$\left. + a_{m,m+\mu;n+\nu,n} + a_{m+\mu,m;n+\nu,n} \Big] \right\}. \qquad (3.3)$$

The summation ranges for the indices m, n, μ_{max} and ν_{max} are derived from the transformation from a rectangular summation scheme to a summation scheme along the central diagonal and the off-axis diagonals. The following expression for G_{kl} results

$$\begin{aligned}
G_{kl}(\beta_1, \beta_2) = \exp\left[i(k-l)\phi\right] \Bigg[& \sum_{n} \sum_{m} \beta_{n,1}^{m} \beta_{n,2}^{m*} V_{n,k}^{m} V_{n,l}^{m*} + \\
& \sum_{\mu=1}^{\mu_{max}} \Bigg\{ \exp\left[-i\mu\pi/2\right] \exp\left[-i\mu\phi\right] \sum_{m} \sum_{n} \beta_{n,1}^{m} \beta_{n,2}^{m+\mu*} V_{n,k}^{m} V_{n,l}^{m+\mu*} \\
& \quad + \exp\left[i\mu\pi/2\right] \exp\left[i\mu\phi\right] \sum_{m} \sum_{n} \beta_{n,1}^{m+\mu} \beta_{n,2}^{m*} V_{n,k}^{m+\mu} V_{n,l}^{m*} \Bigg\} \\
& + \sum_{\nu=1}^{\nu_{max}} \Bigg\{ \sum_{n} \sum_{m} \left(\beta_{n,1}^{m} \beta_{n+\nu,2}^{m*} V_{n,k}^{m} V_{n+\nu,l}^{m*} + \beta_{n+\nu,1}^{m} \beta_{n,2}^{m*} V_{n+\nu,k}^{m} V_{n,l}^{m*} \right) \\
& \quad + \sum_{\mu=1}^{\mu_{max}} \Bigg[\exp\left[-i\mu\pi/2\right] \exp\left[-i\mu\phi\right] \Bigg\{ \sum_{n} \sum_{m} \Big(\beta_{n,1}^{m} \beta_{n+\nu,2}^{m+\mu*} V_{n,k}^{m} V_{n+\nu,l}^{m+\mu*} \\
& \qquad + \beta_{n+\nu,1}^{m} \beta_{n,2}^{m+\mu*} V_{n+\nu,k}^{m} V_{n,l}^{m+\mu*} \Big) \Bigg\} \\
& \qquad + \exp\left[i\mu\pi/2\right] \exp\left[+i\mu\phi\right] \Bigg\{ \sum_{n} \sum_{m} \Big(\beta_{n,1}^{m+\mu} \beta_{n+\nu,2}^{m*} V_{n,k}^{m+\mu} V_{n+\nu,l}^{m*} \\
& \qquad + \beta_{n+\nu,1}^{m+\mu} \beta_{n,2}^{m*} V_{n+\nu,k}^{m+\mu} V_{n,l}^{m*} \Big) \Bigg\} \Bigg] \Bigg\} \Bigg], \qquad (3.4)
\end{aligned}$$

where we have suppressed in the notation the (r, f)-dependence of the V-functions. With the G-function notation above, the electric energy density is readily written as

$$\begin{aligned}
\langle w_e(r, \phi, f) \rangle = \frac{\epsilon_0 n_r^2 k_0^2 f_L^2 s_0^4}{8} \Big[& |a_x|^2 G_{0,0}(\beta_x, \beta_x) + \\
& s_0^2 \Re \left\{ G_{0,2}(a_x \beta_x, a_x \beta_x - i a_y \beta_y) \right. \\
& \qquad \left. + G_{0,-2}(a_x \beta_x, a_x \beta_x + i a_y \beta_y) \right\} +
\end{aligned}$$

$$
\begin{aligned}
&\frac{s_0^4}{4}\{G_{2,2}(a_x\beta_x - ia_y\beta_y, a_x\beta_x - ia_y\beta_y)+\\
&\quad +G_{-2,-2}(a_x\beta_x + ia_y\beta_y, a_x\beta_x + ia_y\beta_y)\} +\\
&\frac{s_0^4}{2}\Re\{G_{2,-2}(a_x\beta_x - ia_y\beta_y, a_x\beta_x + ia_y\beta_y)\} +\\
&|a_y|^2 G_{0,0}(\beta_y, \beta_y) +\\
&-s_0^2\Re\{G_{0,2}(a_y\beta_y, ia_x\beta_x + a_y\beta_y)\\
&\qquad\qquad +G_{0,-2}(a_y\beta_y, -ia_x\beta_x + a_y\beta_y)\} +\\
&\frac{s_0^4}{4}\{G_{2,2}(ia_x\beta_x + a_y\beta_y, ia_x\beta_x + a_y\beta_y)+\\
&\quad G_{-2,-2}(-ia_x\beta_x + a_y\beta_y, -ia_x\beta_x + a_y\beta_y)\} +\\
&\frac{s_0^4}{2}\Re\{G_{2,-2}(ia_x\beta_x + a_y\beta_y, -ia_x\beta_x + a_y\beta_y)\} +\\
&s_0^2\{G_{1,1}(ia_x\beta_x + a_y\beta_y, ia_x\beta_x + a_y\beta_y)\\
&\quad +G_{-1,-1}(-ia_x\beta_x + a_y\beta_y, -ia_x\beta_x + a_y\beta_y)\} +\\
&2s_0^2\Re\{G_{1,-1}(ia_x\beta_x + a_y\beta_y, -ia_x\beta_x + a_y\beta_y)\}\Big],
\end{aligned}
\tag{3.5}
$$

with k_0 the vacuum wave number and f_L the focal length of the imaging system. The amplitude factors $a_{x,y}$ apply to the strength of the incident x- and y-polarization components and the indices x, y of β in the arguments of the G_{kl}-functions refer to the sets of Zernike coefficients to be used. They correspond to either x- or y- linearly polarized light and are denoted by $\beta_{n,x}^m$ and $\beta_{n,y}^m$, respectively.

A further rearrangement of the expression for $\langle w_e(r,\phi,f)\rangle$ is possible by using the properties

$$
\begin{aligned}
G_{kl}(\beta_1 + \beta_2, \beta_3 + \beta_4) = &\, G_{kl}(\beta_1, \beta_3)\\
&+G_{kl}(\beta_1, \beta_4) + G_{kl}(\beta_2, \beta_3) + G_{kl}(\beta_2, \beta_4),
\end{aligned}
\tag{3.6}
$$

$$
G_{kl}(\beta_1, \beta_2) = G_{lk}^*(\beta_2, \beta_1),
\tag{3.7}
$$

leading to the expression

$$
\begin{aligned}
\langle w_e(r,\phi,f)\rangle = &\frac{\epsilon_0 n_r^2 k_0^2 f_L^2 s_0^4}{8} \times\\
&\Big[|a_x|^2 G_{0,0}(\beta_x, \beta_x) + |a_y|^2 G_{0,0}(\beta_y, \beta_y) +\\
&\quad s_0^2\Re\left\{|a_x|^2 G_{0,2}(\beta_x, \beta_x) + ia_x a_y^* G_{0,2}(\beta_x, \beta_y)\right.
\end{aligned}
$$

$$
\begin{aligned}
&\quad +ia_x^* a_y G_{0,2}(\beta_y,\beta_x) - |a_y|^2 G_{0,2}(\beta_y,\beta_y)\big\} + \\
&s_0^2 \Re\big\{|a_x|^2 G_{0,-2}(\beta_x,\beta_x) - ia_x a_y^* G_{0,-2}(\beta_x,\beta_y) \\
&\quad -ia_x^* a_y G_{0,-2}(\beta_y,\beta_x) - |a_y|^2 G_{0,-2}(\beta_y,\beta_y)\big\} + \\
&\frac{s_0^4}{2}\big\{|a_x|^2 G_{2,2}(\beta_x,\beta_x) + ia_x a_y^* G_{2,2}(\beta_x,\beta_y) \\
&\quad -ia_x^* a_y G_{2,2}(\beta_y,\beta_x) + |a_y|^2 G_{2,2}(\beta_y,\beta_y)\big\} + \\
&\frac{s_0^4}{2}\big\{|a_x|^2 G_{-2,-2}(\beta_x,\beta_x) - ia_x a_y^* G_{-2,-2}(\beta_x,\beta_y) \\
&\quad +ia_x^* a_y G_{-2,-2}(\beta_y,\beta_x) + |a_y|^2 G_{-2,-2}(\beta_y,\beta_y)\big\} + \\
&s_0^2\big\{|a_x|^2 G_{1,1}(\beta_x,\beta_x) + ia_x a_y^* G_{1,1}(\beta_x,\beta_y) \\
&\quad -ia_x^* a_y G_{1,1}(\beta_y,\beta_x) + |a_y|^2 G_{1,1}(\beta_y,\beta_y)\big\} + \\
&s_0^2\big\{|a_x|^2 G_{-1,-1}(\beta_x,\beta_x) - ia_x a_y^* G_{-1,-1}(\beta_x,\beta_y) \\
&\quad +ia_x^* a_y G_{-1,-1}(\beta_y,\beta_x) + |a_y|^2 G_{-1,-1}(\beta_y,\beta_y)\big\} + \\
&+2s_0^2 \Re\big\{-|a_x|^2 G_{1,-1}(\beta_x,\beta_x) + ia_x a_y^* G_{1,-1}(\beta_x,\beta_y) \\
&\quad +ia_x^* a_y G_{1,-1}(\beta_y,\beta_x) + |a_y|^2 G_{1,-1}(\beta_y,\beta_y)\big\}\Big]. \qquad (3.8)
\end{aligned}
$$

The expression above is, within the framework of the approximations related to the Debye integral, a rigorous expression for the energy density in the focal region for a general incident state of polarization with the optical system suffering from transmission defects, wavefront aberration and spatially varying birefringence over the pupil cross-section. Once we eliminate all optical defects ($\beta_x = \beta_y = \beta$ with $\beta_0^0 = 1$ and all other $\beta_n^m \equiv 0$) and limit ourselves to linear polarization along the x-axis ($a_y = 0$), the expression is greatly simplified to

$$
\begin{aligned}
\langle w_e(r,\phi,f)\rangle = &\frac{\epsilon_0 n_r^2 k_0^2 f_L^2 s_0^4\,|a_x|^2}{8} \times \\
&\Big[\; G_{0,0}(\beta,\beta) + \\
&\quad s_0^2 \Re\left\{G_{0,2}(\beta,\beta) + G_{0,-2}(\beta,\beta) - 2G_{1,-1}(\beta,\beta)\right\} \\
&\quad \frac{s_0^4}{2}\left\{G_{2,2}(\beta,\beta) + G_{-2-2}(\beta,\beta)\right\}\Big], \qquad (3.9)
\end{aligned}
$$

and, on substituting the expression for the functions G_{kl} in the case of a perfect system, we find

$$
\langle w_e(r,\phi,f)\rangle = \frac{\epsilon_0 n_r^2 k_0^2 f_L^2 s_0^4\,|a_x|^2}{8} \times
$$

$$\Big[\ |V^0_{0,0}|^2 + 2s_0^2\left\{|V^0_{0,1}|^2 + \cos 2\phi\left[|V^0_{0,1}|^2 + \Re(V^0_{0,0}V^{0*}_{0,2})\right]\right\} + s_0^4|V^0_{0,2}|^2\Big]. \tag{3.10}$$

This special case corresponds to the original result on high-numerical aperture focusing by a perfect system treated in [Richards, Wolf (1959)]. When we strongly reduce the numerical aperture, only the leading term with s_0^4 remains, leading to Lommel's result. Finally, in the nominal focal plane ($f = 0$) and, using the analytic expression for $V^0_{0,0}$ with $s_0 \to 0$, we obtain the expression corresponding to Airy's result

$$\langle w_e(r,\phi,f)\rangle = \frac{\epsilon_0 n_r^2 |a_x|^2}{2}\ \left[\frac{\pi^2 f_L^2 s_0^4}{\lambda^2}\right]\ \left(\frac{2J_1(2\pi r)}{2\pi r}\right)^2\ , \tag{3.11}$$

where the factor between square brackets can be identified as the energy 'concentration' factor in optimum focus.

If we limit ourselves to optical systems that are free of birefringence, we can study characteristic energy density patterns in the focal region corresponding to special cases of incident polarization. A general state of polarization in the entrance pupil of the system is determined by the field coefficients $a_x = p_x A$ and $a_y = p_y A$, with p_x and p_y complex numbers satisfying $|p_x|^2 + |p_y|^2 = 1$ for the purpose of normalization. The absence of birefringence allows us to write for each aberration coefficient $\beta^m_{n,x} = \beta^m_{n,y} = \beta^m_n$. Using the result of Eq.(3.8), we find

$$\begin{aligned}
\langle w_e(r,\phi,f)\rangle = &\frac{\epsilon_0 n_r^2 k_0^2 f_L^2 s_0^4 |A|^2}{8}\ \times \\
&\Big[G_{0,0}(\beta,\beta) + \\
&s_0^2\left\{\left[|p_x|^2 - |p_y|^2\right]\Re\{G_{0,2}(\beta,\beta)\} - 2\Re(p_x p_y^*)\Im\{G_{0,2}(\beta,\beta)\}\right\} + \\
&s_0^2\left\{\left[|p_x|^2 - |p_y|^2\right]\Re\{G_{0,-2}(\beta,\beta)\} + 2\Re(p_x p_y^*)\Im\{G_{0,-2}(\beta,\beta)\}\right\} + \\
&\frac{s_0^4}{2}\left[\left\{1 - 2\Im(p_x p_y^*)\right\}G_{2,2}(\beta,\beta) + \left\{1 + 2\Im(p_x p_y^*)\right\}G_{-2,-2}(\beta,\beta)\right] + \\
&s_0^2\left[\left\{1 - 2\Im(p_x p_y^*)\right\}G_{1,1}(\beta,\beta) + \left\{1 + 2\Im(p_x p_y^*)\right\}G_{-1,-1}(\beta,\beta)\right] + \\
&-2s_0^2\left\{\left[|p_x|^2 - |p_y|^2\right]\Re\left\{G_{+1,-1}(\beta,\beta)\right\} + \right. \\
&\qquad\left. 2\Re(p_x p_y^*)\Im\left\{G_{+1,-1}(\beta,\beta)\right\}\right\}\Big].
\end{aligned} \tag{3.12}$$

Alternatively, the various terms in the expression above can be arranged according to their contribution to the four Stokes vector components like it was shown in [Stallinga (2001)]. Some special cases can be distinguished regarding the incident state of polarization.

3.1.1 Linear polarization

- x-direction, $(p_x, p_y) = (1, 0)$

The energy density reduces to

$$\begin{aligned}\langle w_e^x(r,\phi,f)\rangle_0 \propto & G_{0,0}(\beta,\beta) + s_0^2 \Re\left[G_{0,2}(\beta,\beta) + G_{0,-2}(\beta,\beta)\right] \\ & + \frac{s_0^4}{2}\left[G_{2,2}(\beta,\beta) + G_{-2,-2}(\beta,\beta)\right] \\ & + s_0^2\left[G_{1,1}(\beta,\beta) + G_{-1,-1}(\beta,\beta)\right] \\ & - 2s_0^2 \Re\left\{G_{+1,-1}(\beta,\beta)\right\} \quad . \end{aligned} \tag{3.13}$$

- y-direction, $(p_x, p_y) = (0, 1)$

The energy density is now proportional to

$$\begin{aligned}\langle w_e^y(r,\phi,f)\rangle_0 \propto & G_{0,0}(\beta,\beta) - s_0^2 \Re\left[G_{0,2}(\beta,\beta) + G_{0,-2}(\beta,\beta)\right] \\ & + \frac{s_0^4}{2}\left[G_{2,2}(\beta,\beta) + G_{-2,-2}(\beta,\beta)\right] \\ & + s_0^2\left[G_{1,1}(\beta,\beta) + G_{-1,-1}(\beta,\beta)\right] \\ & + 2s_0^2 \Re\left\{G_{+1,-1}(\beta,\beta)\right\} \quad . \end{aligned} \tag{3.14}$$

In Fig. 3.1 grey-scale plots of the intensity distribution in the focal volume are presented in the presence of typical lower order aberrations. The state of polarization in all graphs is linear with the plane of polarization parallel to the x-axis. The defocus range, going from left to right, extends over four focal depths ($|f| = \pi/2$) of $\Delta_z = \lambda/(4u_0)$; this quantity, defined in Eq.(2.31), is used in the case of high numerical aperture values, to be compared with $\Delta_z = \lambda/(2s_0^2)$ for low values of s_0. The upper row shows the energy density in the aberration-free case. The well-known broadening of the point-spread function in the cross-section parallel to the plane of polarization in the entrance pupil is clearly visible, leading to an overall elliptical profile of the point-spread function. In the second row, the coefficient $\alpha_{4,c}^0$, describing the phase departure in the entrance pupil due to spherical aberration, has been put equal to $\sqrt{2}$. This aberration value is such that the classical Strehl intensity, see [Born, Wolf

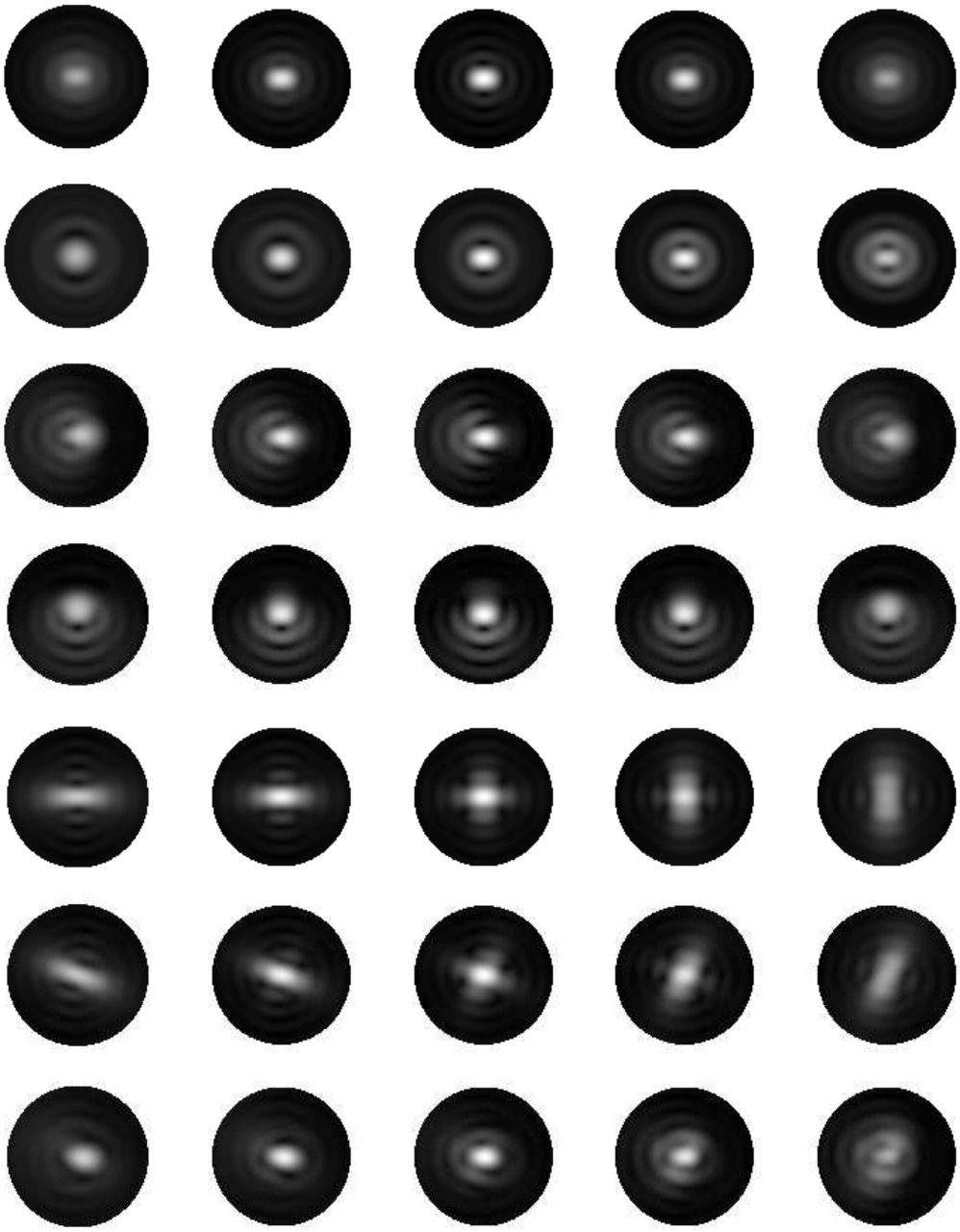

Fig. 3.1. Intensity of the point-spread function of a high-numerical-aperture imaging system ($s_0 = 0.95$). The columns pertain to the defocus parameter with $f = \pi, \pi/2, 0, -\pi/2, -\pi$, from left to right, going away from the exit pupil according to the sign convention. Radial size: $|r| \leq 3$. Upper row: aberration-free case; row 2: $\alpha^0_{4,c} = 1.41$; row 3: $\alpha^1_{3,c} = 1.79$; row 4: $\alpha^1_{3,s} = 1.79$; row 5: $\alpha^2_{2,c} = 1.55$; row 6: $\alpha^2_{2,s} = 1.55$; row 7: $\alpha^0_{4,c} = 0.81$, $\alpha^1_{3,c} = 1.03$, $\alpha^2_{2,c} = 0.89$. The grey-scale graphs have been normalized in each row to the top intensity in the focal plane with $f = 0$. The maximum intensity of the aberrated graphs in rows 2 to 7 is approximately 0.60 (Strehl intensity).

(2002)], would become 0.60. This means that the aberration pushes the quality of the imaging system beyond the 'just-diffraction-limited' level corresponding to the Strehl ratio value of 0.80. The columns on the right, corresponding to the defocus region beyond the nominal focal point F start to show a narrower ring-shaped pattern; closer to the exit pupil, the central lobe of the point-

spread function is broadened. This asymmetry with respect to 'best' focus is characteristic for spherical aberration. In the low aperture scalar case, it leads to sharp and narrow diffraction rings beyond focus, and a more blurred pattern at the short side of F, at least when the sign of $\alpha^0_{4,c}$ is positive like in Fig. 3.1. In the high numerical aperture case, the typical spherical aberration effects are somewhat blurred by the intrinsic 'unsharpness' that arises from the vector diffraction effects. The third and the fourth row are point-spread functions of an imaging system suffering from comatic aberration, in this case with a coefficient $\alpha^1_{3,c} = 1.79$ in the third row and the same value for $\alpha^1_{3,s}$ in the fourth row. The characteristic asymmetric pattern of comatic aberration is present in both cases. In the third row, the comatic blur is superimposed on the intrinsic blur in the x-direction due to the linear state of polarization. It also becomes apparent from the graphs that comatic aberration does not perturb the axial symmetry with respect to the nominal focal plane in F. In the fifth row we have introduced lowest order astigmatism with the coefficient $\alpha^2_{2,c} = 1.55$. The vector diffraction effects influence the widths of the focal lines in the x- and y-direction in the defocused state. The focal line in the y-direction, farther away from focus, has suffered a strong broadening due to the polarization effect. Note that with the chosen value of $\alpha^2_{2,c}$, the two outer focus settings approximately correspond to the sharp focal line positions predicted by geometrical optics. The sixth row shows, with the astigmatic aberration rotated by 45 degrees, the typical interaction between the vector 'blur' direction along the x-axis and the astigmatic effect that is diagonal. The net visual effect is a small extra rotation of the point-spread function towards the y-axis. Finally, the graphs in the seventh row correspond to a mixture of the three basic aberrations above, so that the total rms phase departure is the same and the Strehl intensity is again close to 0.60.

Certain azimuthal dependencies in the energy density patterns can be made visible by the subtraction of 'orthogonal' states of polarization. In this case, the subtraction of the two orthogonal linearly polarized patterns at 0 and 90 degrees with the x-axis yields

$$\begin{aligned}\Delta w_{l,0} = &\langle w_e^x(r,\phi,f)\rangle_{\pi/2} - \langle w_e^y(r,\phi,f)\rangle_0 = \\ &2s_0^2\,\Re\left[G_{0,2}(\beta,\beta) + G_{0,-2}(\beta,\beta) - 2G_{+1,-1}(\beta,\beta)\right]\ .\end{aligned} \tag{3.15}$$

The subtraction of two energy patterns belonging to diagonal linear polarization states gives rise to

$$\Delta w_{l,\pi/4} = \langle w_e^x(r,\phi,f)\rangle_{3\pi/4} - \langle w_e^y(r,\phi,f)\rangle_{\pi/4} =$$

$$2s_0^2\,\Im\left[G_{0,2}(\beta,\beta) - G_{0,-2}(\beta,\beta) + 2G_{+1,-1}(\beta,\beta)\right]\ . \tag{3.16}$$

The G-functions above, in the absence of aberrations, contain the basic 2ϕ-azimuthal dependence in the energy density, in general a mixture of the $\cos 2\phi$- and $\sin 2\phi$-function from their real and imaginary parts, depending on the orientation of the linear state of polarization. The addition of aberrations introduces higher and lower order ϕ-dependencies in the energy density function. This phenomenon plays an important role when studying the quality of an optical system with the aid of its through-focus point-spread functions.

3.1.2 Circular polarization (LC and RC)

If we substitute $p_y = -ip_x$ and $p_y = ip_x$, we define right- and left-handed circularly polarized light, respectively. This definition of polarization handedness follows from our convention $\exp\{i(kz - \omega t)\}$ for an outgoing plane wave in the positive z-direction. The energy density is proportional to

$$\begin{aligned}\langle w_e^{RC}(r,\phi,f)\rangle_0 \propto\, & G_{0,0}(\beta,\beta) + s_0^4\, G_{2,2}(\beta,\beta) \\ & +2s_0^2\, G_{1,1}(\beta,\beta)\end{aligned} \tag{3.17}$$

and, in a corresponding way,

$$\begin{aligned}\langle w_e^{LC}(r,\phi,f)\rangle_0 \propto\, & G_{0,0}(\beta,\beta) + s_0^4\, G_{-2,-2}(\beta,\beta) \\ & +2s_0^2\, G_{-1,-1}(\beta,\beta)\quad .\end{aligned} \tag{3.18}$$

The difference between right- and left-handed polarization density distributions thus equals

$$\begin{aligned}\Delta w_{C,0} = & s_0^4\ \left[G_{2,2}(\beta,\beta) - G_{-2,-2}(\beta,\beta)\right] \\ & +2s_0^2\ \left[G_{1,1}(\beta,\beta) - G_{-1,-1}(\beta,\beta)\right]\quad .\end{aligned} \tag{3.19}$$

In the aberration-free case, this difference is identical zero. However, in the presence of aberrations, the nonzero difference function with its specific azimuthal dependencies carries information on the aberration function of the optical system. Like for the linear state of polarization, this fact will be exploited later in this chapter in the part on the assessment of optical systems regarding their imaging quality.

3.1.3 Unpolarized or 'natural' light

The energy density in the case of incoherent ('natural') light is obtained by adding the energy density patterns corresponding to two orthogonal polarization states. We find

$$\langle w_e^N(r,\phi,f)\rangle = G_{0,0}(\beta,\beta) + s_0^2\left[G_{1,1}(\beta,\beta) + G_{-1,-1}(\beta,\beta)\right] + \frac{s_0^4}{2}\left[G_{2,2}(\beta,\beta) + G_{-2,-2}(\beta,\beta)\right] \quad . \tag{3.20}$$

In the aberration-free case, the energy density for natural light and circularly polarized light is equal. This is generally not the case in the presence of aberrations. The case of partially polarized light can be accounted for by defining a total energy density that is a weighted sum of a fully polarized pattern and an unpolarized pattern, the weight being determined by the degree of polarization.

3.1.4 Circularly symmetric states of polarization (radial and tangential)

Other states of polarization with a specific structure have been studied in the context of the angular momentum of light beams, in particular Gauss-Laguerre beam modes [Allen, Beijersbergen, Spreeuw, Woerdman (1992)], [He, Friese, Heckenberg, Rubinsztein-Dunlop (1995)]. These special beams have a spatially varying state of polarization over the beam cross-section and cannot be represented by a combination of two complex numbers specifying their constant x- and y-components. The Gauss-Laguerre beam modes apply to paraxial beams with a gradual decrease in field strenght as a function of radial position. To incorporate finite-size beams with a sharp aperture limitation as is common in imaging systems, we give below the Zernike expansion of radially or tangentially polarized beams, or, more generally, of polarized beams with circular symmetry. The expansion to be used is that of Eq.(2.64) in which the linear phase terms, carrying angular momentum, are present as $\exp(im\theta)$ with m also assuming negative values to allow for the positive or negative sign of angular momentum. Two sets of expansion coefficients are required to represent the x- and y-components of the field in the entrance pupil. We write the state of polarization of the incident field in the entrance pupil as, see [Braat, Dirksen, Janssen, van de Nes (2003)],

$$\begin{aligned} E_x &= A_0\cos(\theta+\theta_0), \\ E_y &= A_0\sin(\theta+\theta_0)\exp(i\epsilon_{xy}). \end{aligned} \tag{3.21}$$

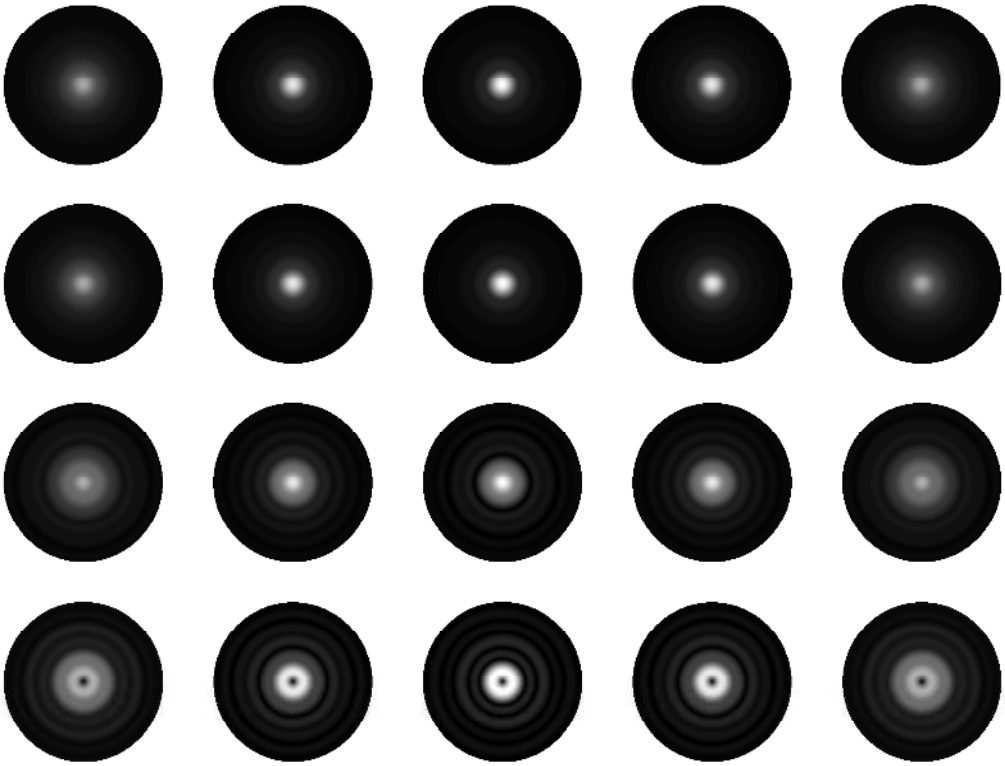

Fig. 3.2. Intensity of the point-spread function for various states of polarization in the entrance pupil of an aberration-free imaging system ($s_0 = 0.95$). The columns pertain to the defocus parameter with $f = \pi, \pi/2, 0, -\pi/2, -\pi$, from left to right. Radial size: $|r| \leq 3$. Upper row: incident light is unpolarized; row 2: circular polarization; row 3: radial polarization; row 4: tangential polarization.

With $\epsilon_{xy} \equiv 0$, we find as limiting cases radial polarization for $\theta_0 = 0$ and tangential or azimuthal polarization for $\theta_0 = \pi/2$. The constant phase ϵ_{xy} allows a gradual change from linearly polarized light along the x- and y-axis to elliptically polarized light with maximum eccentricity along the diagonal sections of the aperture.

Limiting ourselves to $\epsilon_{xy} = 0$, we can calculate the general coefficients $\beta^m_{n,x}$ and $\beta^m_{n,y}$ of the Zernike expansion by forming the inner products with the field components of Eq.(3.21). The details of the derivation are given in Appendix F; the result is given by

$$
\begin{aligned}
\beta^{+1}_{2n+1,x} &= f_c(n)\ \exp(i\theta_0), \\
\beta^{-1}_{2n+1,x} &= f_c(n)\ \exp(-i\theta_0), \\
\beta^{+1}_{2n+1,y} &= f_c(n)\ \exp\{i(\theta_0 - \pi/2)\},, \\
\beta^{-1}_{2n+1,y} &= f_c(n)\ \exp\{-i(\theta_0 - \pi/2)\}, \\
\text{with} \qquad f_c(n) &= (-1)^n\ \frac{2n+2}{(2n+1)(2n+3)},
\end{aligned}
\tag{3.22}
$$

and with $n = 0, 1, ..., n_{max}$, where the value of n_{max} depends on the convergence of the expansion. Some special states of polarization have been depicted in Fig. 3.2. In all cases, the phase departure of the focusing wave in the exit pupil is zero. With the through-focus planes of each column chosen as in Fig. 3.1, we first present the point-spread function intensity resulting from imaging with unpolarized light, obtained by adding with equal weights the intensity distribution belonging to two orthogonal states of polarization. The second row pertains to circularly polarized light, with no difference between right- or left-handed circular polarization in the aberration-free case. Moreover, as it is also suggested by Fig. 3.2, the point-spread functions in row one and two are identical in the aberration-free case, see Eqs.(3.17)-(3.18) and (3.20). In the third and fourth row we show through-focus point-spread functions corresponding to, respectively, radial and tangential polarization in the entrance pupil. The wavefront deformation in the exit pupil is still zero but nonzero complex Zernike coefficients $\beta^{\pm 1}_{2n+1,x}$ and $\beta^{\pm 1}_{2n+1,y}$ are needed now to represent the continuously varying state of polarization in the entrance pupil. In the case of radial polarization (row three), a strong z-component of the electric field is present in the optimum focal point F. It is seen that the radial polarization leads to an overall blurring effect when the total energy density is considered. Particular components of the electric field, in this case the z-component, give rise to a contribution to the energy density distribution that is significantly narrower than the typical point-spread function width. If a detecting material can be devised that is preferentially sensitive to the z-component, this point-spread function narrowing can be exploited in practice. In the fourth row with tangential polarization, we observe a zero on-axis, surrounded by a strong ring in the plane of best focus. This singular point in the energy density distribution can be exploited, for instance, when pointing accuracy in metrology is important. As a final remark we note that, apart from dimensional issues, the geometry of the electric field distribution for radial polarization is identical to that of the magnetic field in the case of tangential polarization, and vice versa.

3.2 Expression for the Poynting vector

In this subsection we briefly discuss the behavior of the components of the Poynting vector in a high-numerical-aperture system with general aberration and state of polarization in the entrance pupil. The energy flow in the focal volume is determined by the time averaged values of the cartesian components of the Poynting vector $\mathbf{S}$. In a passive system, the quantity $|< \nabla \cdot (\mathbf{E} \times \mathbf{B}) >| / \mu_0$,

integrated over a certain volume, determines the total power loss in that volume. If the loss is ohmic only, this quantity can also be written as $\sigma|\mathbf{E}|^2/2$ with σ the local electric conductivity in Sm^{-1}. The exposure in a photo-resist layer or the total charge collected by a detector thus depends on either the electric energy density or on the divergence of the Poynting vector. In practice, it will be easier to calculate exposure or detected charge by using the directly available electric energy density. However, despite the evident advantage of using $|\mathbf{E}|^2$, we present the expressions for the Poynting vector components to enable a comparison and numerical check of both approaches.

For harmonic fields, the time average of the Poynting vector reads

$$\langle \mathbf{S} \rangle = \frac{\epsilon_0 c^2}{2} \mathbf{E} \times \mathbf{B}^* \quad . \tag{3.23}$$

We write the Poynting vector in a medium (refractive index n_r) as

$$\mathbf{S} = (S_x, S_y, S_z) = \frac{\epsilon_0 n_r c}{8}\, k_0^2 f_L^2 s_0^4 |A|^2 (P_x, P_y, P_z), \tag{3.24}$$

where the incident electric field is represented by $a_x = p_x A, \;\; a_y = p_y A$, like we did before in the case of an optical system that is free of birefringence. Using Eqs.(2.65)-(2.66) for the electromagnetic field vectors, we obtain after some lengthy manipulation for the components P_x and P_y

$$\begin{aligned}
P_x = s_0 \Big\{ & -2ip_x^* p_y [\Im(G_{0,1}) + \Im(G_{0,-1})] \\
& + i \left\{ |p_x|^2 \left[G_{0,1}^* - G_{0,-1}^* \right] - |p_y|^2 \left[G_{0,1} - G_{0,-1} \right] \right\} \Big\} \\
- s_0^3 \Big[& \left\{ -2\Im(p_x p_y^*) + 1 \right\} \Im(G_{2,1}) - \left\{ 2\Im(p_x p_y^*) + 1 \right\} \Im(G_{-2,-1}) \\
& + 2i\Re(p_x p_y^*) \left\{ \Im(G_{1,-2} - \Im(G_{2,-1} \right\} \\
& + i(|p_x|^2 - |p_y|^2) \left\{ \Re(G_{1,-2} - \Re(G_{2,-1} \right\} \Big] \,, \qquad (3.25) \\
P_y = s_0 \Big\{ & 2ip_x p_y^* [\Re(G_{0,1}) - \Re(G_{0,-1})] \\
& + |p_x|^2 \left[G_{0,1} + G_{0,-1} \right] + |p_y|^2 \left[G_{0,1}^* + G_{0,-1}^* \right] \Big\} \\
+ s_0^3 \Big[& \left\{ -2\Im(p_x p_y^*) + 1 \right\} \Re(G_{2,1}) + \left\{ 2\Im(p_x p_y^*) + 1 \right\} \Re(G_{-2,-1}) \\
& + 2i\Re(p_x p_y^*) \left\{ \Re(G_{1,-2} - \Re(G_{2,-1} \right\}
\end{aligned}$$

$$-i(|p_x|^2-|p_y|^2)\left\{\Im(G_{1,-2}-\Im(G_{2,-1}\right\}\Big]\,. \qquad (3.26)$$

The z-component of the Poynting vector equals

$$\begin{aligned}P_z=&G_{0,0}-s_0^2\Big[i(|p_x|^2-|p_y|^2)\Im(G_{0,2})+2i\Re(p_xp_y^*)\Re(G_{0,2})\\&+i(|p_x|^2-|p_y|^2)\Im(G_{0,-2})-2i\Re(p_xp_y^*)\Re(G_{0,-2})\Big]\\&-\frac{s_0^4}{2}\Big[\left\{1-2\Im(p_xp_y^*)\right\}G_{2,2}+\left\{1+2\Im(p_xp_y^*)\right\}G_{-2,-2}\Big].\end{aligned} \qquad (3.27)$$

The real parts of the above expressions are needed to obtain the time-averaged energy flow and to eliminate the reactive part of the Poynting vector, yielding the adapted Poynting vector components

$$\begin{aligned}P_{x,r}=&s_0\Big\{-2\Im(p_xp_y^*)\Im\left(G_{0,1}+G_{0,-1}\right)+\Im\left(G_{0,1}-G_{0,-1}\right)\Big\}\\&+s_0^3\Big\{+2\Im(p_xp_y^*)\Im\left(G_{2,1}+G_{-2,-1}\right)-\Im\left(G_{2,1}-G_{-2,-1}\right)\Big\}\,,\end{aligned} \qquad (3.28)$$

$$\begin{aligned}P_{y,r}=&s_0\Big\{-2\Im(p_xp_y^*)\Re\left(G_{0,1}-G_{0,-1}\right)+\Re\left(G_{0,1}+G_{0,-1}\right)\Big\}\\&+s_0^3\Big\{-2\Im(p_xp_y^*)\Re\left(G_{2,1}-G_{-2,-1}\right)+\Re\left(G_{2,1}+G_{-2,-1}\right)\Big\}\,,\end{aligned} \qquad (3.29)$$

$$P_{z,r}=G_{0,0}-\frac{s_0^4}{2}\Big\{\left(G_{2,2}+G_{-2,-2}\right)-2\Im(p_xp_y^*)\left(G_{2,2}-G_{-2,-2}\right)\Big\}\,. \qquad (3.30)$$

In Fig. 3.3 we have plotted these Poynting vector components in three cross-sections of the focal volume with $f=\pi,0,-\pi$. The top row (no aberrations) shows a uniformly directed flow on both sides of best focus, towards the focal point F in front of F and outgoing beyond F. In the plane with $f=0$, the only nonzero flow component is that along the z-axis. Despite the non-circularly symmetric energy density in the high-numerical-aperture case, the flow pattern of the Poynting vector is circularly symmetric. This is because of the complementary field distributions of the **E**- and **B**-vector, yielding a circularly symmetric function regarding their product. At a very fine scale, not visible in the Figure, vortices in the flow pattern are possible, close to the regions in space of zero energy density where the z-component of the Poynting vector changes sign, see [Richards, Wolf (1959)]. In the second row of Fig. 3.3, in the presence of spherical aberration, the global flow pattern of the aberration-free case is still there, but finite radial components are visible

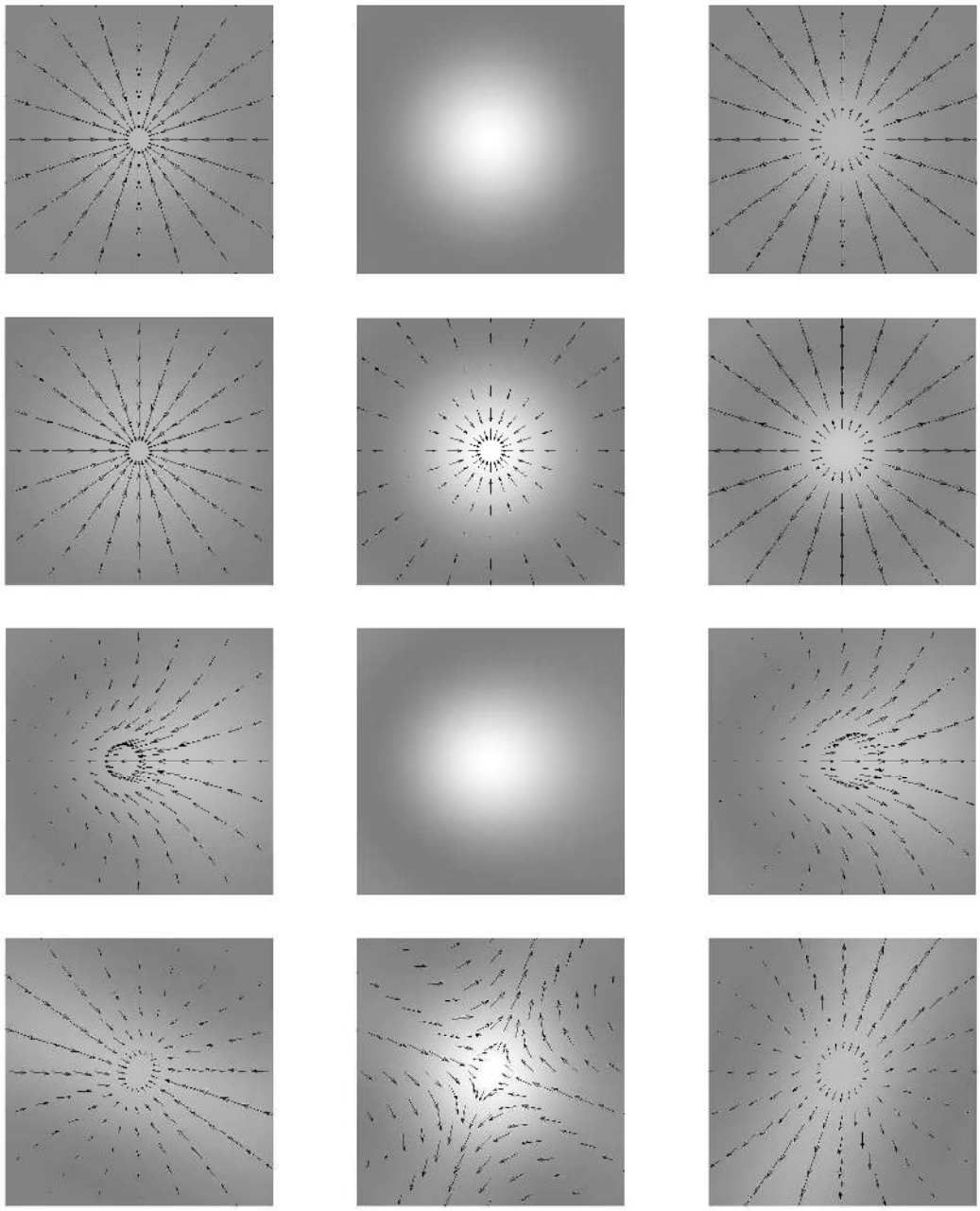

Fig. 3.3. Flow lines of the electromagnetic energy in the focal region of a high-numerical-aperture beam ($s_0 = 0.95$, linear polarization x-direction), going from a defocused plane closer to the exit pupil, via the best focus plane in F to a defocused plane beyond F (the defocus distance equals two focal depths). Lateral dimensions in x- and y-direction are $-1.11 \leq x, y \leq +1.11$ in dimensionless units of λ/s_0. The x- and y-components of the Poynting vector are represented by arrows; the amplitude of the z-component is represented by the grey-shading in each plane z=constant. Top row: aberration-free case; row 2: $\alpha^0_{4,c} = 1.41$; row 3: $\alpha^1_{3,c} = 1.79$; row 4: $\alpha^2_{2,s} = 1.55$.

now in the plane $f = 0$ because of the 'distributed' axial focus in the beam. The asymmetry around focus, already present in the energy density function, is also visible in the Poynting vector flow pattern. In the third row, the left graph shows the enhanced energy flow in the x-direction towards the asymmetrical coma distribution in the plane $f = 0$. On the other side of the best focal plane,

the outflow in the x-direction is also stronger to get back to the balanced flow pattern at large defocus value in the far-field. Finally, in the fourth row, we observe in the energy flow pattern the effect of the splitting of the ideal focal point into two focal lines, due to the astigmatism at 45 degrees. The slight change in orientation of the 'focal lines' towards the y-axis is due to the initial state of linear polarization that was chosen along the x-axis.

3.2.1 The aberration-free system as a special case

It is interesting to reduce the general expressions for the Poynting vector components to their simpler form in the case of an aberration-free imaging system. In that case, we put $\beta_n^m = 0$ with the exception of $\beta_0^0 \equiv 1$. The G-functions reduce to

$$G_{kl}(\beta) = \exp\{i(k-l)\phi\}\, \Psi^0_{0;k,l}(r,f), \tag{3.31}$$

with the shorthand notation $\Psi^0_{0;k,l}(r,f) = V^0_{0,k}(r,f)V^{0*}_{0,l}(r,f)$. After some manipulation, the cartesian Poynting vector components are found to be

$$\begin{aligned} P_{x,r} = {} & 2s_0\Big\{2\Im(p_x p_y^*)\Re\{\Psi^0_{0;0,1}(r,f)\}\sin\phi + \Im\{\Psi^0_{0;0,1}(r,f)\}\cos\phi\Big\} \\ & +2s_0^3\Big\{2\Im(p_x p_y^*)\Re\{\Psi^0_{0;2,1}(r,f)\}\sin\phi - \Im\{\Psi^0_{0;2,1}(r,f)\}\cos\phi\Big\}, \end{aligned} \tag{3.32}$$

$$\begin{aligned} P_{y,r} = {} & 2s_0\Big\{-2\Im(p_x p_y^*)\Re\{\Psi^0_{0;0,1}(r,f)\}\cos\phi + \Im\{\Psi^0_{0;0,1}(r,f)\}\sin\phi\Big\} \\ & +2s_0^3\Big\{-2\Im(p_x p_y^*)\Re\{\Psi^0_{0;2,1}(r,f)\}\cos\phi - \Im\{\Psi^0_{0;2,1}(r,f)\}\sin\phi\Big\}, \end{aligned} \tag{3.33}$$

$$P_{z,r} = \Psi^0_{0;0,0}(r,f) - s_0^4\Psi^0_{0;2,2}(r,f)\ . \tag{3.34}$$

Because of the basic circular symmetry of many diffraction problems, it is appropriate to express the Poynting vector components in cylindrical coordinates and we find for the polar components

$$\begin{aligned} P_r &= 2s_0\ \Im\left[\Psi^0_{0;0,1}(r,f) - s_0^2\Psi^0_{0;2,1}(r,f)\right], \\ P_\phi &= -4s_0\Im(p_x p_y^*)\ \Re\left[\Psi^0_{0;0,1}(r,f) - s_0^2\Psi^0_{0;2,1}(r,f)\right]. \end{aligned} \tag{3.35}$$

Some conclusions can be drawn from the above expressions. Using the property $\Psi^0_{0;k,l}(r,-f) = \Psi^{0*}_{0;k,l}(r,f)$, we can state that

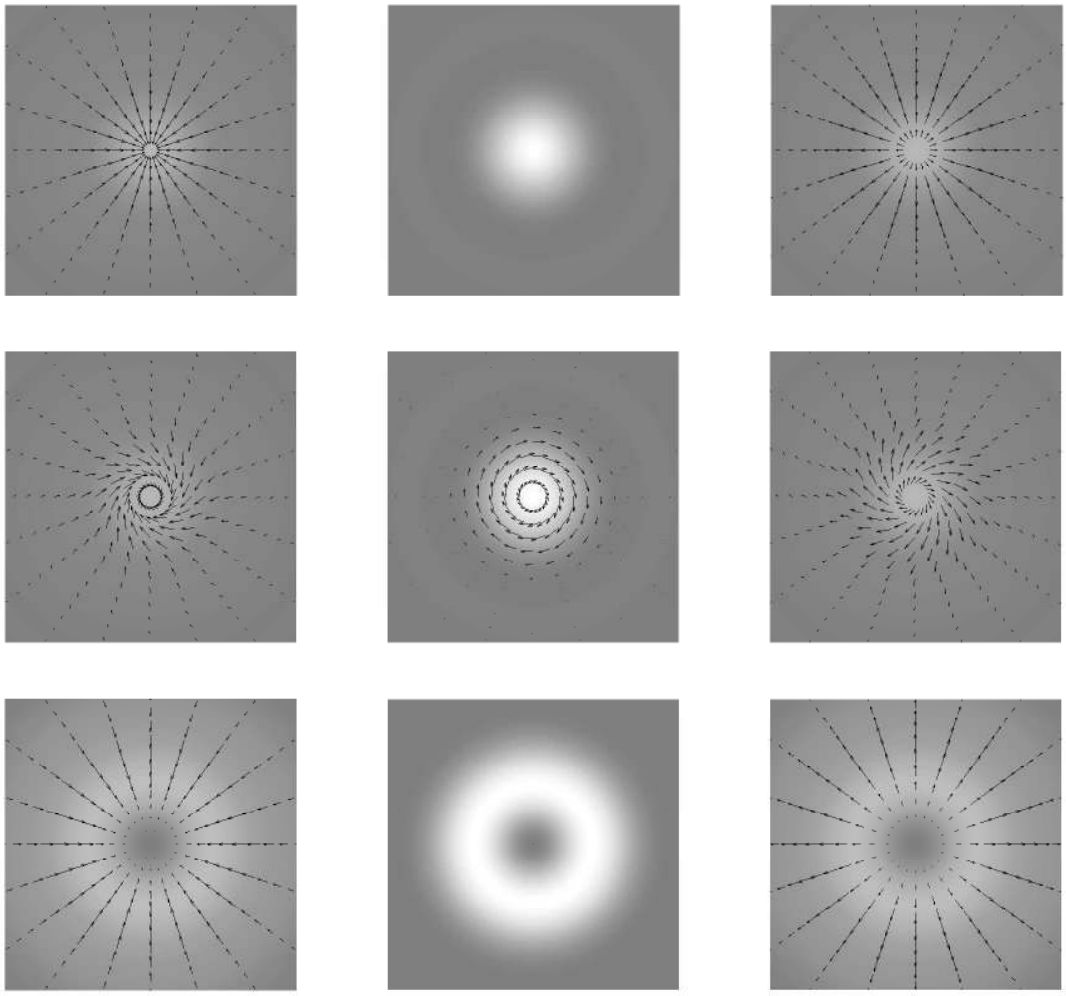

Fig. 3.4. Flow lines of the Poynting vector in the focal region of an ideal imaging system ($s_0 = 0.95$) for various states of polarization in the entrance pupil. Left column: $f = \pi$; central column: $f = 0$, right column: $f = -\pi$. Lateral dimensions in x- and y-direction are $-1.11r \leq x, y \leq +1.11$. Upper row: linear polarization along the x-axis. Middle row: Right-handed circularly polarized light ($p_x = 1,\ p_y = -i$). Bottom row: radial polarization.

- On-axis ($r = 0$), the power flow is directed along the axis of the beam.
- The radial component changes sign through focus.
- The azimuthal component is only present if the incident radiation is not linearly polarized ($arg(p_x) \neq arg(p_y)$), see [Boivin, Dow, Wolf, 1967], [Stallinga (2001)]. This corresponds to the presence of angular momentum in the focused beam.
- The azimuthal component is maximum in the case of circularly polarized light.
- The azimuthal component maintains its sign on both sides of the optimum focus.
- For large s_0, all components can locally change sign with respect to their average values if the (r, f)-dependent function becomes zero. This can give

rise to regions where the energy flow is in the negative z-direction and also to the appearance of vortices in the energy flow pattern.

- Regardless of the incident state of polarization, the z-component possesses circular symmetry. This is because the Poynting vector describes the energy flow of both electric and magnetic energy. Any lack of circular symmetry in the energy densities of these contributions is cancelled in their sum.
- In the low-aperture case, the z-component is the only surviving only.

In Fig. 3.4 we have presented some graphs that illustrate the observations made above for the aberration-free case. With the upper row (linear polarization in the x-direction) as a reference, we see in the second row the influence of circular polarization in the entrance pupil on the flow pattern in the focal region. The state of polarization is right-handed, the flow circulation in focus becomes left-handed. Everywhere on the optical axis the azimuthal component is zero. The beam possesses a certain amount of angular momentum. With the positive z-direction as the viewing direction, we observe that the rotation sense of the electric field vector is left-handed for RC-polarized light and this rotation sense is in accordance with the sign of the angular momentum of the electric field distribution in the focal region. In the bottom row, we have plotted the power flow in the case of radial polarization. Because of the interchangeability of the **E**- and **B**-vector between radial and azimuthal polarization, the flow pattern would have been the same for azimuthal polarization. It is important to remark that the z-component of the Poynting vector is zero everywhere on-axis, despite the fact that the energy density is finite on-axis in the case of radial polarization. The same holds for the magnetic energy density in the case of azimuthal polarization. However, because of the vanishing transversal components of either the electric (radial polarization) or magnetic (azimuthal) field components on the z-axis, there is no power flow possible in the z-direction on the axis itself.

In the preceding sections, a thorough description has been presented of the energy density and the intensity in the focal region. Various methods are available to calculate these quantities. The propagation from the exit pupil sphere to the image region is the crucial and most labor-intensive step for obtaining the above quantities. Numerical methods are frequently used, in most cases based on the Fast Fourier Transform scheme. These methods can handle a large variety of practical situations; with the correct sampling density quite arbitrary geometries are tractable. Analytic methods generally are less versatile but they have the advantage of providing an immediate solution of the diffraction integral, thus saving much computational effort. Considerations of this nature are important when addressing the so-called 'inverse problem', how to obtain reliable information on the properties of the optical imaging system to assess its quality. Although an excellent method like interferometry is available to evaluate the aberrations of an optical system, this method is not always easily implemented in a practical situation. Special sources, preferably lasers, are required at the specific design wavelengths of the optical system. Perfect optics are needed in the reference branch of an amplitude-splitting interferometer or a wavefront splitting device in a shearing interferometer. Coherence length requirements have to be satisfied and the necessary mechanical and environmental stability is difficult to obtain. For these reasons, the reconstruction or retrieval of system information from images in the focal region is interesting because this method avoids most of the subtle experimental conditions encountered in interferometry. The images to be studied for 'retrieval' of system parameters can be of a general nature or they can be of the simplest form, the image of a point source, the so-called point-spread function. After a brief discussion of the more general methods for phase retrieval, we will focus in this section on the point-source or quasi-point-source option as it is, experimentally, most easily realized. The quasi-point-source is the practical compromise between smallest possible object dimension and light efficiency in the measurement set-up. The analyses in this section will be limited to the scalar approximation of image formation, valid for relatively low-numerical-aperture imaging systems. The extension of the inverse problem to high-numerical-aperture will be treated in the following section.

The most important quantity impairing the performance of an optical instrument is its phase aberration. It may be due to environmental perturbations like atmospheric turbulence in astronomical imaging, it may be caused by the design of the system or induced by fabrication and mounting errors of the system components, such as the improper figuring of an aspheric optical surface. In this subsection we briefly discuss the model for retrieval of phase information from intensity measurements based on an approximate solution of the scalar wave equation for quasi-parallel or low-aperture beams. The starting point of the analysis is the so-called paraxial or parabolic Helmholtz wave equation [Kogelnik (1965)],

$$\nabla_t^2 Q + 2ik\frac{\partial Q}{\partial z} + k^2 Q = 0, \tag{4.1}$$

with $Q(x, y; z)$ the slowly varying amplitude in the z-direction of the scalar solution U for the wave

$$U(x, y, z; t) = Q(x, y; z) \exp\{i(kz - \omega t)\}. \tag{4.2}$$

The circular wave number of the wave propagating in the z-direction is again given by k, the circular frequency is ω. The ∇_t^2-sign means that only the second derivatives in the transversal direction need to be taken. The complex amplitude is more explicitly written as $Q(x, y; z) = A(x, y; z) \exp\{i\phi(x, y; z)\}$ where, again, the parameter-wise notation of the z-coordinate indicates that the functions only slowly vary as a function of this variable.

The intensity of the wave phenomenon is given by $|U|^2 = QQ^* = I$ and an equation can be derived [Teague (1983)] that relates the measured intensity I to the phase function $\phi(x, y; z)$ of the wave, the so-called Intensity Transport Equation (ITE). Multiplying Eq.(4.1) by Q^* and the complex conjugate expression of Eq.(4.1) by Q itself and subtracting the results, we obtain after some rearrangement

$$2ik\frac{\partial A^2}{\partial z} + 4iA\left[\frac{\partial A}{\partial x}\frac{\partial \phi}{\partial x} - \frac{\partial A}{\partial y}\frac{\partial \phi}{\partial y}\right] + 2iA^2\left[\frac{\partial^2 \phi}{\partial x^2} + \frac{\partial^2 \phi}{\partial y^2}\right] = 0, \tag{4.3}$$

which is commonly written as the ITE-equation in compact notation

$$-k\frac{\partial I}{\partial z} = \nabla_t \cdot (I\nabla_t\phi) = I\nabla_t^2\phi + \nabla_t I \cdot \nabla_t\phi. \tag{4.4}$$

If the intensity across the beam is locally constant, the second term on the right side of Eq.(4.4) is zero and the axial derivative of the intensity is proportional to the wave front curvature. In regions where the intensity across the beam varies, the gradient or slope of the wavefront determines the transfer of intensity across the beam (see Fig. 4.1) Methods to solve the intensity transport equation

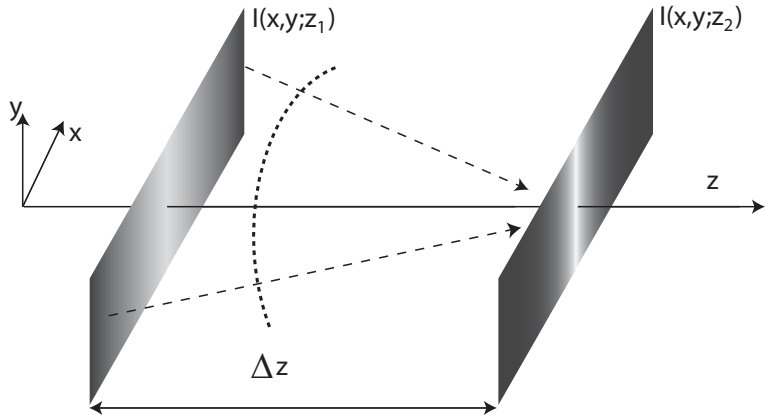

Fig. 4.1. Schematic drawing of a quasi-parallel beam and the variation of its intensity in the axial and in the transverse beam direction due to, for instance, wave front curvature. The lower intensity regions have been shaded. The energy propagation direction is given by the arrows, the dashed curve indicates the curved wavefront. All effects have been strongly exaggerated in the figure.

using Green's functions have been presented in [Woods, Greenaway (2003)]. The experimental evaluation of the z-derivative of the intensity is generally done by measuring the intensity distribution in two axially shifted planes. The ITE-based phase retrieval method is limited to paraxial beams. In this chapter, the interest is focused on the characterization of high-quality imaging systems where, in most cases, imaging pencils with a medium to large opening angle are encountered. The characterization of such systems is treated in the following subsections.

4.2 The optical inverse problem for finite-aperture imaging systems

The aberration of an optical imaging systems influences its complex 'lens' transmission function. Measurements only give access to the intensity, the modulus squared of the complex amplitude. In this subsection we discuss inverse schemes that go back to the complex lens function in a generally unambiguous way using appropriate intensity measurements. However, a unique way back to

the lens function is not guaranteed in all cases, among others given the problem of phase retrieval from data that extend beyond the basic retrieval interval for phase data of $[-\pi, +\pi]$ (phase-unwrapping problem). The first scheme for

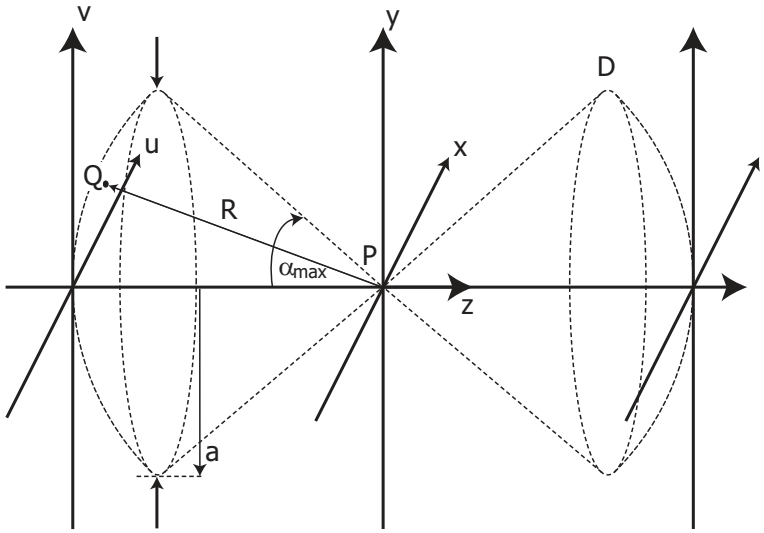

Fig. 4.2. Schematic drawing of the exit upil domain (far field, coordinates $Q(u, v)$) and the image domain (coordinates $P(x, y, z)$). The propagation forth and back between the two domains is governed by the scalar diffraction integral. In a different set-up, the light is focused first on the object in a plane $z = z_0$; the far field then becomes available on the detection sphere D. The angular extent α_{max} of the imaging pencil has been exaggerated in the figure.

phase retrieval or pupil function reconstruction goes back to [Gerchberg, Saxton (1971)]. The method is based on the frequent back and forth propagation of the complex amplitude between the image plane and the exit pupil, see Fig. 4.2. A Fast Fourier Transform (FFT) is executed and the Fraunhofer or Fresnel approximation is used for calculating the pathlength from a general point Q in the exit pupil to a point P in the image plane. After each forward and backward propagation, the calculated results are updated to better match them with the measurements and the physical boundary condition (non-negativity of the intensity). Denoting the image plane complex amplitude in a certain plane $z = z_0$ by $f(x, y, z_0)$, we have the basic Fourier relationship

$$
\begin{aligned}
F(k_x, k_y; z_0) &= \int_{-\infty}^{+\infty}\int_{-\infty}^{+\infty} f(x, y, z_0) \exp\{-i(k_x x + k_y y)\} dx dy, \\
f(x, y, z_0) &= \frac{1}{(2\pi)^2} \int_{-\infty}^{+\infty}\int_{-\infty}^{+\infty} F(k_x, k_y; z_0) \exp\{+i(k_x x + k_y y)\} dk_x dk_y,
\end{aligned}
\tag{4.5}
$$

where k_x and k_y are the optical 'far field' coordinates and where we have neglected the exact radiation factors that should precede the integrals. Both

$F(k_x, k_y; z_0)$ and $f(x, y, z_0)$ are complex-valued according to

$$\begin{aligned} F(k_x, k_y; z_0) &= |F(k_x, k_y; z_0)| \exp\{i\phi_F(k_x, k_y; z_0)\}, \\ f(x, y, z_0) &= |f(x, y, z_0)| \exp\{i\phi_f(x, y, z_0)\}. \end{aligned} \tag{4.6}$$

In the most comfortable situation, both the optical far field $|F|$ and near field $|f|$ are accessible to measurements via their squared moduli. In other circumstances, for instance when measuring the far field distribution scattered from a microscopic periodic transmitting object, $|F|$ is available and we want to get back to the object transmission function f, including its phase ϕ_f. In the case of the single intensity measurement, a supplementary property of the object needs to be specified. This could be, for example, the frequently occurring boundary condition that the object is partly obscuring the light, yielding a transmission function $f(x, y; z_0)$ that should be real and positive. The Gerchberg-Saxton algorithm then proceeds as follows

(1) produce an estimate of the object and calculate its Fourier transform to obtain the far field,
(2) replace the calculated modulus of the far field by its measured value to obtain a better estimate of the far field,
(3) apply an inverse Fourier Transform to this function to obtain an image estimate,
(4) replace the modulus of the image by the measured modulus to further improve the image.

Following the analysis in [Fienup (1982)], the equations governing the four steps in the n^{th} cycle are, starting with, for instance, the n^{th} estimate f_n of the object function

$$F_n(k_x, k_y; z_0) = |F_n(k_x, k_y; z_0)| \exp\{i\phi_{F,n}(k_x, k_y; z_0)\} = \mathcal{F}[f_n(x, y, z_0], \tag{4.7}$$

$$F_n^{'}(k_x, k_y; z_0) = |F(k_x, k_y; z_0)| \exp\{i\phi_{F,n}(k_x, k_y; z_0)\}, \tag{4.8}$$

$$f_n^{'}(x, y, z_0) = |f_n^{'}(x, y, z_0)| \exp\{i\phi_{f,n}^{'}(x, y, z_0)\} = \mathcal{F}^{-1}[F_n^{'}(k_x, k_y; z_0], \tag{4.9}$$

$$\begin{aligned} f_{n+1}(x, y, z_0) &= |f(x, y, z_0)| \exp\{i\phi_{f,n+1}(x, y, z_0)\} \\ &= |f(x, y, z_0)| \exp\{i\phi_{f,n}^{'}(x, y, z_0)\}. \end{aligned} \tag{4.10}$$

Here, $\mathcal{F}$ and $\mathcal{F}^{-1}$ stand for the forward and backward Fourier Transform operations; the primed quantity $F_n^{'}$ has been obtained by using the measurement result for $|F|$. In a comparable way, the non-primed quantity f_{n+1} in the fourth equation has been obtained from the primed $f_n^{'}$ by substituting the measure-

ment result of $|f|$. If a complete measurement of F or f is not available, partial adjustments can be made in steps 2 and 4. These are related to possible negative intensity values or to the spreading of F or f outside a fixed domain for these functions whose limits are known *a priori*. The whole cycle is repeated until no further improvement is obtained. This means that either the optimum image or pupil function has been found or that stagnation has occurred. The improvement is monitored by calculating a merit or cost function at each cycle according to

$$M_{n,f} = \iint \left| f_{n+1}(x,y,z_0) - f_n^{'}(x,y,z_0) \right|^2 dxdy, \tag{4.11}$$

$$M_{n,F} = \frac{1}{(2\pi)^2} \iint \left| F_n^{'}(k_x,k_y;z_0) - F_n(k_x,k_y;z_0) \right|^2 dk_x dk_y, \tag{4.12}$$

where either the image plane or the far-field data are monitored.

Convergence of the merit function can be proved in the following way. Applying Parseval's theorem first to $M_{n,F}$ we find

$$M_{n,F} = \frac{1}{(2\pi)^2} \iint \left| F_n^{'}(k_x,k_y;z_0) - F_n(k_x,k_y;z_0) \right|^2 dk_x dk_y = \iint \left| f_n^{'}(x,y,z_0) - f_n(x,y,z_0) \right|^2 dxdy. \tag{4.13}$$

Inspection of Eqs.(4.7)-(4.10) yields the result

$$|f_n^{'} - f_n| \geq \left| |f_n^{'}| - |f| \right| = |f_n^{'} - f_{n+1}|, \tag{4.14}$$

since the argument values of the complex quantities $f_n^{'}$ and f_n are different in general. This allows us to write

$$\frac{1}{(2\pi)^2} \iint \left| F_n^{'}(k_x,k_y;z_0) - F_n(k_x,k_y;z_0) \right|^2 dk_x dk_y \geq \iint \left| f_{n+1}(x,y,z_0) - f_n^{'}(x,y,z_0) \right|^2 dxdy, \text{ or: } \quad M_{n,F} \geq M_{n,f}. \tag{4.15}$$

In an analogous manner, Parseval's theorem applied to $M_{n,f}$ yields the result $M_{n,f} \geq M_{n+1,F}$, which leads to the conclusion that each iteration cycle will produce smaller (or equal) values of the merit function, defined either in the far-field or in the image domain. The original method by Gerchberg and Saxton can be classified in the more general framework of optimization methods; it then becomes a special case of the method of steepest descent.

The initial solution to optical inverse problems required the measurement of one intensity pattern, subject to certain constraints in the corresponding Fourier domain, or the measurement of two intensity patterns in both Fourier domains. The success of a solution method strongly depends on a fast propagation algorithm to switch between the two domains; the preferred tool to carry out this propagation is the Fast Fourier Transform. If it is not possible to have access to both domains or if the measurements in the second domain add virtually no information, the inverse problem can be extended to more than one measurement in a single domain. The first suggestion to do so goes back to [Gonsalves (1982)] and, in the case of sufficiently small aberration, the procedure for unique phase retrieval using two intensity measurements is explained as follows [Gonsalves (2001)]. In Fig. 4.3 we have depicted a system producing

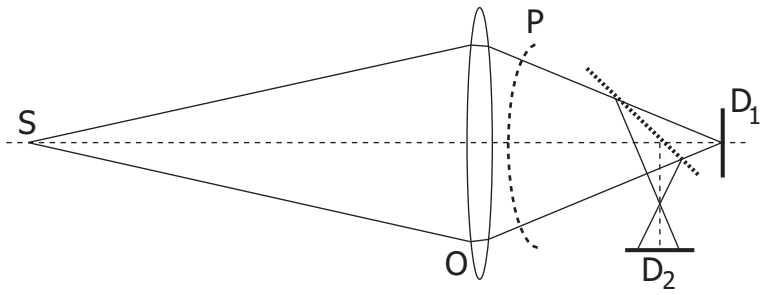

Fig. 4.3. A simple set-up to produce simultaneously two intensity patterns on the detectors D_1 and D_2 of an object. The required phase diversity between the two detected images is obtained by the defocusing (heavily exaggerated in the figure) of the point-spread function on D_2. The object is a point source S, the exit pupil of the optical system O has been denoted by P.

phase diversity by means of the beam splitter that delivers a defocused image on detector D_2. In what follows, both the aberrations of the system O itself and the defocusing on the second detector are small with respect to the wavelength λ of the light. The pupil function of the imaging system O is now given by

$$P = A\exp[i\Phi] \approx A[1 + i\Phi] = A + i[A\Phi_1 + A\Phi_2] = A + i[\Psi_1 + \Psi_2], \quad (4.16)$$

where we have suppressed, for ease of notation, the dependence of the functions on the pupil coordinates (u, v). Moreover, we have split the phase function Φ in two parts, an even part Φ_1 and an odd part Φ_2. The total phase departure Φ should remain small, typically $\leq \pi/2$. The amplitude function A is supposed to be real and positive $(0 < A \leq 1)$. If the detector D_1 is positioned in the

nominal imaging plane, the amplitude point-spread function is given by the Fourier transform of the pupil function P and is written

$$p = a + i(\psi_1 + \psi_2) = a + \psi_3 + i\psi_1, \tag{4.17}$$

with the lower-case symbols indicating the Fourier transforms of the corresponding functions in the pupil domain. The Fourier transform ψ_1 of the even function Ψ_1 is real and even. Because Ψ_2 is odd, its transform ψ_2 is purely imaginary and odd; for that reason it has been replaced by $\psi_3 = i\psi_2$ with ψ_3 real and odd to have only real functions in Eq.(4.17). The measured intensity on D_1 is proportional to pp^*, yielding

$$S_{D_1} = S_{11} + S_{12} = (a^2 + \psi_1^2 + \psi_3^2) + 2a\psi_3, \tag{4.18}$$

where we have split up the detector signal in an even part S_{11} and an odd part S_{12}. The function $\psi_2 = -i\psi_3 = -iS_{12}/(2a)$ is purely imaginary. After applying a backward or inverse Fourier Transform we get the result $A\Phi_2 = \Im\{\Psi_2\}$ for the odd part of the pupil function.
Having obtained the odd part of the pupil function, Eq.(4.18) allows to find the function ψ_1 using S_{11}, the even part of the detector signal, and retrieve $A\Phi_1$ using $\psi_1 = \sqrt{S_{11} - a^2 - \psi_3^2}$ and applying an inverse Fourier Transform to this function. The problem in doing this is the uncertainty about the sign when taking the square root. Phase diversity is a useful tool to eliminate this problem. The defocusing in the second measurement branch corresponds to a modified pupil function

$$P = A\exp[i(\Phi + \Phi_d] \approx A + i[\Psi_1 + \Psi_2 + \Psi_d], \tag{4.19}$$

with $\Psi_d = A\Phi_d$ and Φ_d the quadratic phase function due to defocusing, again small in amplitude. Using the same arguments as above, the signal on the second defocused detector is now given by

$$S_{D_2} = S_{21} + S_{22} = (a^2 + \psi_3)^2 + (\psi_1 + \psi_d)^2, \tag{4.20}$$

where ψ_d is the Fourier transform of the defocus function $A\Phi_d$. Combining the two detector measurements we write

$$S_{D_2} = S_{D_1} + 2\psi_1\psi_d + \psi_d^2\ , \tag{4.21}$$

with the solution

$$\psi_1 = \frac{S_{D_2} - S_{D_1} - \psi_d^2}{2\psi_d}. \tag{4.22}$$

Finally, the value of $A\Phi_1$ is obtained after applying the backward Fourier Transform to ψ_1 and taking the real part of it. Possible divisions by zero in obtaining ψ_2 above and ψ_1 in Eq.(4.22) can be numerically avoided by replacing a division by a by the expression $a/(a^2 + \epsilon)$ where the value of ϵ decides about the allowed range of function values of the ψ_1- and ψ_2-functions.

The basic approach of phase diversity as described above has been extended to problems of a more general nature [Fienup (1999)], for instance in the context of the Hubble space telescope recovery action, or the analysis of microscope objectives [Wesner, Heil, Sure (2002)]. The 'diversity' in images to be treated can be extended to the wavelength domain (broadband imaging), to varying aberration settings and to changes in pupil geometry. The extension to broadband imaging is especially interesting when dealing with astronomical images of extremely weak objects (photon-starved regime); a restriction to quasi-monochromatic detection would give rise to a prohibitively low signal-to-noise ratio of the corresponding images.

5 Quality assessment using the Extended Nijboer-Zernike diffraction theory

In this section we focus on the retrieval of the pupil function using an expansion in terms of Zernike polynomials. The coefficients of the expansion are obtained by means of an inversion or retrieval process that uses as input the data from various intensity patterns collected in the focal region of the optical system. To be able to treat these defocused intensity patterns, an analytic extension of the Nijboer-Zernike theory was recently devised [Janssen (2002)], [Braat, Dirksen, Janssen (2002)]. The out-of-focus extension of the classical Nijboer-Zernike diffraction theory allows for a fast and numerically stable forward propagation from the exit pupil to the focal 'volume' of the imaging system. This can be done independently for each of the amplitude and intensity patterns belonging to a typical Zernike aberration. In this way, Fast Fourier Transform methods can be avoided. Although the latter are reputedly fast with respect to the classical numerical evaluation of a diffraction integral, they still constitute the major numerical burden in an inversion process. Because of the discontinuous behaviour of the pupil function, high sample rates are needed. A semi-analytic approach as made possible by using the extended Nijboer-Zernike theory offers very substantial advantages in the speed with which an inversion can be carried out. Moreover, due to the analytic decomposition of the inversion problem, certain computational tasks are independent of the parameter values and can be carried out beforehand, making the effective inversion operation extremely fast. Both the amplitude and phase part of the pupil function can be retrieved by using the complex Zernike coefficient expansion that was given in Eq.(2.27) for the scalar diffraction case and in Eq.(2.64) for the vector diffraction case. Due to the limited space available, most considerations in this section are of a global nature; analytic and computational details can be found in the references.

We first treat the retrieval process for relatively low numerical aperture systems using the scalar diffraction model. This is a good approximation up to aperture values of 0.60 in air, or equivalently, up to a full cone convergence angle of the focused pencil below 75 degrees, independently of the refractive index of the image space medium. An extension to higher aperture values first needs an adaptation of the defocus factor in the diffraction integral from the quadratic form to the exact expression at high numerical aperture. With this extension, one can still adequately describe imaging up to a numerical aperture value of, say, 0.85 if the imaging is carried out with natural light so that polarization effects in the focal region are not yet pronounced, see [Dirk-

sen, Braat, Janssen, Leeuwestein (2005)] and [van der Avoort, Braat, Dirksen, Janssen (2005)]. But in the case of fully polarized illumination in the entrance pupil and imaging with high numerical aperture, one should use the full vector diffraction integral and the complete parametric description of the pupil function according to Eq.(2.64). With this expansion one can detect possible birefringence introduced by the optical system, a non-negligible factor of quality deterioration in imaging systems, especially at high numerical aperture. The limits of applicability of the extended Nijboer-Zernike diffraction model are given in practice by the restrictions on the illumination. The illumination of the entrance pupil should basically be done with a point source, or, in practice, a source that is much smaller than the diffraction unit λ/s_E in object space, with s_E the object side numerical aperture of the optical system. Because of the limited throughput of such a tiny source, it is important to be able to extend the model to sources with a finite lateral extent. This can be done by including the analytically known non-uniform far-field pattern of a finite source in the effective pupil function of the optical system [van der Avoort, Braat, Dirksen, Janssen (2005)]. In this way, the model is made applicable to practical experimental circumstances where exposure time or detector sensitivity are critical factors.

5.1 Scalar retrieval process using the Extended Nijboer-Zernike theory

The starting point for the retrieval process is the analytic expression for the complex amplitude in the focal region that was obtained in Section 2.6, using the result for the diffraction integral of Eq.(2.47). We describe the complex amplitude distribution on the exit pupil sphere, in analogy with Eq.(2.27) by

$$P(\rho,\theta) = E(\rho,\theta)\exp\{i\Phi(\rho,\theta)\} = \sum_{nm} \beta_n^m \; R_n^{|m|}(\rho) \; \exp\{im\theta\}, \tag{5.1}$$

where we have used the symbol β_n^m for the complex expansion coefficients for the complete pupil function to distinguish them from the (real) expansion coefficients α_n^m that are related to the expansion of the phase function Φ only. In the case of sufficiently smooth functions E and Φ, it is possible to go back from the complex β_n^m to the separate amplitude and phase parts of the pupil function. Using the above expansion for the exit pupil function in Eq.(2.20), we readily obtain the complex amplitude in the focal region with the aid of Eq.(2.47),

$$E_f(r,\phi,f) \propto \sum_{nm} 2i^m\ \beta_n^m\ V_n^m(r,f)\ \exp\{im\phi\}, \tag{5.2}$$

where the summation over the index m has to be carried out over both positive and negative values. The function $V_n^m(r,f)$ and its series expansion have been given in Eqs.(2.47)-(2.50).

The intensity I in the focal region is obtained by taking the squared modulus of E_f. In the case of relatively small aberrations and transmission non-uniformity, the intensity is approximated by

$$\begin{aligned} I(r,\phi,f) \approx & 4(\beta_0^0)^2\ |V_0^0(r,f)|^2 \\ & +8\beta_0^0 \sum_{n=0}^{\infty} \sum_{m=-\infty}^{+\infty} \Re\left\{i^{-m}\beta_n^{m\,*}\ V_0^0(r,f)\ V_n^{m\,*}(r,f)\exp[-im\phi]\right\}, \end{aligned} \tag{5.3}$$

where the term with $m = n = 0$ has to be omitted in the summation. The coefficient β_0^0 is chosen to be real and > 0; any nonzero phase of β_0^0 can be accounted for by a phase offset in the coefficients β_n^m with $n = m \neq 0$ as the absolute phase of the wavefront in the exit pupil is of no concern when measuring the image intensity. The approximation in Eq.(5.3) is justified when β_0^0 is the dominant coefficient in the Zernike expansion of the pupil function, thus allowing the deletion of any quadratic terms in β that do not contain a β_0^0 coefficient. In (5.3) the leading term is the aberration-free intensity pattern, for $f = 0$ equal to the Airy disc intensity.

Although the parametric representation of the pupil function with the aid of the β-coefficients is mathematically efficient and compact, the relationship between the amplitude and phase part of the pupil function and the structure of the intensity distribution in the focal volume tends to become obscure. For that reason, we temporarily resort to the more common harmonic representation with possibly complex β_c- and β_s-coefficients for the cosine and sine terms and the following relationship with the general β-coefficients

$$\beta_n^m = \frac{\beta_{n,c}^m}{2} - i\frac{\beta_{n,s}^m}{2}, \qquad \beta_n^{-m} = \frac{\beta_{n,c}^m}{2} + i\frac{\beta_{n,s}^m}{2}. \tag{5.4}$$

When the pupil function shows only weak phase aberration, one uses the approximate representation

$$P(\rho,\theta) \approx 1 + i\Phi(\rho,\theta) = 1 + i{\sum_{nm}}' R_n^m(\rho)\left[\alpha_{n,c}^m \cos\theta + \alpha_{n,s}^m \sin\theta\right]. \tag{5.5}$$

The hyphen on top of the summation sign indicates that the term with $n = m = 0$ should be excluded from the summation. The corresponding β-coefficients are given by

$$\beta_n^m = i\frac{\alpha_{n,c}^m}{2} + \frac{\alpha_{n,s}^m}{2}, \qquad \beta_n^{-m} = i\frac{\alpha_{n,c}^m}{2} - \frac{\alpha_{n,s}^m}{2},$$

and

$$\beta_{n,c}^m = i\alpha_{n,c}^m, \qquad \beta_{n,s}^m = i\alpha_{n,s}^m, \qquad \beta_0^0 = 1, \tag{5.6}$$

with the real coefficients $\alpha_{n,c}^m$ and $\alpha_{n,s}^m$ now specifically linked to the phase part of the pupil function. For this latter, frequently occurring practical case, Eq.(5.3) can be written out in detail to make visible the separate ϕ- and (r, f)-dependencies in the intensity distribution in the focal region. These dependencies will be exploited later in the retrieval scheme. After some manipulation, Eq.(5.3) is written according to

$$\begin{aligned} I(r,\phi,f) \approx \Psi_0^0 + {\sum_{n,m}}' \big\{ &\Re\left[\Psi_n^m(r,f)\right]\left(\Re[\beta_{n,c}^m]\cos m\phi + \Re[\beta_{n,s}^m]\sin m\phi\right) \\ &+\Im\left[\Psi_n^m(r,f)\right]\left(\Im[\beta_{n,c}^m]\cos m\phi + \Im[\beta_{n,s}^m]\sin m\phi\right)\big\}, \end{aligned} \tag{5.7}$$

where we have introduced the function

$$\Psi_n^m(r,f) = \gamma_m i^{-m} V_0^0(r,f) V_n^{m\,*}(r,f) \tag{5.8}$$

with $\gamma_0 = 4$ and $\gamma_m = 8$ for $m = 1, 2, ...$ With the phase-only pupil function and the coefficients according to Eq.(5.6) we find

$$I(r,\phi,f) \approx \Psi_0^0 + {\sum_{n,m}}' \Im\left[\Psi_n^m(r,f)\right]\left(\alpha_{n,c}^m \cos m\phi + \alpha_{n,}^m \sin m\phi\right). \tag{5.9}$$

This expression represents a set of equations in the unknown coefficients $\alpha_{n,c}^m$ and $\alpha_{n,s}^m$ of which a certain set is needed to represent in a sufficiently accurate way the phase part of the pupil function Φ. Various methods can be applied to solve for the unknown coefficients, like point-matching or a least-squares solution. Here, we present the approach that is based on the formation of a set of equations using inner products, see [Dirksen, Braat, Janssen, Juffermans (2003)], [van der Avoort, Braat, Dirksen, Janssen (2005)].

5.1.1 Solution method using inner products

To solve for the unknown aberration coefficients we first carry out a harmonic analysis of the intensity data in the focal volume by evaluating

$$\Xi_c^m(r,f) = \frac{1}{2\pi}\int_0^{2\pi} I(r,\phi,f)\cos m\phi \; d\phi, \tag{5.10}$$

and the corresponding sine-transform $\Xi_s^m(r,f)$. Carrying out the same harmonic analysis on the right-hand side of Eq.(5.9) we obtain the equations

$$\begin{aligned}\Xi_c^m(r,f) &= \delta_{mm}\Psi_0^0(r,f) + \frac{1}{2}\sum_n \alpha_{n,c}^m \Im\left[\Psi_n^m(r,f)\right] \\ \Xi_s^m(r,f) &= \frac{1}{2}\sum_n \alpha_{n,s}^m \Im\left[\Psi_n^m(r,f)\right],\end{aligned} \tag{5.11}$$

with δ_{mm} the Kronecker symbol. We define the (normalized) inner product of two functions Ψ_n^m by

$$(\Psi_1(r,f),\Psi_2(r,f)) = \frac{1}{2\pi R^2 F}\int_{0-F}^{R\,F} \Psi_1(r,f)\Psi_2^*(r,f)\; r dr df, \tag{5.12}$$

where the integration extends over the focal volume up to certain limits within which reliable data have been made available by measurement. We now apply the inner product operation to both sides of Eq.(5.12) and obtain

$$\begin{aligned}(\Xi_c^m, \Im[\Psi_{n'}^m]) &= \delta_{mm}\left(\Psi_0^0, \Im[\Psi_{n'}^m]\right) + \frac{1}{2}\sum_n \alpha_{n,c}^m \left(\Im[\Psi_n^m(r,f)], \Im[\Psi_{n'}^m]\right) \\ (\Xi_s^m, \Im[\Psi_{n'}^m]) &= \frac{1}{2}\sum_n \alpha_{n,s}^m \left(\Im[\Psi_n^m(r,f)], \Im[\Psi_{n'}^m]\right).\end{aligned} \tag{5.13}$$

By choosing a sufficiently large number of $n^{'}$ values, a preferably square system of equations is constructed for each specific value of the harmonic component m. The inner products on the right-hand side of Eq.(5.13) are calculated beforehand, a single time. The inner products on the left-hand side depend on the measurement data and have to be calculated anew for each system measurement. The solution of the system of equations is further facilitated by the fact that the matrix system of linear equations, built via the inner product method, is sparse with an almost perfect diagonal structure; this is because

of the 'almost' orthogonality properties of the elementary functions $\Psi_n^m(r, f)$ over the two-dimensional (r, f)-integration domain in the focal region.

5.1.2 Experimental results of aberration retrieval in the scalar approximation

In Fig. 5.1 we have sketched an experimental set-up to measure the lens quality of a high-resolution projection lens meant for optical lithography. The lens is illuminated via a tiny pinhole at the mask or reticle location using the standard illumination system of the lens. The pinhole image is captured in the high-numerical-aperture image space with the aid of a measuring objective that produces a magnified image on a high-density image sensor. The typical images produced by such a sensor are shown in Fig. 5.1 at the right. Through-focus images are successively captured by a defocusing of the measuring objective. A typical number of images to be treated in the total measurement series is

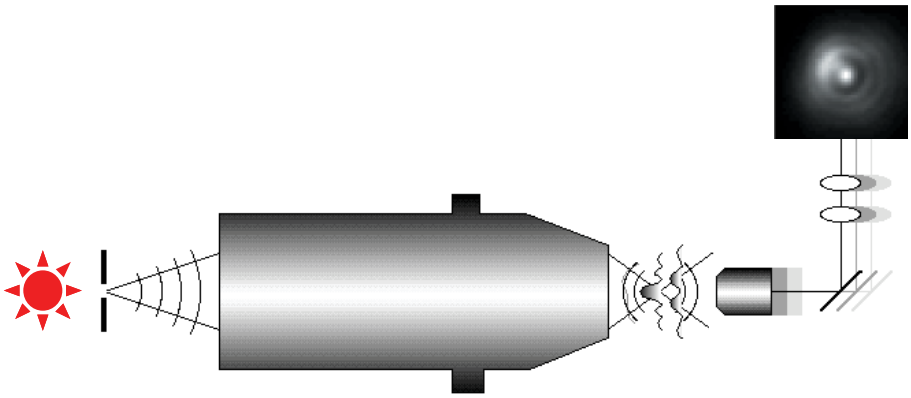

Fig. 5.1. Measurement set-up for quality assessment of a high-resolution projection lens. The intermediate image of the projection lens is captured by a measurement objective that produces a magnified image on the image sensor. The inserted picture at the right is a typical defocused image.

$2N + 1$, preferably symmetrically arranged around the optimum focal plane (see Fig. 5.2, upper row). The total excursion on either side of optimum focus

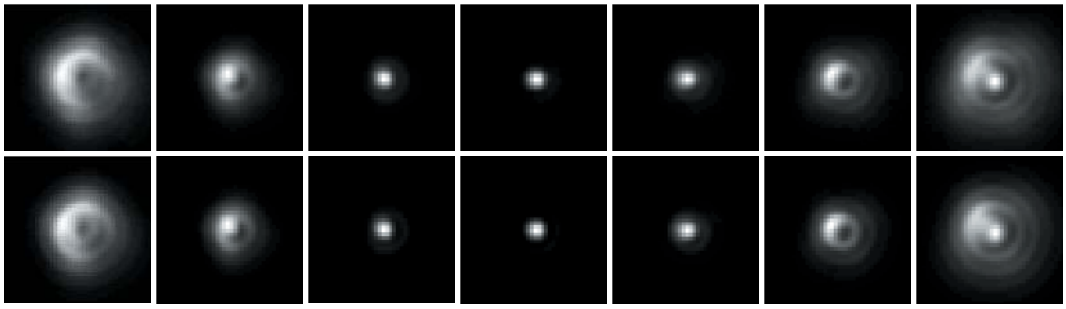

Fig. 5.2. A through-focus collection of point-spread functions captured by the image sensor. In this case, seven images, symmetrically arranged around best focus, have been recorded for aberration retrieval (upper row). The calculated result of the retrieval process is shown in the lower row of pictures where, for an easy comparison, the same pixel structure as during recording has been kept.

is of the order of 3 to 4 focal depths ($-2\pi \leq f \leq +2\pi$). The total amount of data captured from the $2N + 1$ through-focus images is used to construct an interpolated 3D-picture of the intensity distribution in the focal volume. The data are submitted to the harmonic decomposition of Eq.(5.10), yielding the cosine and sine components of the intensity variations over a circle of radius r at axial position f. The solution of the system of linear equations then yields the Zernike coefficients. The set of measured coefficients that resulted from the point-spread function analysis of Fig. 5.2, upper row, is shown in Fig. 5.3. The Zernike aberration coefficients have been arranged according to their

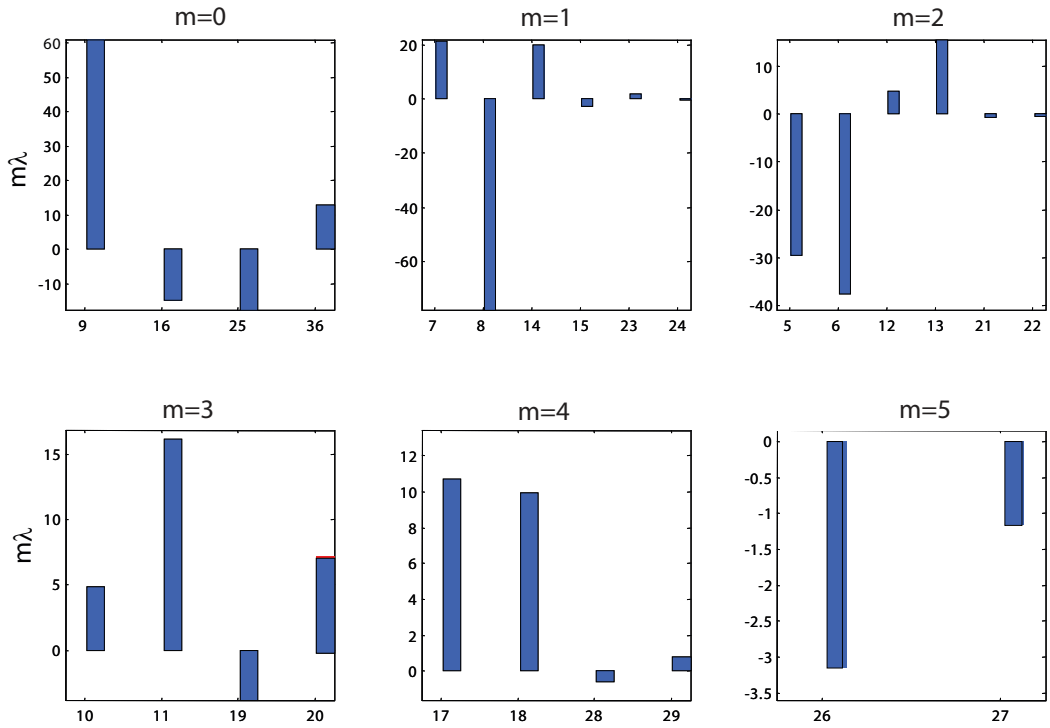

Fig. 5.3. A lens quality map obtained with the aid of the extended Nijboer Zernike method in terms of measured Zernike coefficients of the most frequently occurring aberrations. The measurement data are those of Fig. 5.2, upper row. The coefficients are expressed in units of milli-wavelength ($m\lambda$) of the light. The vertical scales of each order m has been adapted to the size of the aberration coefficients. Horizontal axis: Zernike polynomial index according to the Fringe Convention.

azimuthal order $m\theta$, ranging from 0 to 5. The numbering along the horizontal axis follows the Fringe Convention ordering of Zernike polynomials [Mahajan (1998)]. It is seen that the lowest order aberrations ($m \leq 3$) are dominating.

The stability of the retrieval process has been tested by adding numerical noise to the captured images. The amplitude of the noise was 10% of the top intensity, measured in the best-focus region. An example of such a series of perturbed images and their originals is given in Fig. 5.4. The retrieval process with the aid of the noisy images gave only minor deviations with respect

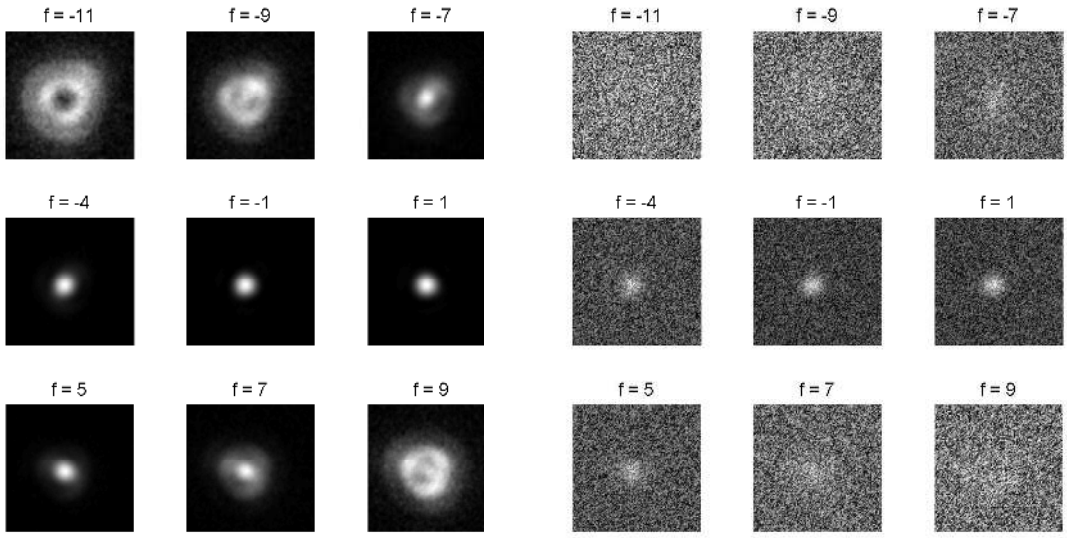

Fig. 5.4. A selection from a through-focus set of seventeen point-source images (left set) and the same pictures with noise artificially added to them (set of pictures to the right). The retrieval process applied to the noisy images shows only minor differences with respect to the original result.

to the original result. Maximum coefficient deviation remained below 10 $m\lambda$, resulting in an rms wavefront deviation of less than 3 $m\lambda$. This value would be too large for reliable quality assessment of high-resolution projection lenses for microlithography, but, fortunately, the image detection conditions are favorable there. The noisy pictures on the right are typical for photon-starved detection conditions. These are encountered in astronomical observation where aberration detection with 10 $m\lambda$ precision is generally more than sufficient.

Up to now, the through-focus images were experimentally obtained using an intermediate magnifying objective with its possible own optical defects. Although a separate assessment of such an objective is feasible, it is preferable to have a direct measurement of the point-spread function in the high-numerical-aperture image space. A method to obtain the intensity profile in the high-NA focal region is the printing of the point-source images in a thin layer of photoresist. To this goal, a point source is imitated by means of a tiny hole in the chromium layer of the object mask of the projection lens with a diameter of typically $0.5\lambda/s_0$, the diffraction unit at the mask side (see Fig. 5.5). For a certain exposure, the printed resist image will be developed up to a certain contour of equal intensity in the point-source image. By varying the exposure between successive displaced images in the resist layer, a whole range of equal intensity contours of the point-source images is obtained. By an analysis of the contour plot of each resist image for the complete series of defocused resist images at varying exposure, we can go back to the three-dimensional intensity

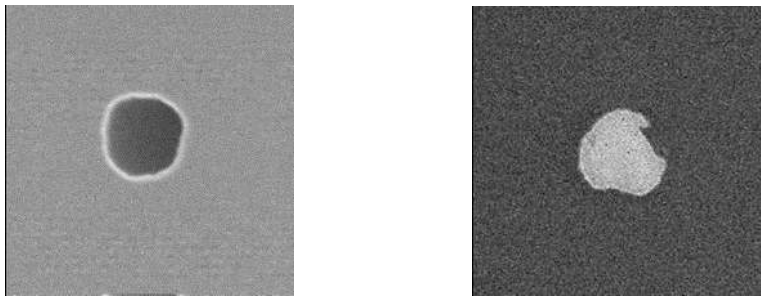

Fig. 5.5. A finite-size hole in the object mask chromium layer for a high-resolution projection lens (left picture) and its developed resist image in the focal region, obtained with a certain exposure dose (electron microscope images). The geometric measurement of a large number of such defocused and over- or under-exposed images yields the required three-dimensional intensity distribution in the focal region.

distribution in the focal volume. Here we should note that the contour plots carry with them intrinsically both the effect of using a finite hole size and the effect of image blur due to finite exposure. Fortunately, the ENZ-formalism is flexible enough to account for such effects, see for instance, [Dirksen, Braat, Janssen (2006)]. Below we show how we account for finite hole size effects, while in Subsection 5.1.3 image blur effects are handled. For a circular object hole, illuminated by a plane wave, the normalized far-field amplitude distribution is given by (scalar approximation),

$$
\begin{aligned}
I_n(\sin\alpha_f) &= \frac{2J_1\left(\pi D\sin\alpha_f/\lambda\right)}{\left(\pi D\sin\alpha_f/\lambda\right)} \\
&\approx 1-\frac{\pi^2D^2}{4\lambda^2}\sin^2\alpha_f \approx \exp\left\{-\frac{\pi^2D^2}{4\lambda^2}\sin^2\alpha_f\right\},
\end{aligned}
\tag{5.14}
$$

with α_f the polar far-field angle and $J_1(x)$ the first order Bessel function of the first kind [van der Avoort, Braat, Dirksen, Janssen (2005)]. In Eq.(5.14) we have also used, for sufficiently small values of the argument x, the approximation $2J_1(x)/x \approx 1 - x^2/4 \approx \exp\{-x^2/4\}$. The quadratically decreasing amplitude on the entrance pupil is accounted for in the diffraction integral of Eq.(2.20) by allowing the defocus parameter f to become complex according to $\tilde{f} = f - if_d$. If the numerical aperture at the object side is given by s_E, the matching of the far-field amplitude function at the rim of the entrance pupil ($\rho = 1$) yields the result

$$
\exp\{-i\tilde{f}\rho^2\} = \exp\{-if\rho^2\}\ \exp\left\{-\left(\frac{\pi^2D^2s_E^2}{4\lambda^2}\right)\rho^2\right\},
\tag{5.15}
$$

with the appropriate value of the amplitude factor f_d.

In [Dirksen, Braat, Janssen, Juffermans, Leeuwestein (2003)] a calibration of the retrieval method using resist images is discussed. A lithographic projection objective (NA=0.63, λ=193 nm) has been analyzed in its nominal setting and in some 'detuned settings'. The detuning operation allows to introduce well defined aberration increments by axial displacement, decentring or tilt of individual lens elements of the objective. In Fig. 5.6 retrieved lens data are

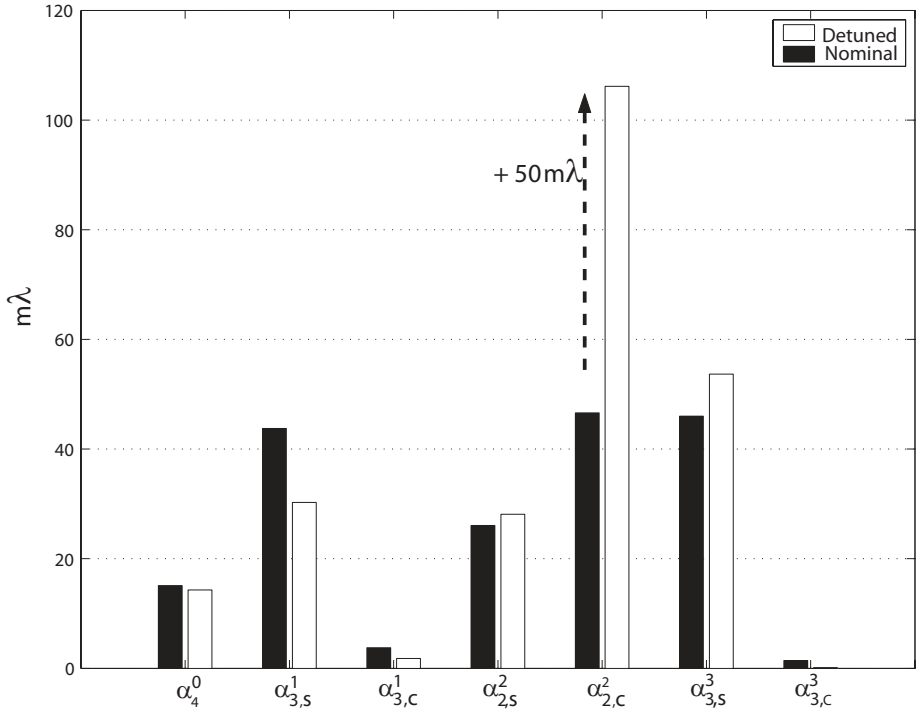

Fig. 5.6. Measurement results for a microlithographic projection objective (NA=0.63, λ=193 nm). The original aberrational data (lowest orders) of the objective are represented by the black bars (absolute values). The second set of white bars represents the measurement results for a detuned aberration setting of the objective with an increment of 50 $m\lambda$ for the astigmatic coefficient $\alpha^2_{2,c}$, respectively.

shown for the nominal lens (black bars) and a particular detuned state of the objective. The objective has been detuned so that the coefficient $\alpha^2_{2,c}$ for x-oriented astigmatism should have been increased by an amount of 50 $m\lambda$. The retrieved aberration coefficients of the detuned objective are represented by the white bars, showing the approximate increase by 50 $m\lambda$ for the $\alpha^2_{2,c}$-coefficient. The measurement spread $\Delta\alpha^m_{n,c/s}$ in the other fixed aberration coefficients is of the order of ± 10 $m\lambda$ and have to be imputed to small drifts in the objective itself and to the accuracy of the retrieval method. The short-term repeatability of the retrieved coefficients is of the order of a few $m\lambda$.

An analysis of the convergence and the robustness of the through-focus retrieval method using the extended Nijboer-Zernike theory has been carried

out in [van der Avoort, Braat, Dirksen, Janssen (2005)]. In this analysis, an approximated scalar retrieval scheme at high numerical aperture values was also given. It was found, as a rule of thumb, that the values of the wavefront coefficients $|\alpha_n^m|$ should not collectively give rise to a variance of the phase aberration larger than 0.4, equivalent to an rms wavefront aberration of less than $\lambda/10$. This corresponds to a Strehl ratio of 0.60, well outside the 'just' diffraction-limited regime. To achieve good retrieval results for these larger aberration coefficients, it is necessary to extend the linearized retrieval scheme with a predictor-corrector iteration method, [van der Avoort, Braat, Dirksen, Janssen (2005)]. We will discuss this iteration method in the next section on the vector diffraction case. In the same reference, the addition of zero-average detection noise in the captured images has been simulated and the resulting coefficients have been compared with the original values for defocus, wavefront tilt, coma and astigmatism. In Table 5.1.2 we reproduce these simulated data and it can be concluded that a signal-to-noise ratio as small as 10 is still capable of yielding retrieval errors not larger than 5%. It has been observed that the detection noise should have zero mean. If this not the case, serious off-sets in the retrieved coefficients can occur.

indices		input values	retrieved values		
n	m		SNR=∞	SNR=100	SNR=10
2	0	0.3000	0.3000	0.2996	0.2989
1	1	0.1000	0.1000	0.1003	0.1027
3	1	0.4000	0.4000	0.4002	0.4082
2	2	0.2000	0.2000	0.1991	0.2087

Table 5.1
Simulation of detection noise (zero mean) and its influence on the values of some lower order retrieved aberration coefficients.

5.1.3 Refinements of the scalar retrieval model

The influence of the finite object pinhole size is an example of how to extend the basic imaging and retrieval model to real experimental conditions. In this subsection we present some refinements of the basic model that allow a broader range of application of the retrieval method. With these refinements one can treat images that are affected by focus or in-plane noise during acquisition, by blurring due to chromatic aberration of an imaging system or by lateral blurring due to image sensor digitization or photo-resist diffusion effects. These are typical 'blurring' effects that arise in the treatment of point-source images

produced by high-resolution projection lenses. For these lenses, the quality assessment has to be carried out with utmost accuracy and such a refined model is mandatory. As a side-effect, such a retrieval process also allows to establish the magnitude of the parameters that cause the blurring, for instance the photo-resist diffusion parameters in the case of image capture via developed photo-resist images in a high-NA space.

The exposure in the focal region, affected by in-plane or axial position noise, depends on the statistics of the movements. Following [Dirksen, Braat, Janssen (2006)], it is customary to adopt Gaussian statistics for the movements with a probability density function given by

$$\Delta_x(t) = \frac{1}{\sqrt{2\pi}\sigma_x} \exp\left(-\frac{\Delta_x^2(t)}{2\sigma_x^2}\right), \tag{5.16}$$

with σ_x the standard deviation of the movement in the x-direction. Comparable expressions hold for the statistical excursions in the y- and f-direction with standard deviations of σ_y and σ_f, respectively. The incremental exposure in a resist layer or the time-integrated intensity recorded by a sufficiently small detector pixel is given by

$$dE_r(x, y, f) = I\left\{x - \Delta_x(t), y - \Delta_y(t), f - \Delta_f(t)\right\} dt. \tag{5.17}$$

In the case of a sufficiently small standard deviation value σ_r with respect to the full width at half maximum (FWHM) of the lateral intensity profile and a sufficiently small value of σ_f of the axial movements with respect to, for instance, the focal depth of the imaging system, a Taylor expansion of the intensity distribution can be applied. The total exposure, integrated over sufficiently long time is then approximated, at least up to second order, by

$$\begin{aligned} E_r(r, f) \approx \int_{-\infty}^{+\infty} \Big[& I(r, f) - \Delta_x(t)\frac{\partial I}{\partial x} - \Delta_y(t)\frac{\partial I}{\partial y} - \Delta_f(t)\frac{\partial I}{\partial f} \\ & + \frac{1}{2}\Delta_x^2(t)\frac{\partial^2 I}{\partial x^2} + \frac{1}{2}\Delta_y^2(t)\frac{\partial^2 I}{\partial y^2} + \frac{1}{2}\Delta_f^2(t)\frac{\partial^2 I}{\partial f^2} \\ & + \Delta_x(t)\Delta_y(t)\frac{\partial^2 I}{\partial x \partial y} + \Delta_x(t)\Delta_f(t)\frac{\partial^2 I}{\partial x \partial f} \\ & + \Delta_y(t)\Delta_f(t)\frac{\partial^2 I}{\partial y \partial f} + \cdots \Big] dt. \end{aligned} \tag{5.18}$$

In what follows, the expressions are simplified by considering the case that the intensity distribution possesses radial symmetry and that equally large statistical x- and y-movements are present (isotropic case) with each a standard deviation σ_m. This limitation to the radially symmetric case is adequate in most practical cases. In the radially symmetric case, one can easily introduce a further effect that is very important in resist imaging, the chemical diffusion of the exposure profile in the resist layer. This chemical blurring of the exposure profile occurs partly during the exposure and development process (latent image formation) but it is most pronounced during the so-called post-exposure bake. It can be adequately incorporated in a total radial standard deviation given by

$$\sigma_r^2 = \sigma_m^2 + 2Dt_b, \tag{5.19}$$

where $2Dt_b$ is the Fickian diffusion length, the product of the acid diffusion coefficient D and the baking time t_b [Lavery, Vogt, Prabhu, Lin, Wu (2006)]. The integration of Eq.(5.18), formally over the total time of resist exposure up to the end of the post-exposure bake, gives rise to

$$E_r(r,f) = E_0(r,f) + \frac{t_E\sigma_r^2}{2}\left\{\frac{\partial^2}{\partial r^2} + \frac{1}{r}\,\frac{\partial}{\partial r}\right\} I(r,f) + \frac{t_E\sigma_f^2}{2}\,\frac{\partial^2 I(r,f)}{\partial f^2}, \tag{5.20}$$

all other terms yielding zero in the radially symmetric case due to statistical averaging. The leading term $E_0(r,f) = I(r,f)t_E$ is called the static exposure term, with t_E a sufficiently long exposure time so that the statistical averaging effectively has taken place.

For the evaluation of the first and second derivative of the function $I(r,f)$, it is sufficient to use the approximated expression of Eq.(5.3) with $m = 0$ in the summation term. In [Dirksen, Braat, Janssen (2006)], the derivatives of the products $V_0^0(r,f)V_{2n}^{0\,*}(r,f)$ have been given. To cover still larger blurring effects, an expansion term of the fourth order has been included in Eq.(5.18). This fourth order Taylor term, in general contributing

$$\frac{t_E\sigma_r^4}{8}\left(\frac{\partial^2}{\partial x^2} + \frac{\partial^2}{\partial y^2}\right)^2 I(r,f) \tag{5.21}$$

to the exposure of Eq.(5.20), is then restricted in this reference to the leading term of $I(r,f)$, the aberration-free term $|V_0^0(r,f)|^2$.

In Fig. 5.7 three physical causes for blurring of the point-spread function

have been presented, all three for a radially symmetric case. The contour plots

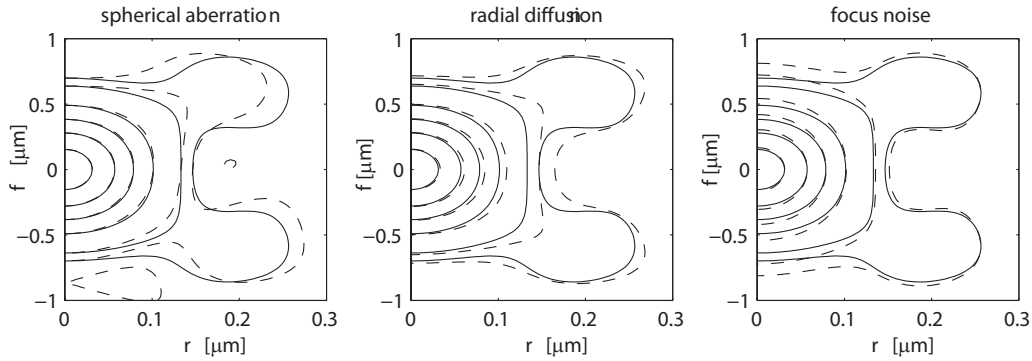

Fig. 5.7. Contour plots for typical blur effects (dashed lines) in a point-spread function (radial symmetry). The ideal point-spread function contours have been represented with full lines. The left graph has been obtained by introducing spherical aberration in the imaging system ($\alpha_4^0 = 75\ m\lambda$). In the central graph, a radial blur (chemical diffusion in resist pattern) has been applied, $\sigma_r = 30\ nm$. The graph on the right presents the effect of an axial blur due to focus noise ($\sigma_f = 150\ nm$.

apply to a point-spread function produced by an objective with an NA of 0.63, operating at a wavelength of 193 nm (Deep UV illumination). The scales are in absolute measure, although different along the radial and axial axes. In the left graph, an (r, f) contour plot (dashed) is given for a point-spread function suffering from spherical aberration. The Zernike coefficient α_4^0 of the wavefront aberration equals 75 $m\lambda$, giving rise to an rms wavefront aberration of 33 $m\lambda$, well within the diffraction limit of 71 $m\lambda$. The drawn curves applies to the aberration-free case. The typical asymmetric behavior of the point-spread function with respect to the plane $f = 0$ is well visible in the figure. A blurring of comparable magnitude, but now with focus symmetry, is presented in the middle graph (dashed contours). In this case, the exposure profile in the recording resist layer has introduced a radial diffusion of the exposure pattern of 30 nm rms value (σ_r); the axial blur is very small. Finally, in the right figure, the point-spread function was subjected to a focus blurring with an rms value of 150 nm, to be compared with the approximate focal depth of 240 nm. In the case of focus noise, the symmetry around focus is also preserved, the blurring being mainly in the axial direction.

Further refinements in the scalar retrieval method are possible to account for other experimental conditions. Instead of mechanical focus noise, an axial blur can also be produced by axial chromatism of the imaging system. As it was mentioned earlier, in some applications broadband light has to be used. This leads to a blurring of the incoherently superimposed monochromatic point-spread functions by the scaling of the diffraction unit λ/NA.

The foregoing section has extensively discussed the retrieval mechanism for the complex pupil function using the scalar imaging model. In this section we replace the scalar through-focus intensity distribution by its vector equivalent and then apply this new expression to basically the same retrieval procedure. The complications that arise in the vector imaging model stem from the influence of the state of polarization in the exit pupil on the intensity distribution in the focal region, see Section 3. In most cases, the state of polarization in the exit pupil is uniquely determined by the state of polarization in the entrance pupil. This direct relationship disappears when the optical system introduces birefringence. The vector imaging model is capable to keep track of this birefringence and, using more than one set of through-focus images with different states of polarization in the entrance pupil, it is even possible to retrieve also the birefringence properties of the system. We first present a linearized expression for the intensity distribution in the focal volume in the absence of birefringence and use this expression in a vector diffraction retrieval scheme. The extension to retrieval in the presence of birefringence is addressed further on in this section but will not be worked out in full detail.

5.2.1 Approximated linearized intensity distribution in the focal volume

In this section we use the expressions for the cartesian electric field vectors in the focal region of a high-NA imaging system in the case of a point source object. The field in the entrance pupil is described by a coherent superposition of two orthogonally polarized linear states of polarization according to $\mathbf{E} = (p_x, p_y, 0)A_0$ where p_x and p_y generally are complex numbers and A_0 is the constant amplitude factor. The influence of the non-perfect high-numerical-aperture imaging system is the introduction of wavefront deformation and transmission changes, on top of an intrinsic amplitude distribution on the exit pupil sphere that is different for each cartesian field component and that has been described in [Wolf (1959)] and [Richards, Wolf (1959)]. The field in the focal region is obtained by calculating three basic integrals. In what follows, the behavior of an aberrated optical system is described by an expansion of the complex lens transmission function in terms of Zernike polynomials with complex coefficients that are supposed to be identical for each polarization state. We suppose that each vector component of the electric field in the exit pupil has to be multiplied by the complex pupil transmission function of Eq.(2.63)

with the Zernike coefficients $\beta_{n,x}^m = \beta_{n,y}^m = \beta_n^m$ yielding a pupil function

$$P(\rho,\theta) = \sum_{n,m} \beta_n^m R_n^{|m|}(\rho) \exp(im\theta). \tag{5.22}$$

As usually, we suppose that β_0^0 is the leading term; this will be the case for optical systems that are close to the diffraction limit. Using the extended Nijboer-Zernike theory, the complex field vectors in the focal region are now calculated using Eq.(2.64) with the modified integrals $V_{n,-2}^m$, $V_{n,-1}^m$, $V_{n,0}^m$, $V_{n,+1}^m$, $V_{n,+2}^m$ with the indices (n,m) pertaining to the Zernike polynomial expansion on the exit pupil function. The evaluation of these integrals is possible using the analytic schemes given in Appendix D.

The general expression for the energy density has been given in Eq.(3.8). An important reduction in complexity is obtained for an isotropic imaging system with the pupil function defined by Eq.(5.22) above and the resulting expression is found in Eq.(3.12). The expression for the energy density that will be used in the retrieval scheme allows a further approximation that was also used in the scalar case by exploiting the fact that β_0^0 is the leading term in the pupil function expansion. The expression for a general term $G_{k,l}$ of Eq.(3.12)is then given by

$$\begin{aligned} G_{k,l}(\beta,\beta) = & \frac{\beta_0^0}{2} \exp\{i(k-l)\phi\} \quad \times \\ & \sum_{\nu} \sum_{\mu} (2-\delta_{\nu\mu}) \left\{ \beta_\nu^{\mu *} \Psi_{\nu;k,l}^{\mu *}(r,f) \exp(-i\mu\phi) + + \beta_\nu^{\mu} \Psi_{\nu;l,k}^{\mu}(r,f) \exp(+i\mu\phi) \right\}, \end{aligned} \tag{5.23}$$

In this expression, μ assumes both positive and negative values and $\delta_{\nu\mu}$ stands for the Kronecker symbol. We also introduced the shorthand notation

$$\Psi_{\nu;k,l}^{\mu}(r,f) = (+i)^{\mu} V_{0,k}^{0*}(r,f) V_{\nu,l}^{\mu}(r,f) \; . \tag{5.24}$$

5.2.2 Aberration retrieval scheme for the vector diffraction case

Like in the scalar case, the retrieval scheme for obtaining the complex pupil function is based on a Fourier analysis of the measured and the analytically proposed intensity data. In contrast with the analysis of Subsection 5.1 where we have dealt with separate expressions for the cosine and sine harmonic components, we will use from now on the complex exponentials $\exp(im\theta)$ and the complex β-coefficients with m-indices running from $-\infty$ to $+\infty$. The harmonic dependence in the focal region is represented by complex exponentials

$\exp(im\phi)$. The Fourier decomposition is carried out with respect to the harmonics in the through-focus intensity distribution. To this goal we evaluate

$$\Psi^m_{an}(r,f) = \frac{1}{2\pi}\int_{-\pi}^{+\pi} \langle w_e(r,\phi,f)\rangle \exp(im\phi)d\phi \;, \tag{5.25}$$

with the subscript (an) referring to the analytically calculated intensity distribution. A comparable operation is performed on the measured intensity data, yielding functions $\Psi^m(r,f)$.

The analytic energy density distribution of Eq.(3.12) is used to calculate Ψ^m_{an} in combination with the linearized G_{kl}-functions, and, after some lengthy manipulation, we obtain (see Appendix A of [Braat, Dirksen, Janssen, van de Nes, van Haver (2005)] and [van Haver, Braat, Dirksen, Janssen (2006)])

$$\begin{aligned}
\Psi^m_{an}(r,f) \approx \frac{\beta^0_0}{2}\sum_\nu \;\Bigg\{ & \\
&\beta^{m*}_\nu(2-\delta_{\nu,m})\Bigg[\Psi^{m*}_{\nu;0,0} + s_0^2\Bigg\{\left(\Psi^{m*}_{\nu;1,1}+\Psi^{m*}_{\nu;-1,-1}\right) + \frac{s_0^2}{2}\left(\Psi^{m*}_{\nu;2,2}+\Psi^{m*}_{\nu;-2,-2}\right) \\
&\quad -2\Im(p_x p_y^*)\left[\left(\Psi^{m*}_{\nu;1,1}-\Psi^{m*}_{\nu;-1,-1}\right) + \frac{s_0^2}{2}\left(\Psi^{m*}_{\nu;2,2}-\Psi^{m*}_{\nu;-2,-2}\right)\right]\Bigg\}\Bigg] \\
&+\beta^{-m}_\nu(2-\delta_{\nu,m})\Bigg[\Psi^{-m}_{\nu;0,0} + s_0^2\Bigg\{\left(\Psi^{-m}_{\nu;1,1}+\Psi^{-m}_{\nu;-1,-1}\right) + \frac{s_0^2}{2}\left(\Psi^{-m}_{\nu;2,2}+\Psi^{-m}_{\nu;-2,-2}\right) \\
&\quad -2\Im(p_x p_y^*)\left[\left(\Psi^{-m}_{\nu;1,1}-\Psi^{-m}_{\nu;-1,-1}\right) + \frac{s_0^2}{2}\left(\Psi^{-m}_{\nu;2,2}-\Psi^{-m}_{\nu;-2,-2}\right)\right]\Bigg\}\Bigg] \\
&+\beta^{(m-2)*}_\nu\left[|p_x|^2-|p_y|^2+2i\Re(p_x p_y^*)\right](2-\delta_{\nu,m-2}) \quad \times \\
&\qquad \frac{s_0^2}{2}\left\{\Psi^{(m-2)*}_{\nu;-2,0}+\Psi^{(m-2)*}_{\nu;0,2}-2\Psi^{(m-2)*}_{\nu;-1,+1}\right\} \\
&+\beta^{(m+2)*}_\nu\left[|p_x|^2-|p_y|^2-2i\Re(p_x p_y^*)\right](2-\delta_{\nu,m+2}) \quad \times \\
&\qquad \frac{s_0^2}{2}\left\{\Psi^{(m+2)*}_{\nu;2,0}+\Psi^{(m+2)*}_{\nu;0,-2}-2\Psi^{(m+2)*}_{\nu;+1,-1}\right\} \\
&+\beta^{(-m-2)}_\nu\left[|p_x|^2-|p_y|^2-2i\Re(p_x p_y^*)\right](2-\delta_{\nu,-m-2}) \quad \times \\
&\qquad \frac{s_0^2}{2}\left\{\Psi^{(-m-2)}_{\nu;-2,0}+\Psi^{(-m-2)}_{\nu;0,2}-2\Psi^{(-m-2)}_{\nu;-1,+1}\right\} \\
&+\beta^{(-m+2)}_\nu\left[|p_x|^2-|p_y|^2+2i\Re(p_x p_y^*)\right](2-\delta_{\nu,-m+2}) \quad \times
\end{aligned}$$

$$\frac{s_0^2}{2}\left\{\Psi_{\nu;2,0}^{(-m+2)} + \Psi_{\nu;0,-2}^{(-m+2)} - 2\Psi_{\nu;+1,-1}^{(-m+2)}\right\}\Bigg\}\Bigg\}. \quad (5.26)$$

We recall that the expression above is not exact but applies to the linearized approximation of the $G_{k,l}$-functions. The equations to be solved now read

$$\Psi^m(r,f) \approx \Psi_{an}^m(r,f)\ , \quad (5.27)$$

to be solved for each separate m-value. In practice, we merge these equations into one large system of linearized equations. Like in the scalar case, the practical solution procedure consists of taking inner products on both sides with the functions $\Psi_{n;k,l}^m(r,f)$ and to solve this new system of equations. This more global method replaces the direct approach that would try to find the solution with the optimum match for each point in the (r,f)-cross-section of the focal volume. The inner products are defined by Eq.(5.12), in line with the scalar retrieval method. In the vector retrieval case, the functions $\Psi^m(r,f)$, $\Psi_{an}^m(r,f)$ and $\Psi_{n;k,l}^m(r,f)$ are now all complex; the integration limits are determined by the axial and lateral range of the collected intensity data.

5.3 Retrieval examples for high-NA systems

In this subsection we present an example that shows the inadequacy of a retrieval method based on scalar diffraction theory when applied to a high-NA imaging system. Secondly, we show the ranges of aberration and transmission defects that can be handled by the linearized system of equations based on Eq.(5.27). Subsequently, the error is evaluated that is introduced in the retrieval process when system parameters, such as the numerical aperture and incident polarization, are not exactly known. We then present a simulated retrieval example performed in such a way that it closely resembles the treatment of experimental data. Experimental intensity data are analyzed for a high numerical aperture projection lens illuminated by a source with a partial degree of polarization equal to zero.

5.3.1 Retrieval of a high-NA system assuming scalar conditions

To underline the necessity of applying the full vectorial case when assessing imaging systems with a high numerical aperture, we analyze the following retrieval operation on simulated data. A through-focus intensity distribution is

constructed from five axially displaced through-focus images with focus parameter values $f = -2, -1, 0, 1, 2$, in dimensionless focal units according to the definition in Eq.(2.31). The intensity distribution is calculated for an aberration-free optical system with a numerical aperture of 0.95, whose entrance pupil is illuminated by a linearly polarized wave with the plane of polarization parallel to the x-axis. We apply the forward-calculation scheme using the expressions for the electric field components of Eq.(2.65). The high-NA data set acquired

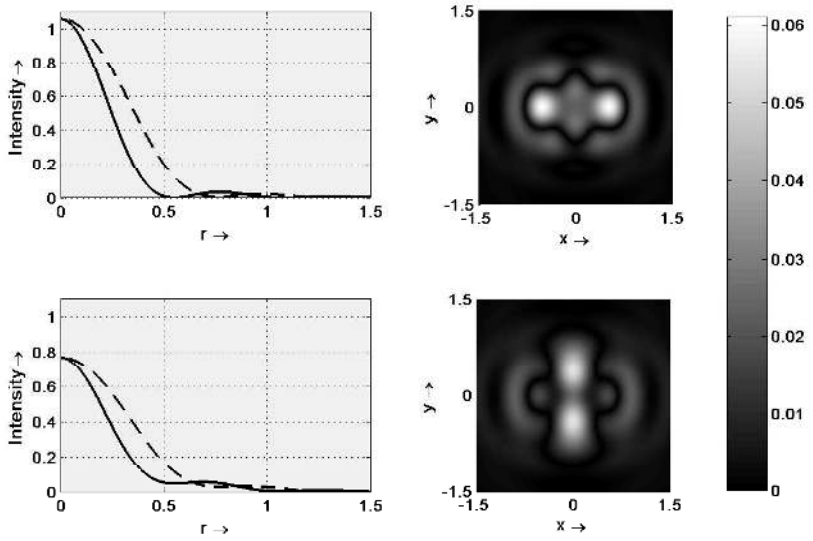

Fig. 5.8. In-focus ($f = 0$) intensities as a function of the positive x- and y-coordinate (upper left graph, dashed and solid line, respectively). Right upper graph: grey-scale plot in the (x, y)-plane of the difference between the aberration-free intensity distribution ($NA = 0.95$, x-polarization) and its retrieved version based on a scalar model. In the second row the same information is presented for an out-of-focus position with $f = -2$.

through this operation is then analyzed using the scalar version of the retrieval scheme. This scheme neglects the vector character of the optical field but takes into account the exact phase departure of a defocused wave at high numerical aperture as it is done in Eq.(2.33). This gives rise to the set of retrieved β-coefficients that can be found in the column on the right of Table 5.2. The fit imposed by this limited set of β-coefficients is remarkably good as can be derived from Fig. 5.8; the maximum intensity deviations are of the order of 5%. Nevertheless, on comparing the β-coefficients obtained through the scalar retrieval operation with the actual β's (aberration-free case) used for the simulation, we observe a very poor correspondence, see Fig. 5.9. Although it seems that the scalar model with high-NA focus adaptation is able to fit a high-NA intensity distribution, the retrieved β-coefficients do not have a physical relevance. We observe that the β_2^0-, β_2^2- and β_2^{-2}-coefficients are all real and thus affect the transmission part of the pupil function. This amplitude

modulation, composed of a circularly symmetric part and a contribution with a $\cos 2\theta$-dependence, is necessary to describe the strongly elliptical energy density distribution in the focal region at high values of the numerical aperture. Note that the strong amplitude deformation even includes a region in the pupil

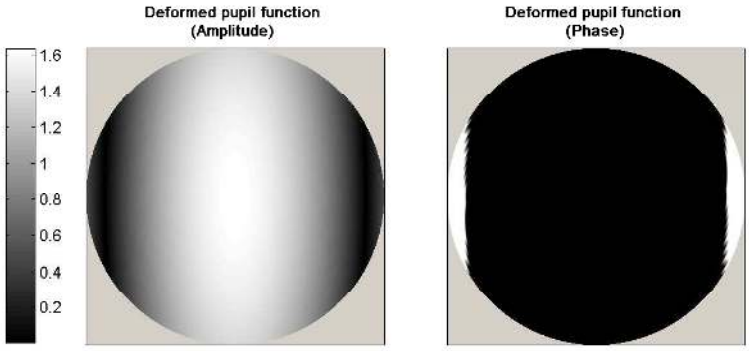

Fig. 5.9. The strongly deformed pupil function resulting from a scalar retrieval method applied to an imaging system with $NA = 0.95$. Left graph: false color plot of the modulus of the retrieved pupil function. Right graph: phase of the pupil function (black region with zero phase, white region with a phase of π. The figure shows that the outer part of the pupil function in the x-direction assumes negative values.

where the amplitude is negative, see Fig. 5.9. This effectively means that this region is subjected to a phase shift of π.

This example with simulated data shows that the β-coefficients that are found when applying scalar theory to intensity distributions governed by the vectorial model, do not have direct physical relevance and no longer give a correct description of the system under consideration. Physically relevant β-coefficients for a high-NA optical system can only be expected if the full vectorial case is applied at the retrieval stage. The high-NA retrieval formalism was introduced above and it will now be further examined using both simulated data and a set of experimentally obtained data.

	Input	Retrieved
β_0^0	1.000	1.038
β_2^0	0.000	−0.593
β_2^{-2}	0.000	−0.466
β_2^2	0.000	−0.466

Table 5.2
Comparison between the initial and the retrieved β-coefficients when retrieving a simulated aberration-free intensity distribution ($NA = 0.95$, x-polarization) using the scalar retrieval scheme.

5.3.2 Accuracy of the high-numerical-aperture retrieval scheme

When applying the retrieval scheme for the high numerical aperture case, the retrieved β-coefficients are generally not exact because of our approximated version of the Ψ_{an}^{m}-functions according to Eq.(5.26). An exception is the aberration-free system where the retrieved β-coefficients are exact, giving the trivial solution $\beta_0^0 = 1$ and all other β_n^m equal to zero. When aberrations are present in the system, described by additional β-coefficients with n or $m \neq 0$, the retrieved β_n^m-coefficients will show residual errors originating from the linearization applied in Eq.(5.26).

An impression of the magnitude of the errors in the retrieved β-coefficients is obtained by performing the following simulations. Starting from a perfect (aberration-free) system, represented by a single β-coefficient, $\beta_0^0 = 1$, we introduce one additional non-zero β-coefficient, for instance $\beta_2^2 \neq 0$. Next, this pair of β-coefficients is used to simulate a through-focus intensity distribution that serves as input for the retrieval operation. The retrieval process will now generate an estimate for this pair of β-coefficients describing the system. These estimates, which we shall denote as β', are not exact and include a certain error. The above process having been repeated at ever increasing size of β_2^2 leads to the error behavior in the set of retrieved β' shown in Fig. 5.10. In the figure, the maximum error in the set of retrieved β-coefficients is plotted as a function of the magnitude of the β_2^2-coefficient that was used as an input to the simulation. Figure 5.10 indicates a quadratic relation between the

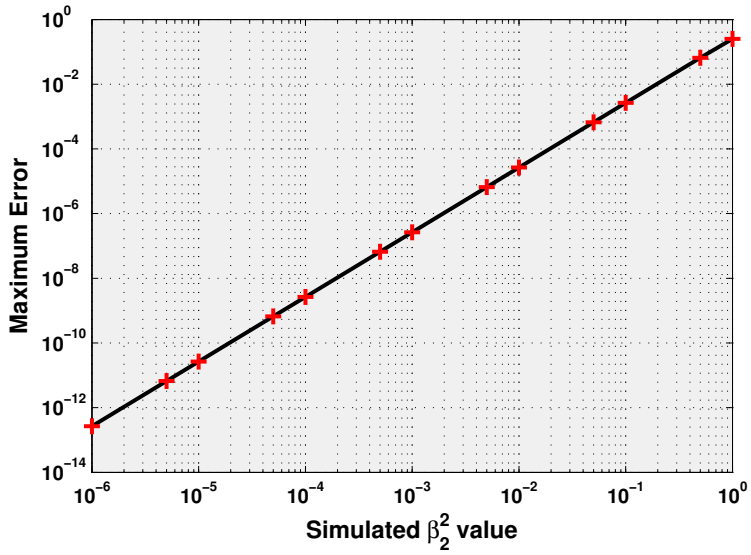

Fig. 5.10. Plot of the maximum error present in the retrieved β'-coefficients as a function of the magnitude of the β_2^2-coefficient that served as input. The imaging system was free of any other defect; incident light x-polarized, NA= 0.95.

maximum observed error in the retrieved β'-coefficients and the input value β_2^2. This has to be expected, as we omit exactly the cross-terms depending on $\beta_n^m \beta_{n'}^{m'}$ in the linearized expression for $G_{k,l}$, see Eq. (5.23). The linearized retrieval method is very accurate for well-corrected optical systems ($\beta \leq 10^{-1}$). On the other hand, if we have a system influenced by larger aberrations (β of the order of 1), the errors present in the retrieved β-coefficients will be of the same order, which means that the quality of the retrieval method is poor. Fortunately, iterative schemes can be applied to the solution of linearized systems of equations, updating the system at each iteration step with an estimate of the ignored quadratic term. Such a correction scheme can be applied to the retrieval method and it produces strongly improved retrieval results to the extent that the retrieved β-coefficients converge to their correct values. The correction scheme of the "predictor-corrector" type, is discussed in more detail below.

5.3.3 Predictor-corrector method for improved system assessment

A wider range of aberrated pupil functions can be handled once we use the so-called predictor-corrector extension when solving the linearized equations. It leads to a better assessment of the quality of imaging systems over a range that substantially exceeds the classical diffraction limit (Strehl ratio ≥ 0.80). Although the final quality of high-resolution imaging systems should be well within this limit, it is well known that during the quality-tuning stage in the manufacturing process these systems can show appreciable deviations from the diffraction limit. The medium to large aberrations that can be expected during this stage should be accessible for an assessment method of more general use. To improve scalar retrieval results, a so-called predictor-corrector iteration scheme was already proposed and thoroughly tested, see [van der Avoort, Braat, Dirksen, Janssen (2005)]. An equivalent iterative procedure has been devised for the high-numerical-aperture case. It is discussed in detail in Appendix E.

In Fig. 5.11 the results are shown of high-NA retrieval using the predictor-corrector procedure. The optical system suffers from astigmatism in the x-direction ($\beta_0^0 = 1$, $\beta_2^2 = \beta_2^{-2} = 0.5i$). The numerical aperture is 0.95, the incident light is polarized in the x-direction. One observes a steady decrease of the error present in the retrieval result with the number of iterations. For the synthetic data used in this example, the error eventually attains the typical machine precision of the calculation software, equal to $\approx 10^{-15}$ in the case of Fig. 5.11. Note that accuracies, customary for practical applications and typi-

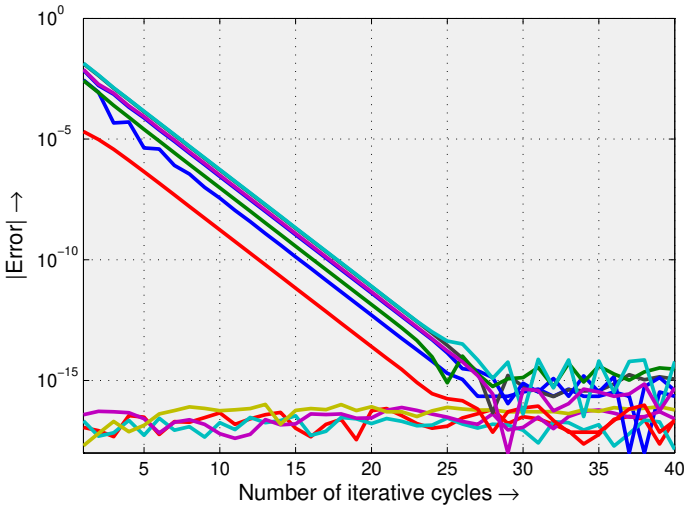

Fig. 5.11. A plot of the residual errors in the retrieved β-values versus the number of iterative steps taken in the predictor-corrector procedure. The colours pertain to various aberration terms that were either initially present or that were erroneously detected at the start of the iterative retrieval process. The end value is determined by machine precision.

cally of the order of a few times 10^{-3}, are reached within less than 10 cycles.

For real experimental data, when numerous inaccuracies and perturbations such as noise are inevitable, the attainable precision will be limited. Still in that case, the residual errors in the retrieved β-values, obtained through the predictor-corrector procedure, will be small and of the same (or lower) order of magnitude than the noise present in the data. We have observed such a performance for aberration values that can be as large as twice the diffraction-limit, up to an rms wavefront deviation of 0.15λ. The influence of noise is discussed further on in this section; we now first investigate the effect on the retrieval quality of systematic errors in the parameters that describe the optical imaging system.

5.3.4 Systematic errors and their influence on the quality assessment

One of the possible complications encountered when going from simulated data to experimental data obtained from a real optical system, is that certain system parameters are not exactly known. The investigation of the effect on the retrieval quality has been carried out in the case that incorrect values of the numerical aperture and the azimuth of the linear state of polarization were assumed [van Haver, Braat, Dirksen, Janssen (2006)]. To this goal, a through-focus intensity distribution according to the β-values of Table 5.3 was synthesized. Next, the system defined in Table 5.3 is subjected to the pupil function retrieval procedure based on the vector diffraction model. A range of

Input values β-coefficients					
β_0^0	β_2^0	β_3^{-1}	β_3^1	β_2^{-2}	β_2^2
1.0000	$0.0200i$	$0.0500i$	$0.0500i$	$0.0100i$	$0.0100i$

Table 5.3
Set of β-coefficients used for the description of the field on the exit pupil sphere of the imaging system under consideration ($NA = 0.95$).

values for the numerical aperture was assumed, ranging from very low to the extreme value of unity. The error in the assessment of the imaging system is monitored by recording several β-coefficients and the results are given in Fig. 5.12. One observes that the residual error in all β-coefficients is minimal for the correct value of the numerical aperture. This feature not only enables a tuning of the retrieval process to the exact value of the numerical aperture, but also suggests a procedure to accurately determine the numerical aperture of an unknown system. A comparable simulation is presented in [van Haver, Braat,

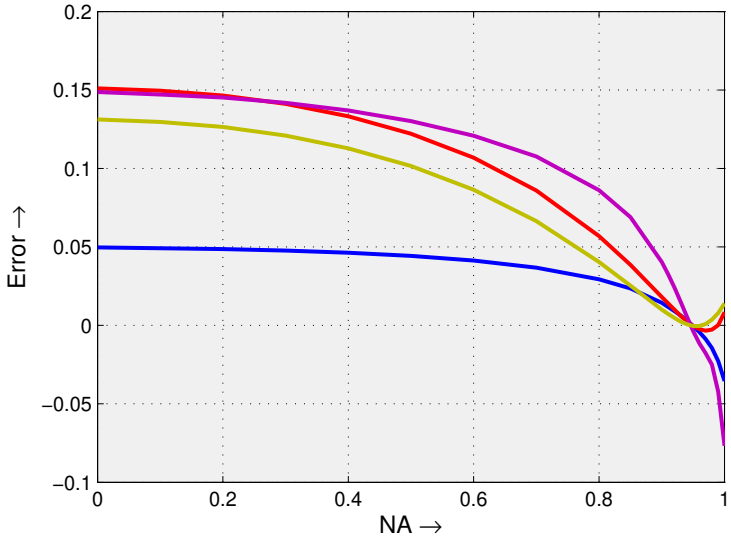

Fig. 5.12. The error present in some relevant β-coefficients when retrieving the system defined in Table 5.3 while assuming different values for the numerical aperture NA. The colours point to typical aberration coefficients; the residual errors for all aberrations are smallest at the correct value of the numerical aperture s_0.

Dirksen, Janssen (2006)], now regarding an erroneous input of the azimuth of the linear state of polarization in the entrance pupil of the optical system; the numerical aperture was fixed in this case at a value of 0.95. The synthetic data representing the through-focus intensity distribution are obtained by assuming an exact linearly polarized illumination of the entrance pupil along the x-axis. The linear state of polarization is then varied by adapting the coefficients p_x and p_y while having p_x and p_y both real and maintaining $(|p_x|^2 + |p_y|^2) = 1$ for normalization purposes. This leads to a rotation of the plane of polarization

towards a certain finite angle with respect to the x-axis. This presumed linear state of polarization, different from the actual state of the system, leads to an error in the retrieved set of β-coefficients. The results of these simulations are

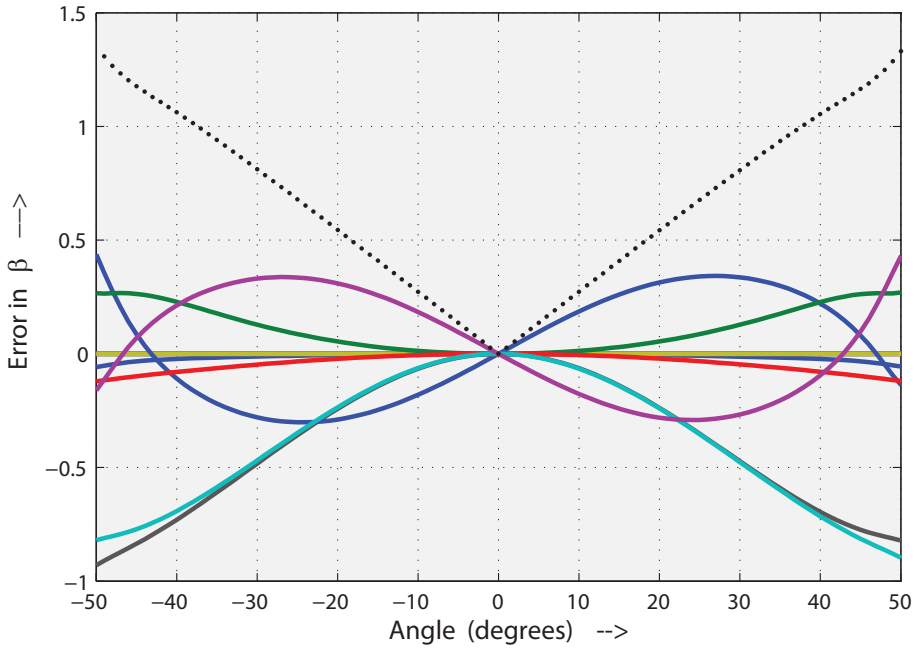

Fig. 5.13. The error present in some selected retrieved β-coefficients (solid lines) as a function of the off-set angle between the chosen plane of polarization at the construction stage of the synthetic intensity data (x-polarization) and the angle of the polarization plane at the retrieval stage. The dotted line is a plot of the total rms error of the retrieved β-coefficients, defined by $(\sum_{nm} |\Delta\beta_n^m|^2)^{\frac{1}{2}}$, with $\Delta\beta_n^m$ the error in each coefficient.

given in Fig. 5.13, where the error present in the set of retrieved β_n^m-coefficients is plotted versus the angle between the supposed and the actual orientation of the plane of polarization. From Fig. 5.13 one observes that it is also important to have accurate knowledge of the polarization state of the system under consideration in order to obtain good retrieval quality. An angular deviation of one degree is a practical limit when it is needed to assess very high-quality imaging systems with sufficient accuracy.

The above example illustrates an interesting relation between the possible inaccuracy in the polarization state and the error in the retrieved β-coefficient. For an optical system of which the polarization state is approximately known, an equivalent operation as used for the generation of Fig. 5.13 can be put into place to determine the polarization state with great accuracy. For the general case that one has no knowledge whatsoever about the state of polarization, the above procedure is no longer applicable. This is caused by the fact that the predictor-corrector procedure is not applicable once the deviations from the real state of polarization are very large. In this case, a basic retrieval op-

eration can be used to obtain the approximate polarization state after which the predictor-corrector method can be applied to determine the state of polarization with great accuracy.

5.3.5 Quality assessment of a high-NA optical system in the presence of noise

Like in the scalar approach, a good estimate of the influence of intensity noise on the retrieved β-coefficients is required. Zero-mean intensity noise can be added to a synthetic data set to perform a numerical noise experiment. In [van Haver, Braat, Dirksen, Janssen (2006)], a through-focus intensity distribution is constructed, corresponding to the β-coefficients of Table 5.4, first two columns. The resulting through-focus intensity distribution is sampled in $2N + 1$ axial planes, several of which are shown in the top row of Fig. 5.14). Noise is added yielding the corresponding pictures in the second row. The noisy distribution (SNR=10 with respect to the highest measured intensity in the best focal plane) is used for a retrieval operation in which all other parameters are assumed to be exactly known. The retrieval results are shown on the third and fourth row. The pictures on the third row are obtained after a single retrieval step, the fourth row gives the results after convergence using the predictor-corrector method. Although a visual inspection hardly shows any difference between the original and the retrieved intensity distributions of Fig. 5.14, the differences are made clear by inspection of Table 5.4. With the chosen values of the β-coefficients, a predictor-corrector step is essential for obtaining the correct input values. It is striking that the presence of the noise does not change the first estimate after linear retrieval. It is the convergence towards the final correct values with the predictor-corrector method that is obstructed by the noise. With the signal to noise ratio of 10, the final coefficients show deviations of the order of 10 to 15%.

5.3.6 Quality assessment of a high-NA system using experimental data

In this subsection we discuss the quality assessment of a lithographic projection lens with a numerical aperture of 0.85 [Dirksen, Braat, Janssen, Leeuwestein (2005)]. The lithographic lens is illuminated by a special illuminator using an excimer laser emitting radiation at λ=193 nm. The radiation of the multimode laser source is effectively unpolarized after integration over the exposure time that is needed to create a developable latent image in the photo-resist layer. The point-spread function created by such an effectively unpolarized focused beam is given by Eq.(3.20). In the aberration-free case, it possesses

		$SNR = \infty$		$SNR = 10$	
Input coeff.		Lin. retr.	Pr.-Corr.	Lin. retr.	Pr.-Corr.
β_0^0	1.0	1.1294	1.0000	1.1291	1.0004
β_1^{-1}	0.0	0.1002	0.0000	0.0934	0.0050
	$+i0.5$	$+i0.4278$	$+i0.5000$	$+i0.4277$	$+i0.4933$
β_1^1	0.0	0.0997	0.0000	0.0973	-0.0124
	$+i0.5$	$+i0.4576$	$+i0.5000$	$+i0.4598$	$+i0.5068$
β_3^{-1}	0.5	0.4545	0.5000	0.4401	0.4688
	$+i0.0$	$+i0.0028$	$+i0.0000$	$+i0.0144$	$+i0.0099$
β_3^1	-0.5	-0.4330	-0.5000	-0.4339	-0.5041
	$+i0.0$	$-i0.0008$	$+i0.0000$	$-i0.0174$	$-i0.0385$
β_2^0	0.0	0.0382	0.0000	0.0220	-0.0264
	$+i0.0$	$+i0.0000$	$+i0.0000$	$-i0.0176$	$-i0.0270$
β_2^{-2}	0.0	0.1138	0.0000	0.1276	0.0112
	$+i0.5$	$+i0.5813$	$+i0.5000$	$+i0.5306$	$+i0.4327$
β_2^2	0.0	0.1113	0.0000	0.1122	0.0060
	$+i0.5$	$+i0.3039$	$+i0.5000$	$+i0.3095$	$+i0.5137$
β_3^{-3}	-0.5	-0.3269	-0.5000	-0.3821	-0.5468
	$+i0.0$	$-i0.0843$	$+i0.0000$	$-i0.0641$	$+i0.0253$
β_3^3	0.5	0.5534	0.5000	0.5631	0.5139
	$+i0.0$	$+i0.0869$	$+i0.0000$	$+i0.0535$	$-i0.0296$

Table 5.4
Set of β-coefficients needed to describe the field in the exit pupil of the optical system ($NA = 0.95$) subjected to a numerical test with noise added to the through-focus intensity distribution. The input data were a noise-free intensity distribution and a distribution with a highest signal-to-noise ratio of 10 at best-focus; from the pictures in the second row of Fig. 5.14 it is clear that the SNR-value is much lower for the out-of-focus intensity distributions. Both distributions are formed from synthetic data obtained by a forward calculation. The retrieved coefficients have been obtained by linearized retrieval and by repeated application of the predictor-corrector scheme.

circular symmetry with respect to the optical axis and a cross-section of the theoretical radial cross-section in the optimum focal plane is given in Fig. 5.15. The salient features are the broadening of the central width of the profile with respect to the scalar prediction by approximately 10% and the absence of dark rings (see graph on the right). The broadening effect for unpolarized illumination is predicted by the shape of the orthogonal intensity cross-sections in Fig. 2.14 for linearly polarized illumination. The broadening effect of the unpolar-

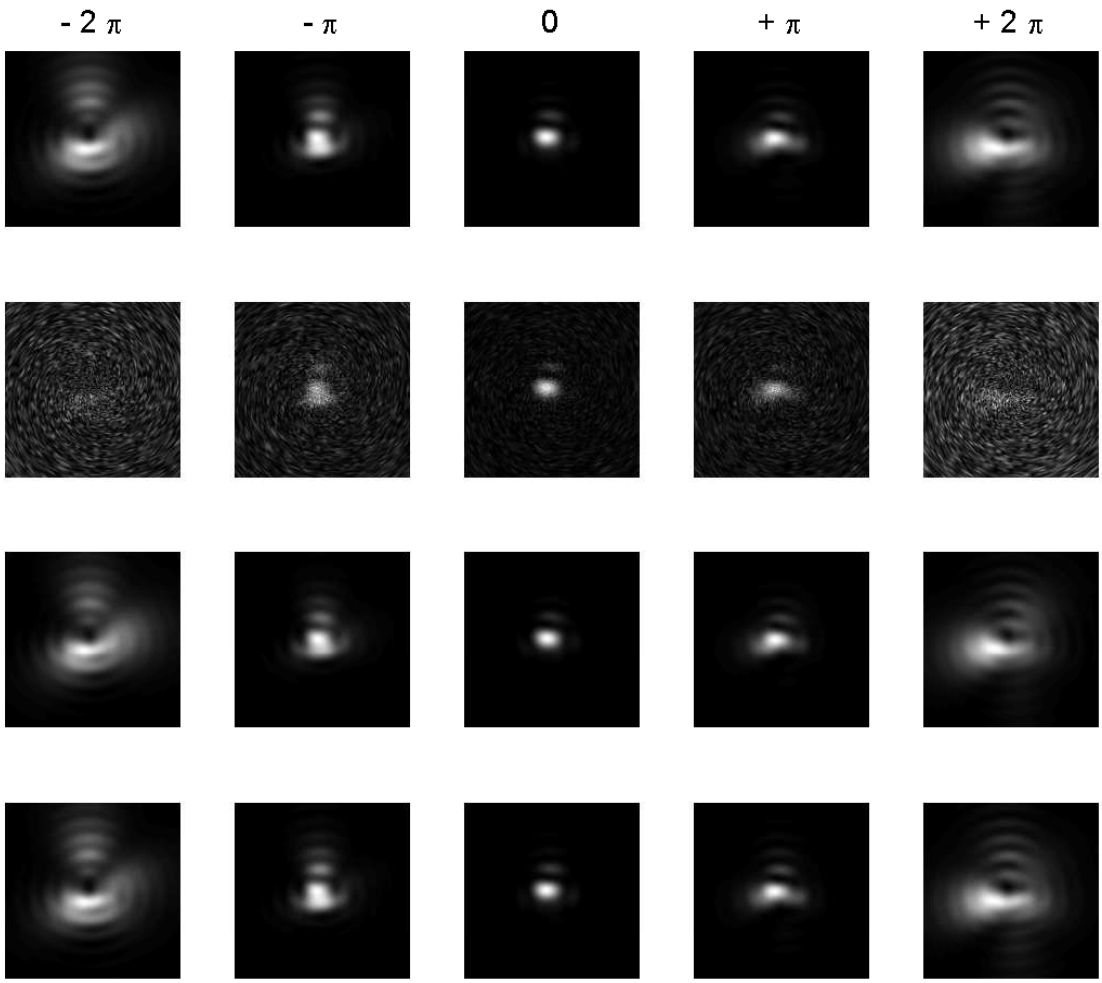

Fig. 5.14. Through-focus intensity distributions pertaining to the system defined by the β-coefficients of Table. 5.4 (NA= 0.95, x-polarization). The upper row is the synthesized actual distribution, the second row is the modified one after adding noise with a SNR of 10. The third row gives the distribution defined by the first β-estimates and the last row is the distribution resulting after the predictor-corrector procedure. Note that all images have been scaled according to their maximum value in order to show maximum detail. The SNR-value of 10 applies to the highest intensity of the in-focus distribution.

ized point-spread function is likely to reduce the resolution capability of the imaging system although it does not necessarily affect the spatial bandwidth of the imaging system.

The assessment of the imaging system with an object point source is carried out in reality with a circular hole in a chromium mask with finite diameter. In the retrieval procedure based on the extended Nijboer-Zernike diffraction theory, the effect of the finite source diameter is accounted for by a complex defocus parameter, see Eq.(5.15). Including such a finite hole size in the

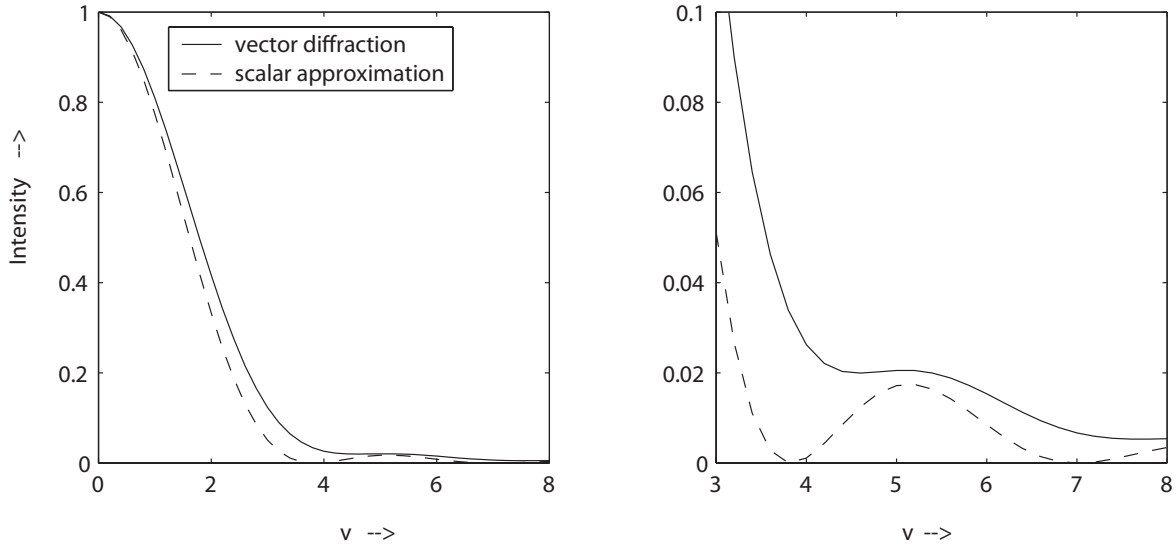

Fig. 5.15. Radial cross-section of the normalized in-focus intensity in the case of a high-numerical aperture aberration-free optical system (s_0=0.85) that is illuminated with effectively unpolarized light. The radial coordinate is $v = 2\pi r$ with r expressed in the diffraction unit λ/s_0.

point-spread calculations gives rise to the through-focus cross-sections of Fig. 5.16. In the left graph, a comparison with the theoretical point-source response

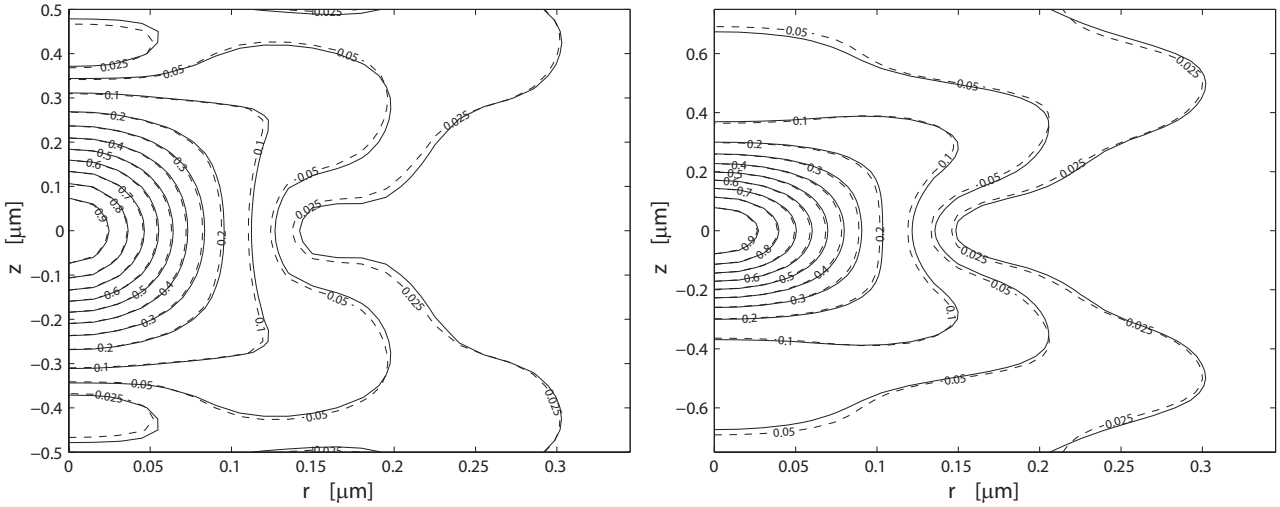

Fig. 5.16. Through-focus cross-sections of the radially symmetric point-spread function in the presence of a finite diameter of the source. The diameter of the circular source is 50 nm (left figure) and 200 nm (right figure) and has to be scaled by the magnification (1/4) of the imaging system ($s_0 = 0.85$, λ=193 nm). The solid lines are obtained using a lithographic simulation package, [SOLID-C (2004)], the dashed lines have been calculated using the extended Nijboer-Zernike formalism. The vertical and horizontal coordinates, z and r respectively, apply to the focal position and the radial image coordinate, both expressed in real space units of μm.

would show only minor differences because of the 12.5 nm geometrical size at the image side. The graph on the right shows an appreciable broadening, the scaled source size becoming comparable to the halfwidth of the theoretical point-spread function.

The retrieval procedure using the inner product method exploits the (non-perfect) orthogonality of the through-focus intensity patterns corresponding to a specific Zernike coefficient of the pupil function. As an example of two such patterns, we first produce in Fig. 5.17 the aberration-free pattern that is basically associated with the coefficient $|\beta_0^0|^2|V_0^0|^2$ with $\beta_0^0 = 1$ (left graph). The graph on the right is the through-focus pattern of a system that suffers

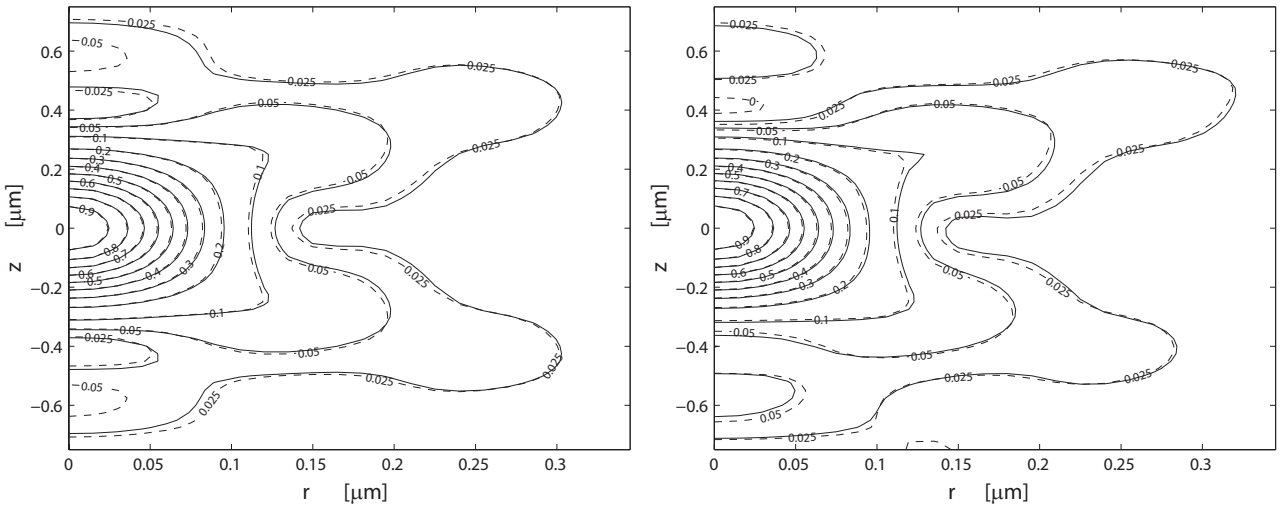

Fig. 5.17. Through-focus cross-section of a radially symmetric point-spread function for the aberration-free case, leftfigure, and in the case where spherical aberration of lowest order is present ($\beta_4^0 \approx 0.25i$, right figure). The solid lines are obtained using the lithographic simulation package SOLID-C, the dashed lines have been calculated using the extended Nijboer-Zernike formalism. Vertical and horizontal coordinates in μm; $s_0 = 0.85$, λ=193 nm.

from lowest order spherical aberration and is, in a first order, proportional to the sum of a contribution associated with $(\beta_0^0)^2$ and contributions stemming from the product of $\beta_0^0 \beta_4^{0\,*}$ and the corresponding product of V-functions. The graph on the right has been calculated with a spherical aberration coefficient of $\beta_4^0 \approx 0.25i$ or a value $Z_9 = 40\ m\lambda$ (Fringe Convention). In the case of Fig. 5.17, the partial orthogonality between the two patterns stems from the asymmetry through focus of the point-spread function with spherical aberration.

As it was pointed out in Subsection 5.1.3, the detected point-spread function is blurred by various effects like mechanical movements in the axial direction or in the plane of the image, or by chemical diffusion of the latent resist image, mainly during the post-exposure bake of the developed resist layer. These effects can be mapped on a radial and axial blurring of the image, the magnitude of which is represented by the standard deviations σ_r and σ_f. The graph on the right of Fig. 5.18 shows that a radial diffusion with a typical value of σ_r=40 nm has a very large impact on the radial scale of the detected point-spread function. With the aberration-free full width at half maximum of the

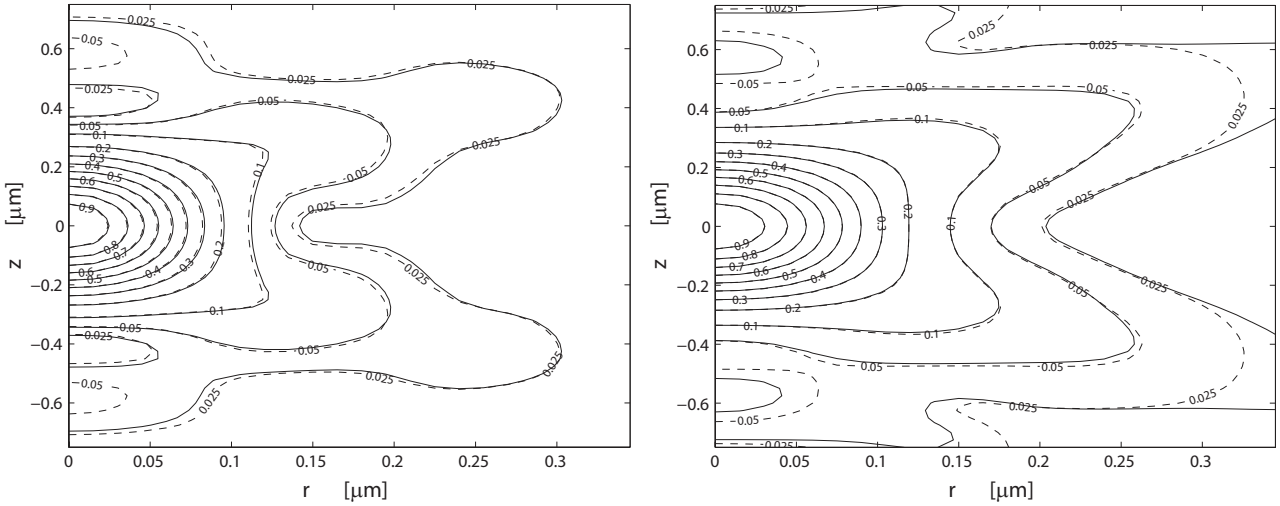

Fig. 5.18. Through-focus cross-section of the aberration-free point-spread function (left graph) and the point-spread function contours of the recorded latent image after a diffusion process in the resist layer (right figure) with σ_r=40 nm. The solid lines are again obtained using the SOLID-C package, the dashed lines have been calculated with the Nijboer-Zernike formalism. Vertical and horizontal coordinates in μm; $s_0 = 0.85$, λ=193 nm.

point-spread function in the radial direction given by 65 nm, we observe an increase to 85 nm in the graph on the right, showing that the diffusion effect in resist imaging should not be neglected.

With the extensions described above, a retrieval operation can be carried out on experimental data, including lateral diffusion and axial blurring. The through-focus point-spread function data were obtained with the resist printing method sketched in Fig. 5.5. The contour lines of the experimental through-focus point-spread function are shown in Fig. 5.19, solid lines. They apply to a lithographic projection objective with a numerical aperture of 0.85, used in water immersion. The refractive index of water is 1.4367 at the deep UV wavelength of 193 nm. It is important to note that the contour lines cannot be experimentally constructed at relatively high intensity levels where the contour diameter becomes small. The corresponding resist images are beyond the recording capabilities of current photo-resist materials. This fact has not proven to be detrimental in the retrieval process because the point-spread function deformation by aberrations is most visible at larger values of the radial coordinate and there where the diffraction ring structure is found. The retrieval procedure carried out on the experimental data gave rise to a very low aberration level with $|\beta_4^0| \leq 0.05$. The dominating factor for the contour line broadening was due to the diffusion and blurring in the lateral and axial directions. The standard deviations of these blurring phenomena could also be retrieved by using them as free parameters in the retrieval method. In line with

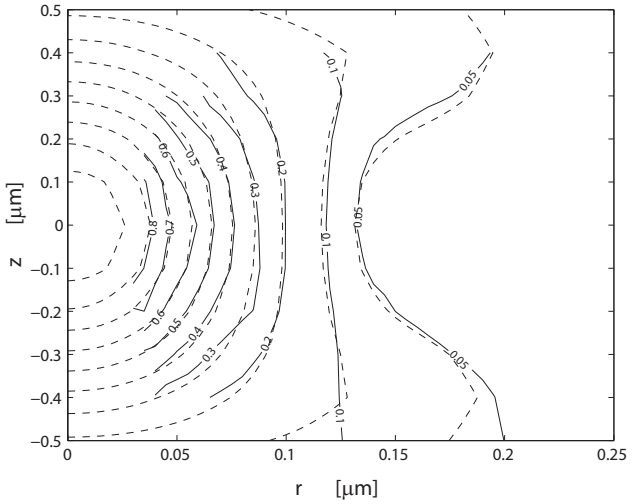

Fig. 5.19. An experimentally obtained through-focus contour plot (solid lines) of a point-spread function in a thin photo-resist layer. The dashed lines have been obtained after Zernike coefficient retrieval using the extended Nijboer-Zernike formalism. Vertical and horizontal coordinates in μm; λ=193 nm, water immersion with n=1.4367, $s_0 = 0.85/1.4367$.

[Dirksen, Braat, Janssen (2006)], a merit function can be defined according to

$$M(\sigma_r, \sigma_f) = \frac{\sum_{n\neq 0} \frac{\left\{\Re[\beta^0_{2n}(\sigma_r,\sigma_f) - \beta^0_{2n,o}]\right\}^2}{2n+1}}{\sum_n \frac{\left|\beta^0_{2n}(\sigma_r,\sigma_f) - \Re[\beta^0_{2n,o}]\right|^2}{2n+1}}, \tag{5.28}$$

where the real parts $\Re[\beta^0_{2n,o}]$ with $n \geq 2$ represent the deviation from unity of the transmission function of the imaging system, in most cases available by *a priori* knowledge about the system. The blurring due to lateral diffusion and defocus could become visible in the retrieved coefficients by a change in their real parts that affect the transmission function of the imaging system. A reduced resolution because of blurring can be enforced by a reduction in the amplitude transmission function at the pupil rim to effectively reduce the numerical aperture of the system. Given the original circularly symmetric transmission function of the imaging system, well represented by the coefficients $\Re[\beta^0_{2n,o}]$, the quantity ($M(\sigma_r, \sigma_f)$ weighs the change in these coefficients with respect to the total power in the retrieved complex β-coefficients. The combination of σ_r- and σ_f-values that minimizes M is the most likely solution for the retrieval problem at hand. When the retrieval procedure using minimization of M was applied to the data set of Fig. 5.19, the values σ_r=16 nm and σ_r=100 nm were obtained.

The initial state of polarization of the incident wave in the entrance pupil of an optical system is modified when it propagates through the optical system. The change in state of polarization because of a change in beam convergence has been extensively described for a high-NA system in Subsection 2.5.3. Another factor that influences the state of polarization on the ext pupil sphere is associated with the polarization-dependent amplitude and phase changes on transmission through the (coated) air-lens and lens-air interfaces of an imaging system or the reflections at mirror surfaces; these are especially appreciable in imaging systems with a high numerical aperture where the ray incidence angles at intermediate surfaces can be large. We also mention possible anisotropy of the lens materials or the reflective coatings. This anisotropy can be induced by structural properties but also by residual stresses in the coatings or lens materials. The result is a gradual or abrupt change in the state of polarization on propagation of the radiation through the imaging system. In [Braat, Dirksen, Janssen, van de Nes, van Haver (2005)] it is indicated how these polarization-sensitive effects can be dealt with in a high-numerical-aperture system. By a number of retrieval steps with different states of polarization in the entrance pupil of the system, one obtains several sets of complex Zernike coefficients corresponding to these incident polarization states. The combination of these retrieved sets of coefficients leads to the value of the geometric wave front deformation and to the amplitude and axis orientation of the cumulative system birefringence in each point on the exit pupil sphere. The exact procedure is briefly pointed out below.

I. *Obtaining the required field components E_x and E_y in the exit pupil*

The cumulative effect of birefringence in the optical system is represented in each point on the exit pupil sphere by a certain value of the retardation due to the birefringence, Δ_b, and the azimuths of the orthogonal principal axes, for instance, by defining the angle α_b of the 'slow' axis of the birefringence. For most practical cases, it is allowed to simplify the analysis by neglecting the dichroism introduced by the optical system. This means that we trust that the amplitude anisotropy, for instance by modulus changes in the transmission or reflection coefficients at surfaces, will have much less influence on the system performance than the corresponding phase anisotropy. This is a reasonable assumption once we do not employ resonant structures like multi-layer coatings in an optical system. Thus, in the modified expressions for the E-field components in the exit pupil due to birefringence, only phase 'retardation' will be

considered.

The state of polarization in the exit pupil is now analyzed using the Jones matrix analysis. The matrix relation between the x- and y-components of the input and output electric fields belonging to a plane wave that has traversed a birefringent optical element is given by [Jones (1941)], [McGuire, Chipman (1990)]

$$\begin{pmatrix} E_{x,j} \\ E_{y,j} \end{pmatrix} = \begin{pmatrix} \mathcal{J}_{11} & \mathcal{J}_{12} \\ \mathcal{J}_{21} & \mathcal{J}_{22} \end{pmatrix} \begin{pmatrix} p_{x,j} \\ p_{y,j} \end{pmatrix} A_j = \mathcal{J}(\rho,\theta) \begin{pmatrix} p_{x,j} \\ p_{y,j} \end{pmatrix} A_j, \tag{5.29}$$

where the complex amplitudes of the x- and y-components of the incident electric field at the j-th exposure or detection are given by $(p_{x,j}A_j, p_{y,j}A_j)$ with A_j the modulus of the amplitude of the incident fields. The field components $(E_{x,j}, E_{y,j})$ depend on the position (ρ,θ) in the entrance pupil because, in general, the $\mathcal{J}$-matrix is spatially varying. The functions describing the locally varying complex amplitudes can be expanded with the aid of Zernike polynomials and their coefficients, $\beta_{n,x}^m$ and $\beta_{n,y}^m$. The field components $(E_{x,j}, E_{y,j})$, affected by the birefringence of the optical system, will now formally replace the original components $(p_{x,j}, p_{y,j})A_j$ in the entrance pupil. The Zernike expansions corresponding to $(E_{x,j}, E_{y,j})$ are then used to determine the vector components of the field on the exit pupil sphere and these are used to evaluate the field in the focal region, see Eq.(2.65).

II. *Linearized energy density in the presence of birefringence*

Basically, we need to evaluate the four complex matrix elements $\mathcal{J}_{ij}$ for each sample point in the exit pupil, leading to eight independent quantities to be determined. But since we have excluded dichroism, the above matrix has a special structure [Lu, Chipman (1994)]-[Stallinga (2004-2)] and can be written as

$$\mathcal{J} = \begin{pmatrix} \mathcal{J}_{11} & \mathcal{J}_{12} \\ -\mathcal{J}_{12}^* & \mathcal{J}_{11}^* \end{pmatrix}, \tag{5.30}$$

with the property $|\mathcal{J}_{11}|^2 + |\mathcal{J}_{12}|^2 = 1$. The eigenstates of this matrix are elliptical in general. Once the eigenvalues and eigenstates have been found, the orientation α of the slow and fast axes and the value Δ_b of the phase birefringence are known.

The retrieval procedure starts with Eq.(3.8) where we use the still unknown

coefficients $\beta^m_{n,x}$ and $\beta^m_{n,y}$ to construct the energy density in the focal volume. The effect of birefringence has to be accounted for in each basic function $G_{kl}(\beta_x, \beta_y)$, see Eq.(3.4). Linearization of $G_{kl}(\beta_x, \beta_y)$, keeping only products with $\beta^0_{0,x}$ or $\beta^0_{0,y}$, gives contributions from lines 1 and 5-8 in Eq.(3.4). Ordering these terms leads to the following general expression, comparable to Eq.(5.23) for the isotropic case,

$$G_{k,l}(\beta_1, \beta_2)\} = \exp\{i(k-l)\phi\} \sum_{\nu\geq 0} \sum_{\mu\neq 0} \left\{\beta^0_{0,1}\ \beta^{\mu *}_{\nu,2} \Psi^{\mu *}_{\nu;k,l}(r,f) \exp(-i\mu\phi) \right. \\ \left. + (1-\delta_{\nu\mu}) \beta^{0*}_{0,2}\ \beta^{\mu}_{\nu,1} \Psi^{\mu}_{\nu;l,k}(r,f) \exp(+i\mu\phi)\right\}. \qquad (5.31)$$

The difference between the coefficients $\beta^0_{0,1}$ and $\beta^0_{0,2}$ is due to the average birefringence over the exit pupil. Because of the neglect of dichroism, these two coefficients have equal moduli but show a phase difference Δ_{12} defined by

$$\left.\begin{aligned} \beta^0_{0,1} &= \beta^0_0 \exp\{i\Delta_{12}/2\} \\ \beta^0_{0,2} &= \beta^0_0 \exp\{-i\Delta_{12}/2\} \end{aligned}\right\} \quad \text{or,} \quad \beta^0_{0,2} = \beta^0_{0,1} \exp\{-i\Delta_{12}\}. \qquad (5.32)$$

With this definition of the $(0,0)$-coefficients, we obtain

$$G_{k,l}(\beta_1, \beta_2)\} = \exp\{i(k-l)\phi\} \beta^0_0 \exp\{i\Delta_{12}/2\}\ \times \\ \sum_{\nu\geq 0} \sum_{\mu\neq 0} \left\{\beta^{\mu *}_{\nu,2} \Psi^{\mu *}_{\nu;k,l}(r,f) \exp(-i\mu\phi) \right. \\ \left. + (1-\delta_{\nu\mu})\ \beta^{\mu}_{\nu,1} \Psi^{\mu}_{\nu;l,k}(r,f) \exp(+i\mu\phi)\right\}. \qquad (5.33)$$

Inspection of the above expression shows that the relationship $G_{kl}(\beta_1, \beta_2) = G^*_{lk}(\beta_2, \beta_1)$ remains valid using the property $\Delta_{12} = -\Delta_{21}$.

Because of the special structure of the unitary matrix $\mathcal{J}$, three independent quantities need to be determined on top of the geometrical wavefront aberration and transmission defects of the system. We thus need four retrieval operations to determine the complex quantities $\mathcal{J}_{11}$ and $\mathcal{J}_{12}$ plus the polarization-independent geometrical defects of the system. Preferred polarization states $(p_{x,j}, p_{y,j})$ are two orthogonal linear polarization states, e.g. $(1,0)$ and $(0,1)$ and the circular ones, viz. $(1,i)/\sqrt{2}$ for left-circularly polarized and $(1,-i)/\sqrt{2}$ for right-circularly polarized light. The four exposures or detection steps with the preferred polarization states lead, after retrieval, to four different sets of β_x- and β_y-coefficients. The four sets of β-coefficients are now used to obtain the complex amplitude in any point of the exit pupil for four different polarization states. This is basically sufficient to uniquely determine the size and

the orientation of the cumulative birefringence of the optical system in that specific point of the exit pupil. In addition, we obtain the geometrical defects of the system that are independent of the state of polarization in the entrance pupil of the optical system.

6 Conclusion and outlook

The assessment of optical systems regarding their imaging capability focuses on the measurement of the exit pupil function. Especially the phase part of the exit pupil function is important as it determines the imaging aberrations and possible birefringence of the system. An accurate knowledge of the exit pupil function, both in the design and in the manufacturing stage, allows for the correction of aberrations or birefringence in the fine-tuning manufacturing step. Precision interferometry is the most direct method to measure the exit pupil function. In practice, its applicability is somewhat limited because of the requirement of special sources and extremely well specified reference surfaces. In this chapter we have discussed the measurement of the point-spread function of an imaging system as a means to obtain accurate information about the defects of the wave in the exit pupil, not only regarding the aberrations of the system under test but also including its transmission and birefringence defects. A prerequisite for solving the so-called inverse problem is the accurate knowledge of the point-spread function in the focal volume as a function of the aberrations and other defects of the exit pupil function. For systems with a high numerical aperture, the state of polarization of the incident field has to be included and the vector diffraction integral of the aberrated system has to be solved. Based on the use of Zernike polynomials, we have discussed semi-analytic expressions for the complex amplitude and the energy density in the focal region. They first apply to the scalar diffraction case at low numerical aperture, to an extended scalar regime for apertures up to values of 0.85 and, finally, to the vector diffraction case at very high aperture close to unity regarding the sine of the opening angle of the focusing beams. The availability of analytic expressions offers an interesting short-cut to the more laborious propagation methods based on a numerical solution of the diffraction integrals involved in the propagation from the exit pupil to the focal region.

Inverse problem solution in optical imaging has been addressed by several authors, based on the matching of measured intensity distributions in the image plane and the exit pupil function intensity. Certain physical constraints are applied like the non-negativity of optical intensity or the limited extent of a point-spread or pupil function to assure convergence towards a most likely solution. Like in optical interferometry, the method of phase diversity has been introduced in optical inverse problem solution to avoid the phase ambiguity that is possible when intensity measurements are used to retrieve the complex amplitude of the exit pupil function. We have focused in the last

part of this chapter on a special application of the phase diversity principle, the collection of through-focus point-spread functions to reconstruct the complex amplitude of the exit pupil. With our analytic expression for the energy density or, equivalently, for the power flow in the focal region, we are capable to address the inverse problem of how to retrieve the coefficients of the Zernike expansion of the complex pupil function that created the measured through-focus point-spread function. Using a linearized version of the energy density function for weak system defects, a system of equations is developed to solve for the unknown complex Zernike coefficients. At larger defect values, a predictor-corrector method is applied to improve the solution. The total range of aberration and other defects that can be covered in this way is well in excess of what is needed for good-quality imaging systems. The quality assessment method takes into account the particularities of the detecting medium. For very high resolution systems, a photo-resist layer is needed to record the extremely fine features of the through-focus point-spread functions. The chemical diffusion in a resist layer is accounted for and a matching procedure allows the precise estimate of the magnitude of this diffusion effect. The same matching principle can be applied to other blurring factors like in-plane and axial vibrations during the point-spread function exposure time. It is equally possible to obtain an accurate estimate of the value of the numerical aperture of the system under test and of the state of polarization of the light incident on the entrance pupil. Future work in this direction will address the assessment of systems with a more general pupil configurations, especially those with a central obstruction. An extension of the analysis to systems with broadband illumination would be of great practical importance because this would bring within reach applications in the fields of, for instance, astronomical observation and ophthalmology.

Acknowledgement
One of the authors (J.B.) thanks the Technical University of Delft for the opportunity of a sabbatical leave and Profs. Mario Bertolotti and Concita Sibilia of University 'La Sapienza', Rome, for their generous hospitality during this sabbatical leave.

Appendices

A Derivation of Weyl's plane wave expansion of a spherical wave

The time-independent Helmholtz equation is given by

$$(\nabla^2 + k^2) f(\mathbf{r}, \mathbf{r}') = -\delta(\mathbf{r} - \mathbf{r}') \ , \tag{A.1}$$

where the point source is located at $\mathbf{r} = \mathbf{r}'$. The (normalized) solution for the three-dimensional geometry is given by the expression for a scalar spherical wave

$$f_3(x, y, z; x', y', z') = \frac{\exp(ik|\mathbf{r} - \mathbf{r}'|)}{4\pi|\mathbf{r} - \mathbf{r}'|} \ , \tag{A.2}$$

with $|\mathbf{r} - \mathbf{r}'|$ given by $\{(x - x')^2 + (y - y')^2 + (z - z')^2\}^{1/2}$. A solution for the one-dimensional geometry where a uniform coherent source covers the entire plane $z = z'$ is obtained from the Helmholtz equation

$$(\nabla^2 + k_z^2) f(x, y, z; k_x, k_y, z') = -\delta(z - z') \ , \tag{A.3}$$

where the value of k_z is given by $k_z^2 = k^2 - k_x^2 - k_y^2$. The individual plane wave solutions of this equation are given by

$$f_1(x, y, z; k_x, k_y, z') = \frac{i}{2k_z} \exp\{ik_z|z - z'|\} \ \exp[i(k_x x + k_y y)] \ . \tag{A.4}$$

The validity of this plane wave solution is easily checked by substituting the solution in Eq.(A.3) and by verifying, using Gauss' theorem, that

$$\oint \nabla f_1 \ \cdot \ \mathbf{n} \, dS = \iiint \left[-\delta(z - z') - k_z^2 f\right] dV \ , \tag{A.5}$$

where the surface S is that of a thin box at $z = z'$ that infinitely extends in the x- and y-directions and has a vanishing thickness in the z-direction, $\mathbf{n}$ is the outward normal to S and the volume V is the interior of the box. The complete solution for the one-dimensional geometry is obtained by an integration over all (k_x, k_y).

The one-dimensional solution can equally well be constructed from the three-dimensional solution by a 2D-integration over the source plane at $z = z'$. This leads to the alternative expression

$$f_1(x,y,z;k_x,k_y,z') = \iint_{-\infty}^{+\infty} f_3(x,y,z;x',y',z') \times \exp\{i[k_x(x-x')+k_y(y-y')]\}dx'dy'$$
$$= \exp\{i[k_x x + k_y y]\} \iint_{-\infty}^{+\infty} \frac{\exp\{ik|\mathbf{r}-\mathbf{r}'|\}}{4\pi|\mathbf{r}-\mathbf{r}'|} \times \exp\{-i[k_x x' + k_y y']\}dx'dy' \ . \qquad (A.6)$$

When comparing Eq.(A.4) and Eq.(A.6), it can be concluded that the second integral in (A.6), the Fourier transform of $f_3(x,y,z;x',y',z')$, should equal $(i/2k_z)\exp\{ik_z(|z-z'|\}$. By taking the inverse Fourier transform of both quantities we obtain

$$FT^{-1}\left[FT\left(\frac{\exp\{ik|\mathbf{r}-\mathbf{r}'|\}}{4\pi|\mathbf{r}-\mathbf{r}'|}\right)\right] = \frac{i}{(2\pi)^2} \times \iint_{-\infty}^{+\infty} \frac{\exp\{i[k_z|z-z'| + k_x x + k_y y]\}}{2k_z} dk_x dk_y \ , \qquad (A.7)$$

or, in its most elementary notation,

$$\frac{\exp(ik|\mathbf{r}|)}{|\mathbf{r}|} = \frac{i}{2\pi} \iint_{-\infty}^{+\infty} \frac{\exp\{i[k_z z + k_x x + k_y y]\}}{k_z} dk_x dk_y \ . \qquad (A.8)$$

B The Debye integral in the presence of aberrations

The angular spectrum of the field distribution in the aperture $\mathcal{A}$ is given by Eq.(2.12). In the aberrated case the field $E_0(x',y')$ is written as $A_0(x',y')\times \exp\{i\Phi(x',y')\}$. The function $\Phi(x',y') = kW(x',y')$ is the phase deviation resulting from the aberration $W(x',y')$ from the spherical shape of the incident wavefront. Our sign convention implies that a positive wavefront aberration corresponds to a position of the wavefront further away from the focal point F than in the aberration-free case. To obtain an asymptotic value of $\tilde{E}(z';k_x,k_y)$, the stationary points of the integrand in Eq.(2.12) with respect to x' and y' have to be found. Writing the integrand as

$$\frac{A_0(x',y')}{R_{QF}} \exp\{-i[kR_{QF} + k_x x' + k_y y' - \Phi(x',y')]\} = g(x',y')\exp\{ih(x',y')\} \ , \qquad (B.1)$$

we find the stationary points by putting $\partial h/\partial x' = 0$ and $\partial h/\partial y' = 0$, and this yields the equations

$$\begin{aligned}\frac{k(x'-x_f)}{R_{QF}} &= -k_x + \frac{\partial\Phi}{\partial x'},\\ \frac{k(y'-y_f)}{R_{QF}} &= -k_y + \frac{\partial\Phi}{\partial y'}.\end{aligned} \tag{B.2}$$

These equations can be solved by squaring both equations, next summing them and adding $(z'-z_f)^2/R_{QF}^2$ to the result, finally yielding

$$1 = \frac{(z'-z_f)^2}{R_{QF}^2} + \frac{1}{k^2}\left[\left(k_x - \frac{\partial\Phi}{\partial x'}\right)^2 + \left(k_y - \frac{\partial\Phi}{\partial y'}\right)^2\right] \tag{B.3}$$

Neglecting the second order terms in $\partial\Phi/\partial x'$ and $\partial\Phi/\partial y'$ we find

$$\frac{R_{QF}}{k} = \frac{z_f - z'}{k_z\left[1 + \frac{2}{k_z^2}\left(k_x\frac{\partial\Phi}{\partial x'} + k_y\frac{\partial\Phi}{\partial y'}\right)\right]^{(1/2)}}. \tag{B.4}$$

For small derivative values of Φ, the stationary points are approximated by

$$\begin{aligned}x_s^{'} &\approx x_f - \frac{k_x(z_f-z')}{k_z}\left\{1 - \left(\frac{k^2-k_y^2}{k_x k_z^2}\right)\frac{\partial\Phi}{\partial x'} - \frac{k_y}{k_z^2}\frac{\partial\Phi}{\partial y'}\right\},\\ y_s^{'} &\approx y_f - \frac{k_y(z_f-z')}{k_z}\left\{1 - \frac{k_x}{k_z^2}\frac{\partial\Phi}{\partial x'} - \left(\frac{k^2-k_x^2}{k_y k_z^2}\right)\frac{\partial\Phi}{\partial y'}\right\}.\end{aligned} \tag{B.5}$$

In the aberration-free case, we find the stationary points that already appeared in the argument of E_0 in Eq.(2.13). It is common practice to neglect the influence of aberrations on the position of the stationary points in the diffracting aperture. If the aberration is small and the aperture size is many wavelengths large, the derivatives of Φ will remain relatively small and the factors between braces in Eq.(B.5) can be put equal to unity. A more careful examination is needed at high numerical aperture values when the various pre-factors containing k_x, k_y and k_z can become large; high order aberrations also yield higher derivative values in Eq.(B.5).

C Series expansion of the diffraction integral at large defocus

The diffraction integral corresponding to $V_n^m(r,f)$ is written using Bauer's formula according to Eq.(2.45) yielding

$$V_n^m(r,f) = \exp(\frac{if}{2}) \sum_{k=0}^{\infty} (2k+1)\, i^k\, j_k(f/2) \times \int_0^1 R_{2k}^0(\rho)\, R_n^m(\rho)\, J_m(2\pi r\rho)\, \rho\, d\rho \ . \tag{C.1}$$

The polynomial product in the integrand of Eq.(C.1) is written as

$$R_{2k}^0(\rho)\, R_{m+2p}^m(\rho) = \sum_l w_{kl}\, R_{m+2l}^m(\rho) \ . \tag{C.2}$$

In [Janssen, Braat, Dirksen (2004)] it is shown that the coefficients w_{kl} can be represented by a double series involving the product of three other coefficients according to

$$w_{kl} = \sum_{s=0}^{p} \sum_{t=0}^{\min(k,s)} f_{ps}^m\, g_{k+s-2t,\,l}^m\, b_{kst} \ , \tag{C.3}$$

with the coefficients f, g and b given by

$$f_{ps}^m = (-1)^{p-s}\, \frac{2s+1}{p+s+1}\, \frac{\binom{m+p-s-1}{m-1}\binom{m+p+s}{s}}{\binom{p+s}{s}} \ , \qquad s = 0,...,p \ , \tag{C.4}$$

$$g_{ul}^m = \frac{m+2l+1}{m+u+l+1}\, \frac{\binom{m}{u-l}\binom{u+l}{l}}{\binom{m+l+u}{m+l}} \ , \qquad u = l,...,l+m \ , \tag{C.5}$$

$$b_{s_1 s_2 t} = \frac{2s_1+2s_2-4t+1}{2s_1+2s_2-2t+1}\, \frac{A_{s_1-t}\, A_t\, A_{s_2-t}}{A_{s_1+s_2-t}} \ , \qquad t = 0,...,\min(s_1,s_2), \tag{C.6}$$

and the coefficients A_k given by the binomial coefficient $\binom{2k}{k}$. We have $w_{kl} \neq 0$ only when l between $\max(0, k-p-m, p-k)$ and $k+p$. Also $w_{kl} \geq 0$ in all cases.

A special case arises when $m = 0$ and the expressions of Eqs.(C.4)-(C.5) are now defined as

$$f_{ps}^0 = \delta_{ps} \ , \qquad\qquad g_{ul}^0 = \delta_{ul} \ , \tag{C.7}$$

with δ_{ab} equal to Kronecker's delta symbol. Here, as before, n, m are integers ≥ 0 with $n-m \geq 0$ and even, and the definitions for p and q are, respectively, $p = (n-m)/2$ and $q = (n+m)/2$.

D Series expansion for the diffraction integral $V_{n,j}^m(r,f)$

In this Appendix, we present two methods for obtaining a series expansion of the integral $V_{n,j}^m(r,f)$ given by

$$V_{n,j}^m(r,f) = \int_0^1 \rho^{|j|} \frac{\left(1+\sqrt{1-s_0^2\rho^2}\right)^{-|j|+1}}{(1-s_0^2\rho^2)^{1/4}} \exp\left[\frac{if}{u_0}\left(1-\sqrt{1-s_0^2\rho^2}\right)\right] \times R_n^{|m|}(\rho) J_{|m+j|}(2\pi r\rho)\rho d\rho \ , \tag{D.1}$$

with m, n, j integers and $n - |m| \geq 0$. We have used the absolute value of the order number $(m+j)$ of the Bessel function. The relation $J_{-n}(x) = (-1)^n J_n(x)$ assures that we can also accommodate negative values of the order index $(m+j)$.

The first method, discussed in [Braat, Dirksen, Janssen, van de Nes (2003)], applies a series expansion that is based on the scalar diffraction integral $V_n^m(r,f)$ according to Eqs.(2.47). The second method uses an expansion with the functions $T_n^m(r,f)$ of Eq.(2.57) as basis functions. Both functions, $V(r,f)$ and $T(r,f)$, have their own Bessel series expansion and expansion coefficients given by Eqs.(2.48)-(2.50) and Eqs.(2.58)-(2.59), respectively.

D.1 Expansion using the functions $V_n^m(r,f)$

The necessary steps that are required to transform the integral Eq.(D.1) into a tractable form are the following;

- we write

$$\left(1+\sqrt{1-s_0^2\rho^2}\right)^{-|j|+1} \exp\left[\frac{if}{u_0}\left(1-\sqrt{1-s_0^2\rho^2}\right)\right] = \exp\left[g_j + if_j\rho^2\right] \sum_{k=0}^{\infty} h_{kj} R_{2k}^0(\rho) \ , \tag{D.2}$$

  and define the coefficients g_j and f_j by requiring the best fit for the constant and the quadratic term in ρ in the expression. The series of Zernike polyno-

mials with coefficients h_{kj} will be normally limited to a constant term h_{0j} close to unity, and, a relatively small higher order term h_{2j}. If the value of s_0, the geometrical numerical aperture, approaches a value of, say, 0.90, or the defocus parameter exceeds the value of 2π, higher order coefficients h_{kj} are needed.

- To reduce the integral $V_{nm,j}(r, f)$ to the analytically known result $V_{nm}(r, f)$, the upper index of the Zernike polynomial and the order of the Bessel function should be identical. Recursion formulae, already presented in [Nijboer (1942)], can be used and the following general relationship can be established

$$\rho^{|j|} R_n^{|m|}(\rho) = \sum_{s=0}^{|j|} c_{n|m|js} R_{n+|j|-2s}^{|m+j|}(\rho) \ . \tag{D.3}$$

- Having determined the two or three new Zernike polynomials that we denote by $R_{n+|j|-2s}^{|m+j|}(\rho)$, we need to evaluate products of these Zernike polynomials with a general polynomial $R_{2k}^0(\rho)$ that appeared in the first step. It can be shown that the following general relationship exists

$$R_{2k}^0(\rho) R_{n+|j|-2s}^{|m+j|}(\rho) = \sum_{t=0}^{\infty} d_{n|m|jskt} R_{n+|j|-2s+2t}^{|m+j|}(\rho) \ \ , \tag{D.4}$$

  and the number of terms t in the summation is normally limited to three. Note that problem of finding the coefficients $d_{n|m|jskt}$ was already solved in Appendix C where an explicit expression for the coefficients w_{kl} was given via Eqs.(C.4)-(C.6).

When combining the above steps we have succeeded in writing $V_{n,j}^m$ as a linear combination of a modest number of terms of the form $V_{n+|j|-2s+2t}^{|m+j|}(r, f_j)$ $\times \exp(g_j)$. A detailed derivation of the expressions for the coefficients g_j and f_j, for the coefficient $c_{n|m|js}$ with running index s and the coefficient $d_{n|m|jskt}$ with running index t can be found in [Braat, Dirksen, Janssen, van de Nes (2003)].

D.2 Expansion using the functions $T_n^m(r, f)$

The expansion according to the second method is more straightforward and allows a better monitoring of the convergence than when using the first method. We start with the slightly more general integral

$$I(r,f) = \int_0^1 \rho^k \frac{\left(1+\sqrt{1-s_0^2\rho^2}\right)^{-p+1}}{(1-s_0^2\rho^2)^{1/4}} \exp\left[\frac{if}{u_0}\left(1-\sqrt{1-s_0^2\rho^2}\right)\right] \times R_n^u(\rho) J_l(2\pi r\rho)\rho d\rho \ , \tag{D.5}$$

where $k, p, u, n, l \geq 0$ and both $n-u$ and $k+u-l$ are ≥ 0 and even. We write

$$R_n^u(\rho) = \rho^u \sum_{s=0}^{\frac{n-u}{2}} C_s \rho^{2s} \quad ; \quad C_s = \frac{(-1)^{\frac{n-u}{2}-s}}{\left(\frac{n-u}{2}-s\right)!\ s!\ (n-s)!} \ , \tag{D.6}$$

and

$$\frac{\left(1+\sqrt{1-s_0^2\rho^2}\right)^{-p+1}}{(1-s_0^2\rho^2)^{1/4}} \exp\left[\frac{if}{u_0}\left(1-\sqrt{1-s_0^2\rho^2}\right)\right] = \exp\{g' + if'\rho^2\} \sum_{t=0}^{\infty} B_t \rho^{2t}. \tag{D.7}$$

The coefficients B_t are obtained from a computation scheme that is given below. Using these coefficients we write the integral $I(r,f)$ as

$$I(r,f) = \sum_{s=0}^{\frac{n-u}{2}} \sum_{t=0}^{\infty} C_s \ B_t \ T^l_{k+u+2s+2t}(r,f') \ , \tag{D.8}$$

with the Bessel series expansion for $T(r,f)$ itself given by Eq.(2.58); there further holds $k+u+2s+2t-l \geq 0$ and even.

The computation scheme for the coefficients B_t runs as follows. As a first step, we bring the fraction on the left-hand side of Eq.(D.7) into the exponential function and split off the optimal quadratic part $g' + if'\rho^2$. The Taylor expansion of the remaining part in the exponential is written as $\sum_{t'=0}^{\infty} A_{t'} \rho^{2t'}$. The coefficients B_t are defined by

$$\sum_{t=0}^{\infty} B_t \rho^{2t} = \exp\left(\sum_{t'=0}^{\infty} A_{t'} \rho^{2t'}\right). \tag{D.9}$$

Using $u_0 = \sqrt{1-s_0^2}$ and $d_0 = (u_0/s_0)^2$ as auxiliary quantities, the detailed scheme now looks as follows,

$$\begin{cases} a_0 = \frac{1}{2} - \frac{1}{6}d_0, \qquad b_0 = \frac{1}{2}d_0 + \ln\left(\frac{u_0}{d_0}\right), \\ \qquad\qquad\qquad\qquad\qquad\qquad c_0 = -\left\{1 + \frac{1-s_0^2}{s_0^2}\ln(1-s_0^2)\right\}, \\ a_1 = \frac{1}{2}\left(1 - \frac{1}{5}d_0^2\right),\ b_1 = -\frac{1}{4}d_0\,(2-d_0)\,, \\ \qquad\qquad\qquad\qquad\qquad\qquad c_1 = -3\sum_{m=1}^{\infty}\frac{s_0^{2m}}{(m+1)(m+2)}, \end{cases} \tag{D.10}$$

$$\begin{cases} g' = -\frac{1}{4}(c_0 - c_1) + (-p+1)(b_0 - b_1) + if(a_0 - a_1), \\ f' = \frac{1}{2}ic_1 + 2fa_1 - 2i(-p+1)b_1, \end{cases} \tag{D.11}$$

$$\begin{cases} A_0 = (-p+1)\ln 2 - g', \qquad A_1 = \frac{1}{4}s_0^2\left(p + \frac{2if}{u_0}\right) - if', \\ A_{t'} = \left\{(p-1)\binom{-\frac{1}{2}}{t'}(-1)^{t'} + \frac{1}{2} - \frac{if}{u_0}\binom{-\frac{1}{2}}{t'-1}(-1)^{t'}\right\}\frac{s_0^{2t'}}{2t'}, \quad t' = 2,3,..., \end{cases} \tag{D.12}$$

with the binomial coefficients again given by Eq.(2.51). The values of the B-coefficients in Eq.(D.9) are then given by

$$\begin{aligned} B_0 &= \exp(A_0)\,, \\ B_{t+1} &= \sum_{j=0}^{t}\frac{t+1-j}{t+1}\,A_{t+1-j}\,B_j\,, \qquad t = 0,1,...\ . \end{aligned} \tag{D.13}$$

The number of coefficients to be used can be judged from the convergence of the series expansion for $I(r,f)$. Like in the first case, even for numerical aperture values s_0 as high as 0.95, a limited number of coefficients is generally needed to attain an accuracy of, say 10^{-4}, in complex amplitude, or, equivalently, 10^{-8} in intensity. Such an accuracy is largely sufficient in practical applications where the measured intensity data, to be used in a retrieval process, are affected by noise at a much higher level.

E The predictor-corrector procedure

The predictor-corrector procedure has been described and tested in simulations in [van der Avoort, Braat, Dirksen, Janssen (2005)], Sec. 4, for the case of relatively low-numerical-aperture systems that allow a scalar treatment of the

image formation. The extension to the high-numerical-aperture vectorial case is rather straightforward. The basic principles being identical, we only present a brief outline.

The starting point of the predictor-corrector method is the availability of a measured through-focus intensity distribution I. From this distribution, by Fourier analysis, we form the various parts with azimuthal dependence $\exp(im\phi)$ that are represented in the form

$$I_m = \left(\beta_0^0\right)^2 \chi_{0,0}^{0,0} + 2{\sum_{n,m}}' \beta_0^0 \beta_n^{m*} \chi_{n,0}^{m,0} + {\sum_{n,m}}' {\sum_{n',m'}}' \beta_n^m \beta_{n'}^{m'*} \chi_{n,n'}^{m,m'} \quad . \tag{E.1}$$

Here we use the symbols $\chi_{0,0}^{0,0}$ and $\chi_{n,0}^{m,0}$ to identify the dominant aberration-free self-interference term and the dominant cross-terms, respectively, that arise in accordance with Eq.(3.12) and Eq.(5.24). The third term on the right-hand side of Eq.(E.1), $\chi_{n,n'}^{m,m'}$, is an elaborate term that involves products $V_{n;j}^m V_{n';j'}^{m'*}$, pertaining to relatively small cross-terms. The $'$-signs in the summations in (E.1) indicate that the terms with $n = m = 0$ and $n' = m' = 0$ should be deleted. In the basic linearized retrieval scheme, we choose the β's in the small cross-term deleted version

$$\left(\beta_0^0\right)^2 \chi_{0,0}^{0,0} + 2{\sum_{n,m}}' \beta_0^0 \beta_n^{m*} \chi_{n,0}^{m,0} \tag{E.2}$$

of (E.1) such that the match between (E.2) and I_m is maximal; this is done in accordance with Eqs.(5.26)-(5.27). The resulting β's are denoted by $\beta_n^m(1)$ and form a first estimate of the β's in (E.1) that serve to represent I_m.

In the linearized retrieval scheme matching was done with the small cross-terms deleted. Now that an estimate $\beta_n^m(1)$ has been found, the small cross-term expression in Eq.(E.1) can be estimated as

$${\sum_{n,m}}' {\sum_{n',m'}}' \beta_n^m(1) \beta_{n'}^{m'*}(1) \chi_{n,n'}^{m,m'} \tag{E.3}$$

in which the unknown β_n^m are replaced by their first estimates $\beta_n^m(1)$. A direct computation of (E.3) is, however, quite involved since the $\chi_{n,n'}^{m,m'}$ are rather complicated, so we proceed in a different manner. We compute, using the forward scheme for computing the field components E_i in Eq.(2.65), the through-focus intensity point-spread function $I(1) = |\mathbf{E}(1)|^2$ of the optical system with pupil function $P(1)$ of Eq.(5.22) where we have set $\beta_n^m = \beta_n^m(1)$ throughout. Then,

in accordance with (E.1), the quantity of (E.3) is given by

$$I(1)-\left(\beta_0^0(1)\right)^2\chi_{0,0}^{0,0}-2{\sum_{n,m}}'\beta_0^0(1)\beta_n^{m*}(1)\chi_{n,0}^{m,0}\ , \tag{E.4}$$

and its computation is now much easier and feasible in a strongly reduced time.

Having available now the double summation cross-term of (E.3), we perform basic retrieval with the I_m replaced by

$$I_m-{\sum_{n,m}}'{\sum_{n',m'}}'\beta_n^m(1)\beta_{n'}^{m'*}(1)\chi_{n,n'}^{m,m'}\ . \tag{E.5}$$

Hence, the β's in Eq.(E.2) now maximize the match between Eqs.(E.2) and (E.5) to yield a new collection of coefficients $\beta_n^m(2)$. This whole process of adjusting I_m is repeated until convergence is reached. When convergence is reached we have obtained coefficients $\beta_n^m(\infty)$ that satisfy

$$I_m-{\sum_{n,m}}'{\sum_{n',m'}}'\beta_n^m(\infty)\beta_{n'}^{m'*}(\infty)\chi_{n,n'}^{m,m'}= \left(\beta_0^0(\infty)\right)^2\chi_{0,0}^{0,0}-2{\sum_{n,m}}'\beta_0^0(\infty)\beta_n^{m*}(\infty)\chi_{n,0}^{m,0}\ . \tag{E.6}$$

By bringing the double summation at the left-hand side of Eq.(E.6) to the right side of (E.6), we see that we have managed to represent I_m in the form Eq.(E.1) using $\beta_n^m=\beta_n^m(\infty)$.

F Zernike coefficients for circularly symmetric polarization states

The incident field in the entrance pupil is given by Eq.(3.21) and using the expansion of Eq.(2.64) with

$$\begin{aligned}E_x&=\sum\beta_{n,x}^m R_n^{|m|}(\rho)\exp(im\theta),\\ E_y&=\sum\beta_{n,y}^m R_n^{|m|}(\rho)\exp(im\theta),\end{aligned} \tag{F.1}$$

we form the inner products with a general Zernike polynomial $R_n^{|m'|}(\rho)\exp(im'\theta)$. For the E_x-component we obtain

$$\frac{1}{\pi}\iint_{\mathcal{A}}\cos(\theta+\theta_0)R_n^{|m'|}(\rho)\exp(-im'\theta)\rho d\rho d\theta$$

$$= \frac{1}{\pi} \sum_{n,m} \int_0^{2\pi} \int_0^1 \beta_{n,x}^m R_n^{|m|}(\rho) \exp(+im\theta) R_n^{|m'|}(\rho) \exp(-im'\theta) \rho d\rho d\theta$$

$$= 2\beta_{n,x}^{m'} \int_0^1 \left[R_n^{|m'|}(\rho)\right]^2 \rho d\rho = \frac{\beta_{n,x}^{m'}}{n+1}, \tag{F.2}$$

where we have used the properties of the inner products of the radial Zernike polynomials $R_n^{|m|}$, see [Born, Wolf (2002)]. Evaluating the first integral in (F.2) then yields

$$\beta_{n,x}^{m'} = \frac{n+1}{\pi} \int_0^1 \int_0^{2\pi} \left[\frac{\exp\{i(\theta+\theta_0)\} + \exp\{-i(\theta+\theta_0)\}}{2}\right] \times \exp(-im'\theta) d\theta \int_0^1 R_n^{|m'|}(\rho) \rho d\rho$$

$$= (n+1) \left\{\exp(i\theta_0)\delta_{m',+1} + \exp(-i\theta_0)\delta_{m',-1}\right\} \int_0^1 R_n^{|m'|}(\rho) \rho d\rho, \tag{F.3}$$

with $\delta_{m,m'}$ the Kronecker symbol.

Using the properties of the Jacobi polynomials, see [Braat, Dirksen, Janssen, van de Nes (2003)], an analytic solution of the integral over ρ can be found

$$\int_0^1 R_{m+2p}^m(\rho) \rho d\rho = \frac{1}{2}(-1)^p \frac{(\frac{m}{2})_p}{(\frac{m+2}{2})_{p+1}}$$

with the Pochhammer symbol $(m)_p$ given by

$$\begin{cases} (m)_p = m(m+1)....(m+p-1) \ , \\ (m)_0 = 1 \ . \end{cases} \tag{F.4}$$

For our special case $|m'| = 1$; we then find the only nonzero coefficients $\beta_{2n+1,x}^{\pm 1}$ and $\beta_{2n+1,y}^{\pm 1}$ of Eq.(3.22).

References

[Conrady (1929)] Conrady, A.E., Applied Optics and Optical Design, Volume I, Oxford 1929.

[Wolf (1951)] Wolf, E., 1951, Rep. Prog. Phys., 14, 95-120.

[Korteweg, Huygens complete works (1941)] Huygens C., 1941, Complete works, Ed. D. Korteweg, Royal Dutch Academy of Arts and Sciences, Amsterdam.

[Airy (1835)] Airy, G.B., 1835, Trans. Camb. Phil. Soc., 5, 283.

[Rayleigh (1879)] Rayleigh, 1879, Phil. Mag., 8, 403.

[Lommel (1885)] Lommel, E., 1885, Abh. Bayer. Akad., 15, Abth. 2, 233; 1886, Abh. Bayer. Akad., 15, Abth. 3, 531.

[Strehl (1896)] Strehl, K., 1894, Theorie des Fernrohrs, Barth, Leipzig.

[Conrady (1919)] Conrady, A., 1919, Mon. Not. R. Astr. Soc., 79, 575.

[Steward (1925)] Steward, G.C., 1925, Phil. Trans. Roy. Soc. A, 225, 131; and: 1926, Trans. Camb. Phil. Soc., 23, 235.

[Picht (1925)] Picht, J., 1925, Ann. Phys., Lpz., 77, 685; and: 1926, Ann. Phys., Lpz., 80, 491.

[Richter (1925)] Richter, R., 1925, Z. Instrumentkunde, 45, 1.

[Zernike (1934)] Zernike, F., 1934, Physica, 1, 689.

[Nijboer (1942)] Nijboer, B.R.A., 1942, Thesis, University of Groningen, Groningen. An electronic version can be downloaded from http://www.nijboerzernike.nl

[Zernike, Nijboer (1949)] Zernike, F. and Nijboer, B.R.A., 1949, Contribution in La Théorie des Images Optiques (Paris : Éditions de la Revue d'Optique).

[Maréchal (1947)] Maréchal, A., 1947, Rev. Opt. (théor. instrum.), 26, 257 and 1947, J. Opt. Soc. Am. 37, 982.

[Born, Wolf (2002)] Born, M. and Wolf, E., 2002, Principles of Optics, 7th edition, Cambridge University Press, Cambridge, UK.

[Ignatowsky (1919)] Ignatowsky, V.S., 1919, Tr. Opt. Inst. 1 (4), 1.

[Hopkins (1943)] Hopkins, H.H., 1943, Proc. Phys. Soc., 55, 116.

[Wolf (1959)] Wolf, E., 1959, Proc. R. Soc. London Ser. A 253, 352.

[Richards, Wolf (1959)] Richards, B. and Wolf, E., 1959, Proc. R. Soc. London Ser. A 253, 358.

[Gerchberg, Saxton (1971)] Gerchberg, R.W. and Saxton, W.O., 1971, Optik 34, 275.

[Gerchberg, Saxton (1972)] Gerchberg, R.W. and Saxton, W.O., 1972, Optik 35, 237.

[Frieden (1972)] Frieden, B.R., 1972, J. Opt. Soc. Am. 62, 511.

[VanDijck, Coene (1987)] VanDijck, D. and Coene, W., 1987, Optik 77, 125.

[Fienup (1982)] Fienup, J.R., 1982, Appl. Opt. 21, 2758.

[Gonsalves (1982)] Gonsalves, R.A., 1982, Opt. Eng. 21, 829.

[Barakat, Sandler (1992)] Barakat, R. and Sandler, B.H., 1992, J. Opt. Soc. Am. A 9, 1715.

[Frieden, Oh (1992)] Frieden, B.R. and Oh, C., 1992, Appl. Opt. 31, 1103.

[Fienup, Marron, Schultz, Seldin (1993)] Fienup, J.R., Marron, J.C., Schultz, T.J., and Seldin, J.H., 1993, Appl. Opt. 32, 1747.

[Iglesias (1998)] Iglesias, I., 1998, Appl. Opt. 37, 5427.

[Fienup (1999)] Fienup, J.R., 1999, J. Opt. Soc. Am. A 16, 1831.

[Weyl (1919)] Weyl, H., 1919, Ann. Phys. (Leipzig) 60(22), 481.

[Stamnes (1986)] Stamnes, J.J., 1986, Waves in Focal Regions, Adam Hilger, Bristol.

[Sherman (1967)] Sherman, G.C., 1967, J. Opt. Soc. Am. 57, 546.

[Debye (1909)] Debye, P., 1909, Ann. Phys. Lpz. 30, 755.

[Wolf, Li (1981)] Wolf, E., and Li, Y., 1981, Opt. Commun. 39, 205.

[Welford (1986)] Welford, W.T., 1986, Aberrations of optical systems, Adam Hilger, Bristol.

[Sheppard, Török (1997)] Sheppard, C.J.R. and Török, P., 1997, J. Mod. Optics 44, 803.

[Stallinga (2004-1)] Stallinga, S., 2004, J. Opt. Soc. Am. A 21, 1785.

[Siegman (1986)] Siegman, A.E., 1986, Lasers, University Science Books, Mill Valley, CA, USA.

[Barnett, Allen (1994)] Barnett, S.M. and Allen, L., 1994, Opt. Commun. 110, 670.

[Beijersbergen, Coerwinkel, Kristensen, Woerdman (1994)] Beijersbergen, M.W., Coerwinkel, R.P.C., Kristensen, M., and Woerdman, J.P., 1994, Opt. Commun. 112, 321.

[Kintner, Sillitto (1976)] Kintner, E.C. and Sillitto, R.M., 1976, Opt. Act. 23, 607.

[Janssen (2002)] Janssen, A.J.E.M., 2002, J. Opt. Soc. Am. A 19, 849.

[Braat, Dirksen, Janssen (2002)] Braat, J.J.M., Dirksen, P., and Janssen, A.J.E.M., 2002, J. Opt. Soc. Am. A 19, 858.

[Cao (2003)] Cao, Q., 2003, J. Opt. Soc. Am. A 20, 661.

[Janssen, Braat, Dirksen (2004)] Janssen, A.J.E.M., Braat, J.J.M., and Dirksen, P., 2004, J. Mod. Optics 51, 687.

[Abramowitz (1970)] Abramowitz, M. and Stegun, I. A., 1970, Handbook of Mathematical Functions, Dover, New York.

[Boivin, Dow, Wolf, 1967] Boivin, A., Dow, J., and Wolf, E., 1967, J. Opt. Soc. Am. 57, 1171.

[Stallinga (2001)] Stallinga, S., 2001, J. Opt. Soc. Am. A 18, 2846.

[Quabis, Dorn, Eberler, Glöckl, Leuchs (2000)] Quabis, S., Dorn, R., Eberler, M., Glöckl, O., and Leuchs, G., 2000, Opt. Commun. 179, 1.

[Ettl, Creath (1996)] Ettl, P. and Creath, K., 1996, Appl. Opt. 35, 5108.

[Braat, Dirksen, Janssen, van de Nes (2003)] Braat, J.J.M., Dirksen, P., Janssen, A.J.E.M., and van de Nes, A.S., 2003, J. Opt. Soc. Am. A 20, 2281.

[Ling, Lee (1984)] Ling, H. and Lee, S., 1984, J. Opt. Soc. Am. A 1, 965.

[Török, Varga, Laczik, Booker (1995)] Török, P., Varga, P., Laczik, Z., and Booker, G.R., 1995, J. Opt. Soc. Am. A 12, 325.

[Török, Sheppard, Varga (1996)] Török, P., Sheppard, C.J.R., and Varga, P., 1996, J. Mod. Optics 43, 1167.

[Mansuripur (1986)] Mansuripur, M., 1986, J. Opt. Soc. Am. A 3, 2086.

[Mansuripur (1989)] Mansuripur, M., 1989, J. Opt. Soc. Am. A 6, 786.

[Flagello, Milster (1992)] Flagello, D.G. and Milster, T., 1992, Proceedings of SPIE 1625, 246.

[Flagello, Milster, Rosenbluth (1996)] Flagello, D.G., Milster, T., and Rosenbluth, A.E., 1996, J. Opt. Soc. Am. A 13, 53.

[Macleod (1989)] Macleod, H.A., 1989, Thin film optical filters, McGraw- Hill, New York, USA.

[van de Nes, Billy, Pereira, Braat (2004)] van de Nes, A.S., Billy, L., Pereira, S.F., and Braat, J.J.M., 2004, Opt. Express 12, 1281.

[Visser, Wiersma (1991)] Visser, T.D. and Wiersma, S.H., 1991, J. Opt. Soc. Am. A 8, 1404.

[He, Friese, Heckenberg, Rubinsztein-Dunlop (1995)] He, H., Friese, M.E.J., Heckenberg, N.R., and Rubinsztein-Dunlop, H., 1995, Phys. Rev. Lett. 75, 826.

[Allen, Beijersbergen, Spreeuw, Woerdman (1992)] Allen, L., Beijersbergen, M.W., Spreeuw, R.J.C., and Woerdman, J.P., 1992, Phys. Rev. A 45, 8185.

[Gonsalves (1982)] Gonsalves, R., 1982, Opt. Eng. 21, 829.

[Gonsalves (2001)] Gonsalves, R., 2001, Opt. Lett. 26, 684.

[Kogelnik (1965)] Kogelnik, H., 1965, Appl. Opt. 4, 1562.

[Teague (1983)] Teague, M.R., 1983, J. Opt. Soc. Am. 73, 1434.

[Woods, Greenaway (2003)] Woods, S.C. and Greenaway, A.H., 2003, J. Opt. Soc. Am. A 20, 508.

[Wesner, Heil, Sure (2002)] Wesner, J., Heil, J., and Sure, T., 2002, Proceedings of SPIE 4767, 32.

[Dirksen, Braat, Janssen, Leeuwestein (2005)] Dirksen, P., Braat, J.J.M., Janssen, A.J.E.M., and Leeuwestein, A., 2005, Proceedings of SPIE 5754, 262.

[van der Avoort, Braat, Dirksen, Janssen (2005)] van der Avoort, C., Braat, J.J.M., Dirksen, P., and Janssen, A.J.E.M., 2005, J. Mod. Optics 52, 1695.

[Dirksen, Braat, Janssen, Juffermans (2003)] Dirksen, P., Braat, J., Janssen, A. J. E. M., and Juffermans, C., 2003, J. Microlithogr., Microfabr., Microsyst. 2, 61.

[Mahajan (1998)] Mahajan, V.N., 1998, Optical Imaging and Aberrations. Part I: Ray Geometrical Optics, SPIE, Bellingham, Wash.

[Dirksen, Braat, Janssen, Juffermans, Leeuwestein (2003)] Dirksen, P., Braat, J., Janssen, A. J. E. M., Juffermans, C., and Leeuwestein, A., 2003, Proceedings of SPIE 5040, 0277-786X.

[Dirksen, Braat, Janssen (2006)] Dirksen, P., Braat, J., and Janssen, A. J. E. M., 2006, J. Microlithogr., Microfabr., Microsyst. 5, 013005-1.

[Lavery, Vogt, Prabhu, Lin, Wu (2006)] Lavery, K.A., Vogt, B.D., Prabhu, V.M., Lin, E.K., and Wu, W.-L., 2006, J. Vac. Sci. Techn. B24, 3044.

[Braat, Dirksen, Janssen, van de Nes, van Haver (2005)] Braat, J.J.M., Dirksen, P., Janssen, A.J.E.M., van de Nes, A.S., and van Haver, S., 2005, J. Opt. Soc. Am. A 22, 2635.

[van Haver, Braat, Dirksen, Janssen (2006)] van Haver, S., Braat, J.J.M., Dirksen, P., and Janssen, A.J.E.M., 2006, J. Eur. Opt. Soc. -RP 1, 06004, 1.

[SOLID-C (2004)] SOLID-C, 2004, a software product (release 6.3.0) of SIGMA-C GmbH, Thomas-Dehlerstrasze 9, D-81737 Munich, Germany.

[Jones (1941)] Jones, R.C., 1941, J. Opt. Soc. Am. 31, 488.

[McGuire, Chipman (1990)] McGuire, J.P. and Chipman, R.A., 1990, J. Opt. Soc. Am. A 7, 1614.

[Lu, Chipman (1994)] Lu, S.-Y. and Chipman, R.A., 1994, J. Opt. Soc. Am. A 11, 766.

[VanWiggeren, Roy (1999)] Van Wiggeren, G.D. and Roy, R., 1999, Appl. Opt. 38, 3888.

[Stallinga (2004-2)] Stallinga, S., 2004, J. Opt. Soc. Am. A 21, 2406.